Investigation of Novel Positron Emission Tomography Radioligands for In Vivo Characterization of Alzheimer's Disease Pathophysiology

By

Tobey J. Betthauser

A dissertation submitted in partial fulfillment of
the requirements for the degree of

Doctor of Philosophy
(Medical Physics)

at the
UNIVERSITY OF WISCONSIN-MADISON
2018

Date of final oral examination: 4/10/2018

The dissertation is approved by the following members of the Final Oral Committee:
Bradley T. Christian, Professor, Medical Physics
Marina E. Emborg, Associate Professor, Medical Physics
Jonathan W. Engle, Assistant Professor, Medical Physics
Barbara Bendlin, Associate Professor, Geriatrics
Sterling C. Johnson, Professor, Medicine-Geriatrics

This work is dedicated to Agnes Webster, Joan Strum, Gene Webster, and Lyle Gordon.

ACKNOWLEDGEMENTS

Beginning in 2010, I took the first steps toward a dramatic change in my career and my life hoping that one day I would find myself doing something I both enjoyed and that would make a positive impact. I could never have imagined that I would end up conducting medical research at the University of Wisconsin-Madison. I have been fortunate to always have a combination of family, friends, mentors and colleagues to support and guide me throughout this transformative process.

My PhD advisor Dr. Brad Christian has been truly remarkable. Your willingness to integrate students into all aspects of PET studies and the freedom you have granted me to explore everything from particle accelerator physics to tracer kinetic analysis and beyond have positioned me with an excellent background in neuroimaging that I will leverage in future endeavors. I cannot express how much I appreciate the support and guidance in academic, professional and other matters that you have given me.

Thank you to Dr. Sterling Johnson for your support of my early career development and the investment you and the ADRC have placed in me. Thank you to Drs. Jean Ann Hunt, Ken Podolak, and Michael Walters for encouraging me to challenge myself and for helping me realize opportunities that I did not know I had. I would also like to thank the late Larry Sturm for mentoring me on how to be a professional and to always do the right thing the first time.

I am extraordinarily grateful for my wife Laura and our wonderful children. Laura, I cannot emphasize enough how appreciative I am for everything you do and the many sacrifices you and our family have made that have allowed me to pursue my PhD. Oliver, Amelia, and Vanessa, the three of you inspire me every day to persist, be a better person and are my greatest escape when I need it most. I am also fortunate to have immense support from my parents Roxie and Paul, my siblings Tasha and Torin and their families, the Satre and Brendel families, and my extended family. All of you have contributed to my success in many ways throughout my life and academic career.

During my graduate studies I have been privileged to work and study alongside many brilliant minds in the Christian Lab, the Waisman Brain Imaging and Behavior Group, the UW Cyclotron Group and the UW Department of Medical Physics. Notably, Patrick Lao has been an amazing friend and colleague. We spent many late nights, weekends and long days (← no Oxford comma) together in the lab and traveling to present our work. It was great to know there was someone going through the process alongside me that understood the ups and downs and could filter my sometimes nonsensical ideas with absolutely without fear. Paul Ellison, Ansel Hillmer and Dustin Wooten have been and continue to be excellent friends and guides during my early career. Karly Cody, Matthew Zammit, and Alex DiFilippo, probably without really knowing, have greatly contributed to my understanding of the details of PET radiochemistry, imaging and analysis by forcing me to get you the right answers. Barb Mueller and all of the study coordinators that have contributed their time and efforts into making human studies possible always provided a welcomed outlet and a comforting atmosphere in the lab. Lastly, despite the stresses involved in graduate studies, my fellow students and friends in the Department of Medical Physics, especially the 2013 cohort, have made my graduate school experience positively enjoyable.

TABLE OF CONTENTS

Copyright Disclosures
Section 2.2 was adapted with permission from Elsevier from
Section 3.3 was adapted with permission from *The Journal of Nuclear Medicine* from
Section 3.4 was adapter with permission from *The Journal of Nuclear Medicine*
Chapter 4 was adapted with permission from Elsevier from

LIST OF TABLES

LIST OF FIGURES

ABSTRACT

Positron emission tomography (PET) has become an integral component of neurodegenerative disease research. The rapid implementation of novel PET radiopharmaceuticals into clinical research necessitates detailed characterization and optimization of the radiopharmaceutical production process, PET imaging protocol, and image processing and analysis methodology. This work details the optimization and automated production of PET radioligands [^{18}F]THK-5351 and [^{18}F]MK-6240, investigates methodological considerations for image processing and quantification of [^{18}F]THK-5317, [^{18}F]THK-5351, and [^{18}F]MK-6240, and evaluates the application of these PET radiopharmaceuticals for human imaging neurofibrillary tangles (NFTs, a hallmark proteinopathy of Alzheimer's disease) in the context of clinical neurodegenerative disease research. In addition, dosimetric considerations and longitudinal, multi-tracer image processing and analysis pipelines are explored.

Individual steps of the radiochemical synthesis, purification and formulation processes were examined and translated to automated production routines, which produce radiopharmaceuticals characterized and suitable for human research use. As part of this process, a novel purification and formulation device was designed, manufactured, and tested.

PET radioligands [^{18}F]THK-5317, [^{18}F]THK-5351 and [^{18}F]MK-6240 were investigated in human subjects ranging from cognitively stable controls to persons clinically diagnosed with probable AD dementia. Pharmacokinetic properties, radiotracer binding, and quantification methods and imaging protocols were explored individually for each radiotracer. Comparisons were made between radiotracers using optimized PET acquisition, processing and analysis methods.

The remaining chapters investigate practical considerations for longitudinal PET studies including internal dosimetry, semi-automated processing and analysis of multimodal, multi-tracer PET and MRI neuroimaging data, and the effects of attenuation correction on longitudinal PET binding estimates.

The results of this work provide a framework that facilitates large-scale, multi-tracer, multi-modal imaging investigation of the pathophysiological processes occurring in the Alzheimer's disease continuum within a longitudinal paradigm.

CHAPTER 1

INTRODUCTION

Medical imaging provides a link between macroscopic topographical images and biological processes occurring at the molecular level. Multimodal magnetic resonance imaging (MRI) and multi-tracer positron emission tomography (PET) studies are becoming increasingly important for characterizing molecular pathophysiological changes associated with neurodegenerative diseases during life. The demand for *in vivo* imaging of neurofibrillary tangle (NFT) and beta-amyloid (Aβ) plaque pathologies in Alzheimer's disease (AD) has led to development of novel PET radiopharmaceuticals and rapid integration of these compounds into clinical research. PET radiotracers require extensive characterization and methodological development so meaningful interpretation of PET images can be extended to biological features of disease. The research described in this work examines methodological considerations for radiopharmaceutical production, characterization, quantification and safe administration of PET radiopharmaceuticals, and image processing and analysis for clinical neurodegenerative disease research in human subjects.

1.1 Overview of Alzheimer's Disease

Alzheimer's disease is a neurodegenerative disease that is the sixth leading cause of death in the United States and is the leading cause of dementia(1). In addition to the stress placed on individuals, families and caregivers, the cost of care associated with AD is estimated to be $287,000 during the last five years of life, with costs and the prevalence of AD expected to increase with an increasingly elderly population(2). On top of rising costs, the prognosis for persons with AD is bleak since no effective disease modifying therapies currently exist that slow or halt the disease process(3). The lack of available therapies is due to a combination of several factors including: 1) a poor understanding of pathogenic mechanisms and pathophysiological interactions, 2) the disease process in AD has a long prodromal period prior to changes in cognition making current clinical endpoints for trials several years to more than a decade downstream of treatment, 3) selection criteria for clinical trials has not been informed by evidence of AD pathophysiology, and 4) clinical intervention trials have largely focused on treating late-stage disease after neuronal damage has likely already occurred(4).

Concurrently, definitive diagnosis of Alzheimer's disease requires postmortem pathological examination to confirm the presence of pathological hallmarks of AD (neurofibrillary tangles (NFTs) and beta-amyloid (Aβ) plaques)(5-7). Current clinical criteria for antemortem AD diagnosis (possible AD or probable AD) are limited to reviewing patient history and longitudinal cognitive assessment(8) that do not provide high levels of diagnostic accuracy (44.3% to 70.8%) when evaluated against the gold standard of neuropathological confirmation(9).

These historical shortcomings have led to considerable efforts to develop *in vivo* AD biomarkers that can be used to detect and monitor pathophysiological processes during life. Ongoing research suggests that AD biomarkers will play a critical role in advancing the understanding of the processes occurring during the disease progression, thereby improving antemortem diagnostic criteria and aiding in the development of disease modifying therapies. The importance of AD biomarkers for clinical and research applications is reflected in recommendations made by both the National Institute on Aging-Alzheimer's Association (NIA-AA) and the International Working Group (IWG) for New Research Criteria for the Diagnosis of Alzheimer's Disease to incorporate biomarkers as a way to improve diagnostic accuracy of various patient groups(5, 6, 8, 10-14).

1.2 Neuropathological Staging of Alzheimer's Disease Proteinopathies

AD is characterized by the aggregation of neurofibrillary tangles (NFTs) composed of tau protein (15), and neuritic plaques composed of beta-amyloid (Aβ) protein(16), along with neurodegeneration and progressive cognitive impairment(17, 18). These pathological features were first described by Alois Alzheimer using silver staining techniques in 1907(19). Neuropathology studies involving thousands of cases have indicated that disease related changes in Aβ and tau are occurring decades prior to the onset of cognitive deficits(17) and follow spatially hierarchical patterns(15, 16, 20-22). Topographical patterns of Aβ deposition were characterized by Thal and colleagues(16), and Braak and Braak for NFTs(15), which are summarized in Table 1.1.

Aβ plaques are composed of fibrils of Aβ peptides that have undergone posttranslational modification resulting in insolubility and aggregation in the extracellular environment(23). In AD, the pattern of beta-amyloidosis is broken into five distinct phases where Aβ deposits are first observed in the neocortex and then spread medially to subcortical structures and ultimately into the cerebellum(16). Similar to Aβ, the

Pathological Feature	Stage/Phase	Affected Regions
Aβ Plaques	Phase 1	Frontal, Temporal, Parietal, Occipital Neocortex
	Phase 2	Phase 1 Regions and Amygdala, Cingulate, Presubiculum
	Phase 3	Phase 1 and 2 Regions and Subcortical Regions (Striatum, Basal Forebrain, Thalamus, hypothalamus)
	Phase 4	Phase 1-3 Regions and Brainstem Nuclei (Olivary Nucleus, Medulla, Midbrain)
	Phase 5	Phase 1-4 Regions and Cerebellum and Other Brainstem Nuclei
Tau Pretangles	Pretangle a-c	Subcortical Regions (Locus Coeruleus, Midbrain Tegmentum, Raphe Nuclei, Magnocellular Nuclei)
	Pretangle 1a-1b	Pretangle a-c Regions and Medial Temporal Cortex Including Transentorhinal Cortex
NFTs	Stage I	Transentorhinal Cortex
	Stage II	Stage I Regions and Entorhinal Cortex and Hippocampus
	Stage III	Stage I-II Regions and Fusiform and Lingual Gyri
	Stage IV	Stage I-III Regions and Neocortical Association Areas (Superior Temporal Gyrus)
	Stage V	Stage I-IV Regions and Frontal , Parietal, and Peristriate Occipital Neocortex
	Stage VI	Stage I-V Regions and Parastriate and Striate Occipital Neocortex

Table 1.1 Neuropathological Staging of Alzheimer's Disease

tubulin associated unit (tau) undergoes posttranslational modifications to ultimately form NFTs(24-26). NFTs in AD are composed of paired-helical filaments (PHF) of hyperphosphorylated tau protein(27). Unlike Aβ, NFTs are found in the intracellular space of neurons, until after cell death when they can occupy the extracellular space as “ghost tangles”(26, 27). Topographically, tau deposition begins as soluble hyperphosphorylated tau pretangles in brainstem nuclei, followed by insoluble NFT deposition in the transentorhinal cortex and spreads inferiolaterally to adjacent temporal cortex and ultimately into the greater neocortex(15, 20, 22). Although neuropathological examination has laid the groundwork characterizing these proteinopathies, it is limited to predefined slices and cross-sectional analysis, which precludes longitudinal characterization of the entire 3D brain volume during the disease process.

1.3 The Amyloid Cascade Hypothesis

Despite thorough neuropathological characterization, etiological mechanisms for AD are still poorly understood. Several hypotheses have been proposed to explain the pathogenic mechanisms that account for AD pathophysiology(28-32). The most widely accepted theory, the amyloid cascade hypothesis, suggests that Aβ deposition is the causative first step in the disease cascade that leads to subsequent NFT aggregation, neuronal cell loss, vascular damage, and ultimately dementia(29, 33). Since its inception, a growing body of human AD research continues to support this hypothesis. Genetic mutations affecting the amyloid precursor protein (APP) including *presenilin 1* and *2* (*PS1* and *PS2*) and the *APP* gene, as well as the presence of the *APOE-ε4* allele, which alters the clearance of Aβ, result in increased risk and earlier age of onset for persons developing AD dementia(34). Similarly, individuals with Down syndrome (DS, trisomy 21, which contains the *APP* gene) develop AD at an earlier age and at a higher prevalence compared to the non-DS population(35, 36). Contrary to the amyloid cascade hypothesis, therapeutic trials targeting Aβ have proven ineffective, although these clinical trials likely suffer from a combination of inadequate screening criteria that does not require evidence of AD pathophysiology, treatment administration in cognitively affected persons in which neurodegeneration has likely already occurred, and inadequate primary clinical endpoints that are not reflective of altered pathophysiology, but rather differences in cognitive performance (37, 38). Additionally confounding hypothesis testing are cofactors of normal aging and the frequent occurrence of comorbidities such as vascular disease, diabetes, and heart disease(28, 39), as well as comorbid neurodegenerative diseases(40). These complicated interactions can potentially be understood by utilizing *in vivo* biomarkers to detect pathophysiological features of disease.

1.4 Biomarker Staging of AD Pathophysiology

As AD biomarkers became available, researchers sought to characterize patterns of biomarker change related to disease progression. Jack and colleagues popularized a model that relates biomarkers for Aβ (cerebrospinal fluid (CSF) assays and PET imaging), tau (CSF), and neurodegeneration (structural MRI and fluorodeoxyglucose (FDG) PET) to later stage cognitive decline in AD(41). The model is based on biomarker evidence of pathophysiological changes, which are proposed to be individually sigmoidal with progressive disease and having early fast, middle steady, and late slowing rates of accumulation or severity(42). The biomarker cascade follows similarly to the amyloid cascade hypothesis wherein changes in detectable Aβ precede overlapping changes in tau followed by increasing neurodegeneration, and lastly progressive cognitive decline that is modulated by AD risk factors(42). While this is a suitable approach for CSF biomarkers that give a single measured value of Aβ and tau concentrations, a criticism of the model is that it condenses multidimensional tomographic imaging data into a single measure, eliminating the potentially useful topographical information that neuropathology findings suggest are important for disease staging. Indeed, recent studies applying hierarchical statistical models to Aβ and NFT PET imaging suggest that PET biomarkers follow ordered spatial patterns in cross-sectional data(43, 44), which may be useful for differential diagnosis(45) of AD and non-AD dementias and *in vivo* AD staging.

1.5 Development of PET Radiopharmaceuticals for Imaging AD Pathophysiology

PET radiopharmaceuticals developed for neuroimaging applications require specific physicochemical properties that result in suitable imaging characteristics (46-49). Generally, radioligands that enter the brain by passive diffusion need to be small (<700 Da), moderately lipophilic (LogP 1-3 at pH 7.4), and have a high affinity for their respective targets (K_D~1nM, see Chapter 3 for a more detailed explanation of affinity the equilibrium dissociation constant K_D)(50). In addition, these ligands must be amenable to radiolabeling and exhibit *in vivo* pharmacokinetic properties that are matched with short-lived PET radioisotopes with half-lives in the range of minutes to hours. Specific to imaging amyloids, many neurodegenerative diseases are characterized by specific amyloid aggregates (e.g. Aβ, alpha-synuclein, tau, Huntington, etc.) that are present in different *in vivo* concentrations, which requires PET radioligands targeting Aβ plaques and NFTs to be highly selective to these targets(50). This is especially the case in AD where these aggregates co-localize, and Aβ deposits are 4- to 20-fold more concentrated than NFTs(51).

A major hurdle thwarting the development of therapeutic and diagnostic agents is the lack of understanding of the chemical structure of amyloids, which would provide insights into potential binding sites for exogenous drugs(50). X-ray crystallography, electron microscopy (EM) and nuclear magnetic resonance spectroscopy have provided much of the macromolecular structural information that currently defines amyloid aggregates(52), but these techniques do not provide sufficient resolution to determine precise chemical structures of amyloid fibrils that compose these aggregates(50). Recently, a major step towards defining the chemical structures of Aβ(1-40) and Aβ(1-42) fibrils, and paired-helical and straight filaments (SF) of tau from filtered human AD tissue samples has been realized using cryo-electron microscopy(53, 54). These findings, combined with previous macromolecular structural knowledge(55, 56) suggest that 1) non-specific panamyloid agents, such as thioflavin-T, bind to channels along surface side-chains of cross β-sheets(56), which are common structures in all amyloids, and 2) ligands that bind specifically to a particular amyloid structure (e.g. NFT or SF tau) target binding sites specific to the structure of β-helices that form fibril cores, which are arranged differently for Aβ(1-40), Aβ(1-42), PHF and SF fibrils(53, 54). Importantly for the development of anti-amyloid therapies, differences in fibril core structures combined with knowledge of genetic modifications provide strong evidence that alteration to certain residues promotes self-aggregation and could potentially be targeted to prevent aggregation from occurring. With regard to PET radioligands, considerable evidence demonstrates that the binding of PET radioligands to protein aggregates is entirely dependent on secondary, tertiary, and/or quaternary protein conformations that are present in pathological amyloid aggregates(50, 57-59). The recently elucidated molecular structure of PHF and SF fibrils offers a complimentary explanation for why NFT PET radioligands preferentially bind to PHF tau (dominant in AD) over SF tau (dominant in non-AD tauopathies) aggregates(58, 60). Cryo-EM findings indicate PHF and SF tau fibrils are composed of the same R3-R4 cores with cross-β conformations, but differ in the configuration of core β-helices and heterogeneous peripheral organization beyond the fibril core. Combined, PET and structural biology findings suggest that the differences between PHF and SF tau fibrils in the core β-helix or peripheral motifs alter the accessibility of radioligand binding sites(53). These findings also highlight the importance and potential of using a multi-disciplinary approach that ties together structural biology, physics, chemistry, engineering, and medicine to enable novel therapeutic and diagnostic strategies for clinical applications.

Prior to the availability of structural information, the identification of candidate molecules for human PET amyloid imaging has involved exhaustive screening of hundreds to thousands of chemicals using *in vitro* binding assays and autoradiography in human tissue samples with a trial-and-error approach(50). Promising ligands then proceed to preclinical studies in rodents and/or non-human primates to assess *in vivo* pharmacokinetic, metabolic properties, and, in some cases, binding patterns. Unfortunately, phylogenetic differences between humans, rodents and nonhuman primates have resulted in a lack of translation from preclinical evaluation to human subjects. This is particularly true in AD due to Alzheimer’s disease being largely a human phenomenon, as evidenced by the lack of nonhuman primate(61) and rodent(62) models that express human-like Aβ plaque and NFT pathologies and cognitive deficits with or without genetic modification(50). This lack of human-like AD features in preclinical models limits their usefulness for radiopharmaceutical development of Aβ-, NFT-, or other amyloid-specific radioligands.

PET Imaging of Beta-Amyloid Plaques and Neurofibrillary Tangles

Despite the considerable challenges in developing amyloid-specific radiotracers, PET imaging of Aβ plaques, and more recently, NFTs has been achieved in humans. [^{11}C]Pittsburgh Compound-B (PiB) was the first reported Aβ-specific PET radioligand to be used for human brain imaging(63). [^{11}C]PiB binds reversibly and with high affinity (K_D=6nM) to neuritic Aβ plaques, but with lower or negligible affinity diffuse Aβ plaques and other amyloids(59, 64), which also provides further evidence that the specificity of PET amyloid imaging agents is motif dependent. Since initial development and characterization, [^{11}C]PiB has been used extensively to interrogate interactions between Aβ plaques, glucose metabolism (using [^{18}F]FDG PET), cerebral blood flow (using [^{15}O]water and MRI), atrophy, and cognitive deficits in a wide array of clinical and preclinical (i.e. at-risk pre-symptomatic) cohorts(65-74). These large-scale PET imaging studies and the distribution limitation of the ^{11}C label (i.e. short half-life) prompted the development of ^{18}F-labeled Aβ-specific PET imaging compounds, and ultimately paved the way for limited FDA approval of several PET radiotracers to be used clinically as a diagnostic aid to rule out AD dementia(75, 76).

PET radioligands for NFT-specific imaging have only recently become available (~2013)(77-80), but have been rapidly integrated into multi-modal, multi-tracer investigations of AD pathophysiology(81-85). Preliminary investigation of NFT PET radioligands has indicated strong correlations between regional and global measures of NFTs with glucose hypometabolism, MRI measures of atrophy, and cognition in MCI and early dementia stages of AD(81, 82, 84, 86, 87). These studies have also demonstrated agreement between neuropathological staging described by Braak and Braak(15), and *in vivo* binding patterns of NFT PET tracers(84, 88) with some notable exceptions. Imaging features of NFT PET radioligands are discussed further in Chapter 3.

Combined, Aβ and NFT PET imaging have shown promise for both differentiating clinically diagnosed AD from non-AD dementias, and discriminating patient groups within the AD continuum(45, 60, 84). In addition, multi-modal, multi-tracer neuroimaging studies show increasing promise for clarifying interactions between pathophysiological processes, which may have predictive value for informed diagnosis of pre-symptomatic individuals and differentiating patterns of disease from those present in normal aging(14, 89-92).

1.6 Statement of Aims and Dissertation Organization

This dissertation is organized into three central components with the common theme of facilitating large-scale longitudinal, multimodal, multi-tracer investigation of AD pathophysiology.

Aim 1: Automated Production of NFT PET Radiopharmaceuticals for Human Use

The demand for serial investigation of NFT pathophysiology requires safe, efficient, and reproducible radiosynthesis of PET radiopharmaceuticals. The focus of Chapter 2 is to characterize the effects of individual steps of the radiochemical synthesis, purification and formulation processes to create optimized, automated production routines for candidate NFT radioligands [^{18}F]THK-5351 and [^{18}F]MK-6240. These findings provide a template for optimizing production of radiofluorinated compounds, and present automated methods for routine production of NFT PET radioligands, which are characterized for human research use.

Aim 2: Characterization and Quantification of NFT PET Radioligands in Humans

Discovery of novel NFT PET radiopharmaceuticals and rapid integration into clinical research requires thorough investigation of imaging methodologies and characterization of *in vivo* binding. The primary goal of Chapter 3 is to assess three candidate radioligands ([^{18}F]THK-5317, [^{18}F]THK-5351, and [^{18}F]MK-6240) for imaging NFT pathophysiology in humans. In this chapter, pharmacokinetic properties and quantification methodology are investigated for each radioligand individually. Spatial binding patterns are then compared within and across the three radiotracers. The results provide unique insights into the applicability of these radioligands for NFT-specific PET imaging and contribute to understanding of the specificity of THK compounds.

Aim 3: Considerations for PET Imaging in Clinical Research Applications

Beyond radioligand development neuroimaging studies of neurodegenerative diseases require consideration for PET imaging protocols and the processing and analysis of longitudinally acquired data. Chapter 4 characterizes the human biodistribution and radiation burden of [^{18}F]nifene in humans and provides discussion of dosimetric considerations for multi-tracer investigation of AD pathophysiology. In Chapter 5, a semi-automated processing and analysis pipeline is described that incorporates a data structure amenable to longitudinal study. Additionally, the effect of PET attenuation correction methods on longitudinal PET binding estimates is investigated. Combined, these chapters facilitate safe and efficient study of neurodegenerative processes using PET and MR imaging.

The sixth and final chapter provides a summary of relevant findings contained in this work as commentary on potential future applications and areas for continued exploration.

CHAPTER 2 AUTOMATED RADIOCHEMICAL SYNTHESIS OF TAU PET RADIOPHARMACEUTICALS

Section 2.2 was adapted with permission from Elsevier from (93).

2.1 Radiopharmaceutical Production of PET Radioligands for Human Use

Developing PET radiopharmaceuticals is an arduous task that often involves screening hundreds to thousands of candidate ligands and preclinical evaluation(50). Once a candidate radioligand is identified, several studies are conducted to determine the potential efficacy for binding the target and evaluate whether the radiopharmaceutical will be safe for human use. These studies investigate proof of concept (i.e. the ligand will bind to the target with some level of specificity), toxicology, and initial estimates of radiation burden. The latter studies are often performed in rodents, and the results are extrapolated to humans. If merited, these preliminary investigations of efficacy and safety are then used to translate the radiopharmaceutical into human subjects for further evaluation. This process involves regulatory approval by the United States Federal Drug Administration, and/or local approval by an Institutional Review Board (IRB).

Regulatory Requirements of PET Radiopharmaceuticals

Manufacturing, testing and use of PET radiopharmaceuticals for human use are regulated by the United States (US) Food and Drug Administration (FDA). Code of Federal Regulations (CFR) Title 21 Part 212 specifies current good manufacturing processes (CGMP) for PET drugs with special consideration given to radioactive drugs for research use in 21 CFR § 361. In addition to 21 CFR, the United States Pharmacopeia (USP) annually publishes the United States Pharmacopeial Convention, which outlines standards for manufacture and testing of pharmaceutical agents. USP chapter <823> outlines the compounding requirements and testing of PET radiopharmaceuticals for human research use (Table 2.1). In addition to USP <823>, USP <1015> specifies processes and considerations for automated production of PET radiopharmaceuticals that are designed to reduce radiation exposure to radiochemists and other lab personnel while maintaining processing standards. Combined, these documents are intended to allow for the safe testing and evaluation of PET radiopharmaceuticals in human subjects, which is reflected in the FDA’s Investigational New Drug (IND) mechanism.

In addition to meeting regulatory requirements, the production methods must be optimized to meet the unique requirements of radiopharmaceutical production, which include reliability and efficiency of the processes and radiation burden to lab personnel in addition to quality control metrics. This chapter describes the optimization of automated radiosynthesis, purification and formulation of [^{18}F]THK-5351 and [^{18}F]MK-6240 for routine production of these radiopharmaceuticals for human research use.

Process	Requirements
Control of Components, Materials and Supplies	Establish Written Specification for components and storage conditions
	Log shipments of components
	Verify each batch of components are in compliance with specifications
	Store components according to established written guidelines
Compounding Procedure Verification	Establish written acceptance criteria for identity, purity, and quality
	Maintain written and verified compounding procedures
	Controls for computer and automated equipment
	Verification studies to test written procedure produces product that meets acceptance criteria
Stability Testing and Expiration Dating	Establish written specifications for expiration dating and storage conditions of the PET radiopharmaceutical based on stability testing
PET Radiopharmaceutical Compounding for Human Use	Establish written procedures for production of PET radiopharmaceuticals
	Ensure cleanliness and aseptic processing of procedures near sterile filtration and dispensing
	Ensure identity, quantity, suitability of components and material used in compounding
	Establish labeling procedures
	Establish a batch record for each catch of radiopharmaceutical and confirm the verified procedures were followed and documented
Quality Control	Establish written quality control tests and acceptance criteria (pH, visual inspection, determination of radiochemical purity and identity, determination of radionuclidic identity, specific activity, residual solvents)
	Membrane filter integrity test
	Endotoxin limit test (outlined in USP <85>)
	Sterility test initiated within 24 hours of sterile filtration
	Establish written procedures and conduct testing of equipment and procedures
	Initial results in batch record
	Accept or reject batch once quality control tests are completed
	Investigate and document unacceptable quality control tests
Sterilization and Sterility Assurance	Establish procedures that conform to USP <823> to ensure sterile processing is maintained, documented and performed

Table 2.1 USP <823> compounding Requirements PET Radiopharmaceuticals for Human Use

2.2 Optimization and Automated Radiosynthesis of [^{18}F]THK-5351

2.2.1 Background: Radiosynthesis of [^{18}F]THK-5351

The chemical synthesis of THK 2-arylquinoline compounds, including [^{18}F]THK-5351, has been previously described(80, 94, 95). Synthesis of [^{18}F]THK-5351 is accomplished through nucleophilic radiofluorination of the 2-tetrahydropyranyl-(OTHP-) protected tosylate precursor (S)-2-(2-

methylaminopyrid-5-yl)-6-[[2-(tetrahydro-2H-pyran-2-yloxy)-3-tosyloxy]propoxy]quinoline (THK-5352), followed by acid hydrolysis and neutralization (Figure 2.1).

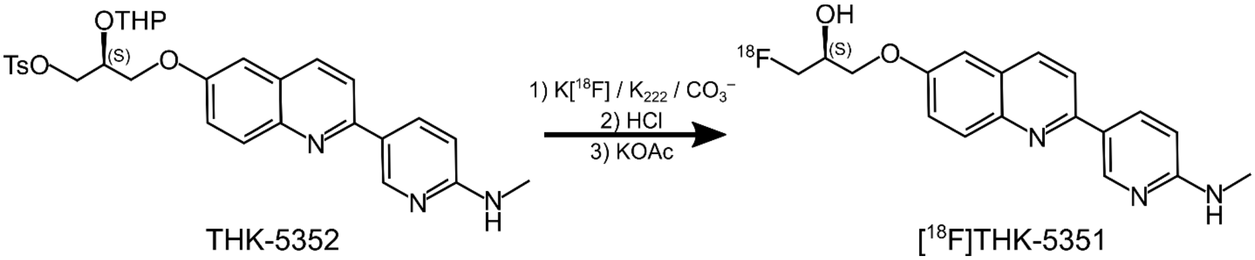

Figure 2.1 Radiosynthesis of [^{18}F]THK-5351

The crude product is purified using a combination of solid phase extraction(s) (SPE) and high-pressure liquid chromatography (HPLC) prior to final drug formulation. Previously reported methods provide adequate radiochemical yields and molar activity, but require 3 mg of THK-5352 (80, 94, 96), and one method requires a two-step elution of the pre-HPLC SPE step making it less amenable to automated methods. The goal of this section is to improve upon the previously described methods by reducing the amount of precursor used per batch, optimizing the intermediate SPE and subsequent HPLC purification methodology to make them more amenable to automation and reduce chemical impurities in the final product, investigate the radiochemical stability of formulated [^{18}F]THK-5351, and finally to automate the entire radiosynthesis, purification and formulation routine.

2.2.2 Materials and Methods

Materials

THK-5351 standard and precursor were synthesized and supplied by Tohoku University (95). Bulk precursor was dissolved in anhydrous DMSO (Thermo Scientific), aliquoted, and stored at ~5˚C. USP grade sterile water for injection (Baxter, SWI), sterile 0.9% sodium chloride for injection (saline, Hospira), and dehydrated ethanol (Decon Labs Inc.) were obtained from the University of Wisconsin (UW) Hospital, or through UW purchasing services, and were used without further purification. All other chemicals were purchased from Acros Organics, Fisher Scientific, and Sigma-Aldrich, and used without further purification. Sep-Pak Accell Plus QMA Plus Light cartridges (Waters Corporation) were preconditioned with 1 mL of 1M potassium bicarbonate followed by a 10 mL rinse with deionized (DI) water. The tC18 Sep-Pak Plus Light (Waters Corporation, tC18 light) and tC18 Sep-Pak Plus Short (Waters Corporation, tC18 short) cartridges were preconditioned with 5 mL of USP ethanol and rinsed with 10 mL of DI water (intermediate tC18 light) or SWI (formulation tC18 short) prior to use. Semi-preparative and analytical HPLC systems consisted of Waters 515 HPLC pump, Waters 2489 HPLC UV detector set at 360 nm absorbance (95), and in-line radioactivity detection (105-S, Carroll & Ramsey Associates). Semi-preparative HPLC purification used either an Inertsil ODS-4 (5µm, 10 x 250 mm, GL Sciences) or a Luna C18(2) (10µm, 10 x 250 mm, 100Å, Phenomenex) column. Analytical HPLC used an Inertsil ODS-4 column (5µm, 4.6 x 150 mm, GL Sciences) with 30:70 (v/v) acetonitrile:20 mM monobasic sodium phosphate mobile phase at a flow rate of 1.5 mL/min.

Radiosynthesis of Crude [^{18}F]THK-5351

Proton irradiation of [^{18}O]water (Huayi Isotopes, 98% enriched) was performed with the University of Wisconsin PETtrace cyclotron (GE Healthcare). Following irradiation with an integrated current of 4 – 25 µA·hr, 7 – 40 GBq of [^{18}F]fluoride in water was transferred to an ELIXYS automated radiosynthesizer where it was trapped on a preconditioned QMA cartridge. The [^{18}F]fluoride was eluted with 700 µL 80/20 (v/v) anhydrous acetonitrile/DI water with 5.6 mg 4,7,13,16,21,24-hexaoxa-1,10-diazabicyclo[8.8.8]hexacosane (Kryptofix® 222, K_{222}) and 1.7 mg potassium carbonate, and rinsed with 700 µL of anhydrous acetonitrile. The QMA eluate was azeotropically dried (x3) at 110˚C under vacuum and argon flow, with two subsequent additions of 1.5 mL anhydrous acetonitrile. Nucleophilic radiofluorination was carried out by adding THK-5352 precursor (0.1-3.0 mg) dissolved in DMSO and heating to 110˚C for 10 minutes. After cooling, hydrolysis of the O-THP protecting group was performed (200 µL 2N HCl, 110˚C for 3 minutes), followed by cooling and neutralization (200 µL of 2M potassium acetate (KOAc)).

^{18}F Nucleophilic Substitution Reaction Rate Determination

Radiofluorination rates were determined by autoradiography-visualized thin layer chromatography (radioTLC) for varying masses of precursor (0.1, 0.2 or 0.5 mg). This was performed to determine the minimum amount of THK-5352 needed to produce sufficient yields. Prior to eluting the QMA cartridge, K_{222} and K_2CO_3 masses were adjusted to match automated concentrations. Following azeotropic distillation of [^{18}F]KF/K_{222}/CO_3 solution, the residue was dissolved in 1 mL of DMSO and aliquoted in 300 µL fractions into three vials each containing different masses of precursor dissolved in 200 µL DMSO. Solutions were heated to 110˚C for 20 minutes and periodically sampled using capillary tubes. [^{18}F]KF/K_{222}/CO_3 DMSO standard and samples were spotted on silica TLC plates, developed in 80/20 (v/v) dichloromethane/methanol and imaged by storage phosphor autoradiography (Perkin Elmer). The percentage of reacted [^{18}F]fluoride was determined at each time point by calculating the percentage of activity within the lane that did not correspond to [^{18}F]fluoride (Rf = 0). As an additional measure of radiochemical yield, each reacted product was hydrolyzed (200 µL 2 N HCl, 3 minutes at 110˚C), neutralized (200 µL 2M KOAc) and SPE was performed (tC18 light, 6 mL DI water dilution, 6 mL DI water rinse). Decay corrected radiochemical yields were determined by dividing the radioactivity trapped on the tC18 by the total activity in the reaction vessel after subtracting residual radioactivity. Subsequently, the post-HPLC radiochemical yield was calculated by using the SPE and HPLC purification methods optimized below

tC18 Sep-Pak Light Ethanol Elution Profile

The use of a tC18 light cartridge was investigated to allow for a single-step elution of the intermediate tC18 cartridge while minimizing the total ethanol volume. This was done to make this process more amenable to automation while maintaining the long-term life of the purification column. The tC18 light ethanol elution profile was determined by stepwise elution of THK-5351 standard and [^{18}F]THK-5351 in separate experiments. Either 6.5 µg (20 nmol) of THK-5351 standard (in 200 µL DMSO) or crude [^{18}F]THK-5351 reaction product underwent solid phase extraction (tC18 light, 7 mL DI water dilution, 7 mL DI water rinse) with stepwise ethanol elution in 100 µL fractions. THK-5351 mass was determined for non-radioactive fractions (analytical HPLC) and the percentage of initial THK-5351 was calculated. For [^{18}F]THK-5351, trapped crude product and eluted fractions were radioassayed using a dose calibrator (CRC-15R, Capintec Inc.) and the percentage of trapped crude product was determined for each fraction after correction for radioactive decay.

Semi-Preparative HPLC Purification

Six semi-preparative HPLC conditions were investigated for purification of [^{18}F]THK-5351. One liter batches of mobile phase consisting of 18-25% (v/v) acetonitrile in 20 mM monobasic sodium phosphate buffer were created (18, 19, 20, and 22 % acetonitrile for Luna column, and 22 and 25 % acetonitrile for Inertsil ODS-4). To remove any residual precursor or other late eluting intermediates, HPLC columns were rinsed with 60/40 acetonitrile/DI water and equilibrated with at least 100 mL of mobile phase. Prior to HPLC injection, a single batch of [^{18}F]THK-5351 was synthesized and the crude product underwent SPE (tC18 Light, 4mL DI water dilution, 6 mL DI water rinse, eluted with 700 µL ethanol). The eluate was diluted in 1 mL SWI and fractioned into six equal parts. For each condition tested, 1/6th of the post-SPE product was injected onto the semi-preparative HPLC system. Mass peaks observed near [^{18}F]THK-5351, and early and late halves of the [^{18}F]THK-5351 product peak were collected in separate fractions which were characterized by analytical HPLC.

Automated Radiosynthesis using the Sofie ELIXYS

Radiosynthesis of ^{18}F-labeled compounds using the ELIXYS and a detailed report of the device features have been previously reported (97, 98). Seven automated productions (2 x 0.2 mg precursor, 3 x 0.5 mg precursor, 2 x 3.0 mg precursor) were carried out using the ELIXYS. The automated synthesis routine developed for the ELIXYS uses two of the three available cassettes and two reactors. Cassette one was loaded according to Figure 2.2, and reactor two was prefilled with 0.5 mL DI water. The following cassette routing was applied: SPE collection output of cassette one was attached to external addition line on cassette two, and the cassette two transfer tube was directly attached to the HPLC injector loading line.

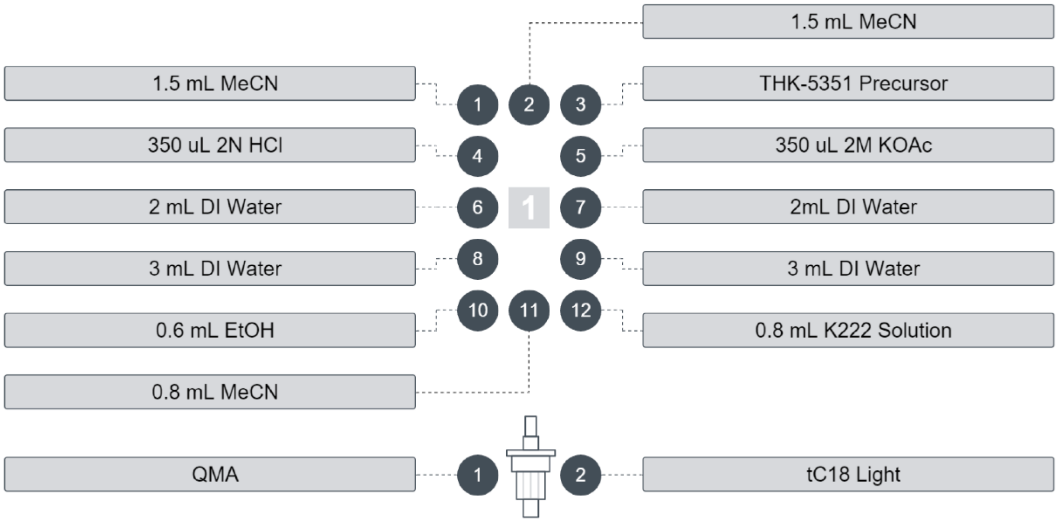

Figure 2.2 [^{18}F]THK-5351 ELIXYS Cassette 1 Setup

To minimize injecting air using the automated injector on the ELIXYS, the HPLC loading path, including the transfer tube, was preloaded with mobile phase and a check valve was added to the HPLC loop waste outlet to prevent the preloaded volume from leaking back into the system prior to post-synthesis HPLC loading. Due to residual losses of ~150 μL using automated additions, reagent volumes were increased to account for the loss of volume with the exception of the precursor dilution volume, which was fixed at 500 μL to avoid dilution during reactions. The following steps were carried out using the built-in unit operations:

1) [^{18}F]Fluoride was transferred from a sealed v-vial, trapped on a preconditioned QMA cartridge using the positive pressure line on the ELIXYS, and bulk [^{18}O]water was recovered.
2) The QMA cartridge was eluted into reactor one with K_{222}/K_2CO_3 solution (vial 12) and subsequently rinsed with anhydrous acetonitrile (vial 11)
3) Evaporation was carried out under vacuum and argon flush for 4.5 min at 110 ˚C, after which two subsequent evaporations were performed to visual dryness following anhydrous acetonitrile additions (vials 1 and 2, add path 1).
4) Precursor was added (vial 3, add path 1) to reactor one and the reactor was heated to 110˚C for 10 minutes in reaction position 1.
5) 2N HCl was added (vial 4, add path 2), and the reactor was heated to 110˚C for 3 minutes in reaction position 2.
6) 2M KOAc was added (vial 5, add path 2) to reactor one, followed by two additions of DI water (vials 6 and 7, add path 2).
7) Diluted crude product was trapped on a tC18 light using the SPE path on cassette one using the trap unit operation.
8) DI water (vials 8 and 9, add path 2) was added to reactor one, and passed through the tC18 light using the trap unit operation to rinse the cartridge.
9) Ethanol was added to reactor 1 (vial 10, add path 2) and used to elute the tC18 light cartridge into reactor two with stirring on using the elute unit operation and the output transferred to reactor 2.
10) The diluted and mixed eluate in reactor 2 was loaded onto the HPLC loop using the automated unit operation and injected onto semi-preparative HPLC.

Hardware and software were developed to perform HPLC data acquisition and fraction collection, post-HPLC purification SPE, and final formulation of [^{18}F]THK-5351 (see Appendix A). HPLC purification of crude ELIXYS product was carried out (19/81 (v/v) acetonitrile/20 mM monobasic sodium phosphate, 10 mL / min) using a new Luna column with a guard column (AJ0-7221 SecurityGuard™, Phenomenex) installed on the inlet. The HPLC fraction corresponding to [^{18}F]THK-5351 was collected into a pressure bottle prefilled with 45 mL SWI. SPE was performed using a preconditioned tC18 short cartridge (15 mL SWI rinse). The tC18 short cartridge was eluted with 1 mL ethanol, USP and flushed with 9 mL saline, USP, which were passed through an in-line sterile filter (SLFG025LS, EMD Millipore Corporation, Darmstadt, Germany) into vented (20G sterile venting needle, International Medical Industries, Pompano Beach, FL) 30 mL sterile empty vial (Hospira, Lake Forest, IL). System losses were characterized for two of the seven productions, and full characterization of the final drug product was performed for four of the seven productions according to USP chapter <823>.

Radiochemical Stability

During the production runs, breakdown of [^{18}F]THK-5351 was observed for activity concentrations ≥340 MBq/mL beginning around two hours post formulation. However, this had not been observed in our previous experience with formulating [^{18}F]THK-5351 manually. After investigating differences in the manual and automated formulation routines, we hypothesized that differences in the formulation vial head gas contributed to the radiochemical stability. To test this, the last two production runs (6 and 7) were formulated using the automated apparatus with USP air instead of ultra-high purity argon as a push gas, which had been used in the previous automated runs. Half of the volume (5 mL) was removed from the formulation vial, transferred aseptically into a separate vented 30 mL sterile empty vial, and purged with ultra-high purity argon for 1 minute. Samples of 200 µL were taken from both vials hourly and were characterized by analytical HPLC. Samples were tested for pH at end of synthesis (EOS) and four hours post-EOS and also tested for dissolved oxygen content at four hours post-EOS (CHEMetrics K-7501 and K-7512). Results are reported as mean ± standard deviation.

2.2.2 Results

^{18}F Radiolabeling Reaction Rates

RadioTLC indicated minimal increases (< 3 % higher at 20 minutes) in radiolabeling after seven minutes of reaction for all precursor masses tested (Figure 2.3). Radiochemical yields measured by radioTLC and SPE scaled with precursor mass. [^{18}F]THK-5351 decay-corrected radiochemical yields post-HPLC purification were 23%, 48%, and 55%, using precursor masses of 0.1, 0.2, and 0.5 mg, respectively.

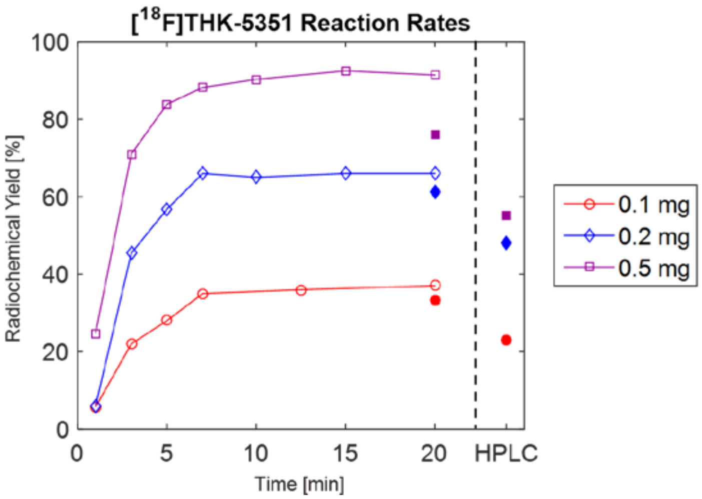

Figure 2.3 [18F]THK-5351 Nucleophilic Reaction Rates

tC18 Sep-Pak Light Ethanol Elution Profile

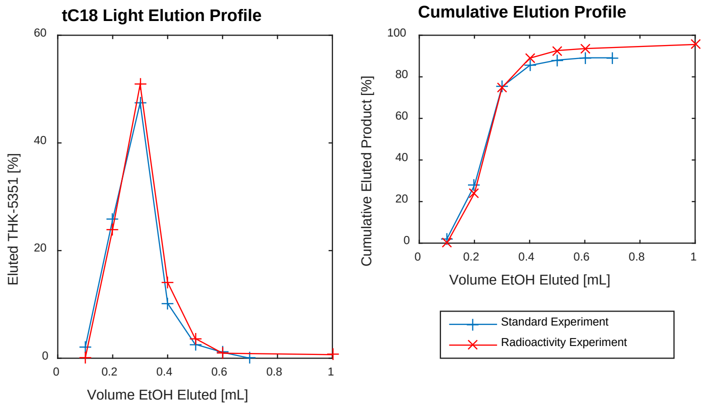

Figure 2.4 [^{18}F]THK-5351 tC18 Light Ethanol Elution Profile

Column	*Acetonitrile Concentration [%]*	*Flow Rate [mL / min]*	*Backpressure [kpsi]*	*THK-5351 Retention Time [min]*
Luna	22	5	1.8	20.08
Luna	20	7	2.8	20.90
Luna	19	9	3.3	21.02
Luna	18	9	3.4	26.13
ODS-4	25	5	2.2	18.93
ODS-4	22	7	3.2	21.13
Luna (New with Guard)	19	10	1.9	18.21

Table 2.2 [^{18}F]THK-5351 Semi-Preparative HPLC Conditions

The THK-5351 ethanol elution profile using the tC18 light cartridge was consistent in both the cold and radiolabeled experiments (Figure 2.4). Volumes greater than 0.5 mL ethanol only slightly increased (<3%) THK-5351 eluted product. In addition,

Impurity Number	*Analytical HPLC Retention Time [s]*
1	110
2	120
3	147
4	175
5	190
6	212
7	220
8	226
9	241
10	249
11	276
12	322

Table 2.3 Chemical Impurities Identified by Analytical HPLC

trapping efficiency of the intermediate crude product in 500 µL DMSO was not compromised with as little as 4 mL water dilution volume following radiofluorination, hydrolysis and neutralization.

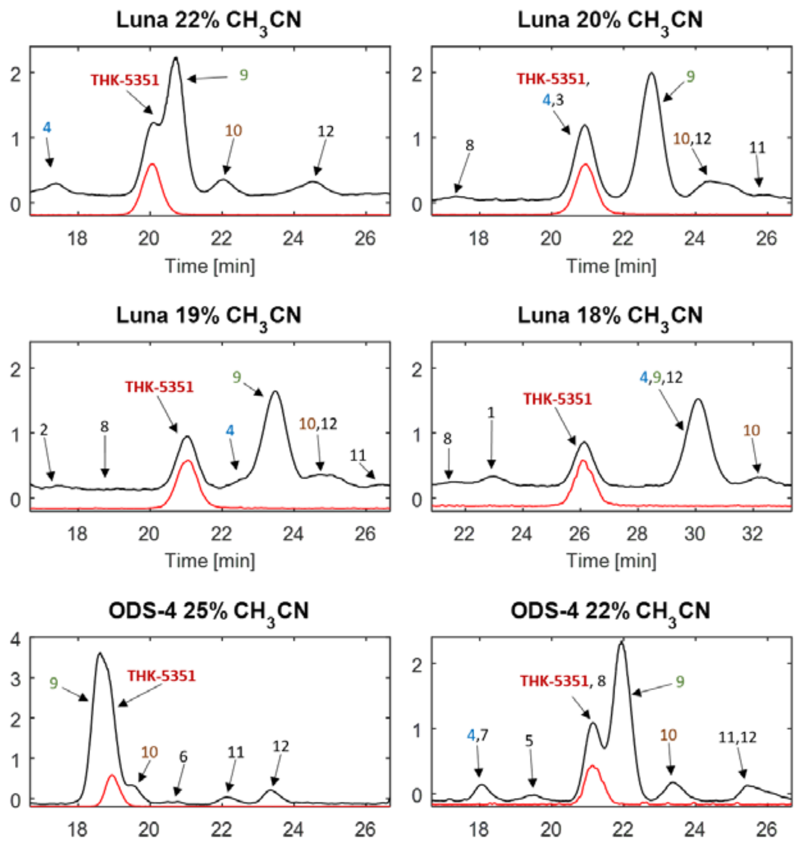

Figure 2.5 [18F]THK-5351 Semi-Preparative HPLC Radiochromatograms

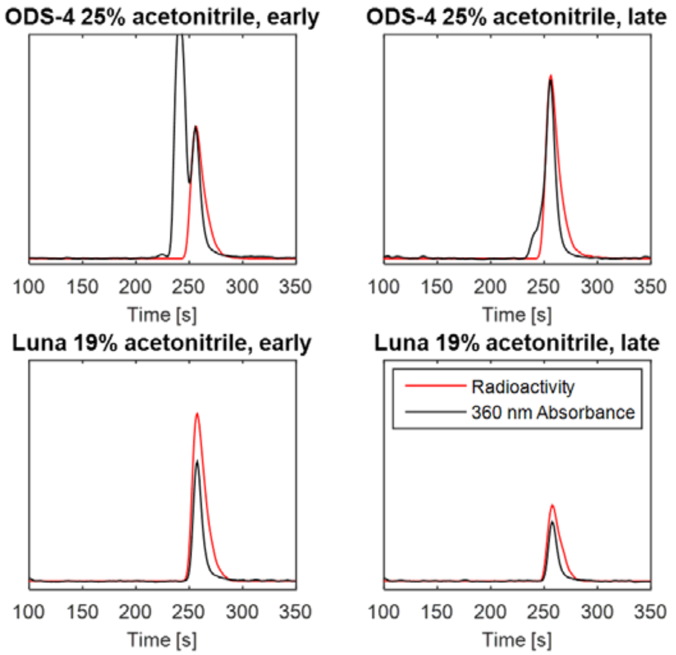

Figure 2.6 Analytical HPLC Comparison of Purified [^{18}F]THK-5351

Run	*Precursor Mass [mg]*	*Run Time [min]*	*NDC Yield [MBq]*	*NDC Yield [%]*	*DC Yield [%]*	*Molar Activity [MBq/nmol]*
1	0.2	100	1051	9.7	18.5	97
2	0.2	84	977	5.1	9.3	144
3	0.5	80	3437	13.5	22.7	317
4	0.5	83	2320	10.5	18.1	210
5	0.5	83	4740	12.3	21.5	322
6	3.0	88	5061	16.0	28.2	289
7	3.0	89	5099	15.6	27.8	635
Mean	**1.1**	**87**	**3200**	**11.8**	**20.9**	**290**
Std	**1.2**	**6**	**1700**	**3.5**	**6.0**	**160**

Table 2.4 Descriptive Statistics of ELIXYS Automated [^{18}F]THK-5351 Productions

Run	*[^{18}F] vial residual [%]*	*QMA Residual [%]*	*tC18 eluate [%]*	*tC18 cartridge residual [%]*	*tC18 waste [%]*	*ELIXYS unaccounted for [%]*	*HPLC Injection Residual [% of tC18 eluate]*	*HPLC, SPE and Formulation Recovery [% of injected eluate]*
6	0.4	17.6	37.3	1.5	34.7	8.5	13.5	87.6
7	0.5	15.6	37.4	1.6	36.9	8	15	87.4
Mean	**0.5**	**16.6**	**37.4**	**1.6**	**35.8**	**8.3**	**14.3**	**87.5**
Std	**0.1**	**1.0**	**0.1**	**0.1**	**1.1**	**0.3**	**0.8**	**0.1**

Table 2.5 Characterization of [^{18}F]THK-5351 Automated System Losses

HPLC Purification of [^{18}F]THK-5351

Table 2.2 gives the system backpressure, flow rates and THK-5351 retention times for the tested HPLC purification conditions. Analytical HPLC identified twelve closely eluting chemical impurities, which were numbered 1-12 in order of their retention time on analytical HPLC (Table 2.3). Five of these impurities were observed to co-elute to varying extents with [^{18}F]THK-5351 in at least one of the semi-preparative HPLC conditions tested. Semi-preparative separations using 20% or 22% acetonitrile with the Luna column and 22% or 25% acetonitrile with the ODS-4 column were unable to separate the identified chemical impurities from [^{18}F]THK-5351 (Figure 2.5). Using 18% or 19% acetonitrile mobile phase with the Luna column allowed for collection of the [^{18}F]THK-5351 peak without any observable chemical impurities on the analytic system (Figure 2.6). When using 3.0 mg of precursor and 19% acetonitrile with the Luna column, a chemical impurity (175s analytical retention time) was observed to co-elute on the tail of the [^{18}F]THK-5351 peak. However, this impurity was not observed during production runs using ≤0.5 mg of precursor with the same purification conditions.

Automated Production of [^{18}F]THK-5351

Results of the seven ELIXYS production runs are summarized in Table 2.4. The average run time from QMA loading to end of synthesis was 87±6 minutes with the longer runs being due to pausing the routine to radioassay system components. Syntheses without interruption typically took 80-84 minutes. The greatest radioactivity losses were due to radiolabeling efficiency, QMA elution efficiency, and residual losses during automated HPLC injection (Table 2.5). Data for the final drug product of the four of the ELIXYS syntheses that were fully characterized according to USP <823> are provided in Table 2.6. The automated ELIXYS routine combined with RadioChromaForm reliably produced [^{18}F]THK-5351 compliant with FDA regulatory requirements for research use of PET radiopharmaceuticals in humans.

Radiochemical Stability

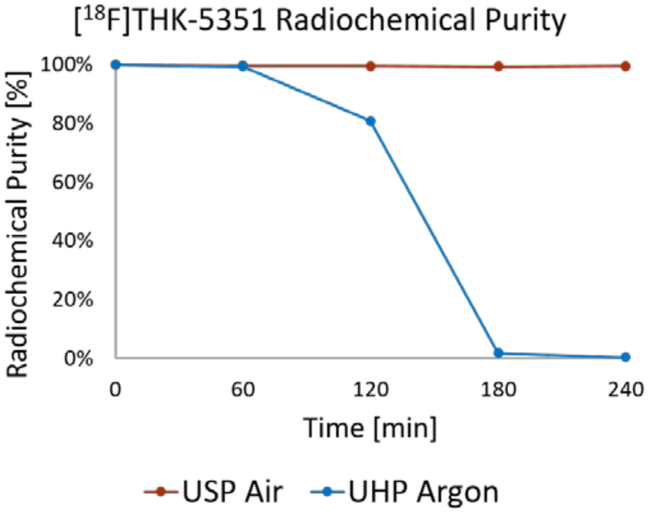

Figure 2.7 Radiochemical Stability of [18F]THK-5351 in Formulation

Chemical and radiochemical breakdown were observed in formulated [^{18}F]THK-5351 stored with argon head gas (Figure 2.7), but were stable (>99% radiochemical purity) up to four hours post-EOS when USP air was used. The formulated tracer stored in argon head gas was stable when tested at EOS (99.89%±0.07%) and one hour post-EOS (99.3%±0.1%), but deteriorated rapidly from 80.9%±6.7% radiochemical purity at two hours post-EOS to 1.6%±0.0% radiochemical purity by three hours, and 0.2%±0.1% by four hours post-EOS (n=2). In addition to radiochemical instability with argon head gas, all chemical products present on analytical HPLC at EOS, including impurities, were no longer observed four hours post-EOS. Dissolved oxygen content measured at four hours post-EOS indicated a significant decrease in the argon-stored sample (0.6±0.2 mg/L) compared to the sample stored in USP air (8±2 mg/L). All samples remained at a pH of 7.5 throughout the duration of study.

Test	Specification	Run #2	Run #3	Run #4	Run #5	Mean ± SD
Radiochemical Yield	EOS Yield	0.98 GBq (26.4 mCi)	3.44 GBq (92.9 mCi)	2.32 GBq (62.7 mCi)	4.74 GBq (128.1 mCi)	2.87 ± 1.39 GBq (77.5 ± 37.5 mCi)
Strength	Radioactivity concentration at EOS	97 MBq/mL	343 MBq/mL	232 MBq/mL	474 MBq/mL	287 ± 139 MBq/mL (7.8 ± 3.8 mCi/mL)
Visual Solution Inspection	Clear, colorless, and free of particulate matter	Pass	Pass	Pass	Pass	Pass
Vial Integrity	Intact	Pass	Pass	Pass	Pass	Pass
Membrane Filer Integrity	Bubble point > 13 psi	21	21	20	20	20.5 ± 0.5 psi
pH	4-8	7.2	7.2	7	7	7.1
Radiochemical Identity	Retention time within ±10 % of THK-5351 standard	1.5 %	1.9 %	0.8 %	1.1 %	1.3 ± 0.4 %
Radiochemical Purity	[^{18}F]THK-5351 peak > 90% of the sum of all radioactivity peaks	100 %	99.9 %	100 %	99.8 %	99.9 ± 0.1 %
Chemical Purity	Non-THK-5351 mass peaks < 3.7 µg in 10 mL (360nm abs)	< 0.2 µg (none detected)	< 0.2 µg (none detected)	< 0.2 µg (none detected)	< 0.2 µg (none detected)	< 0.2 µg (none detected)
Molar Activity	> 18.5 GBq / µmol	144 GBq/µmol	317 GBq/µmol	210 GBq/µmol	322 GBq/µmol	248 ± 75 GBq / µmol
Residual Solvents	Acetonitrile <0.41 mg / mL	Pass	Pass	Pass	Pass	Pass
Radionuclidic Identity	Half-life 105-115 minutes	108.6 min	109.0 min	108.4 min	109.5 min	108.9 ± 0.4 min
Radionuclidic Purity	>99 % of total counts at 511 keV, 1022 keV or Compton scatter	100 %	100 %	100 %	100 %	100 ± 0 %
Bacterial Endotoxin Testing	<17.5 EU / mL	< 2 EU / mL	< 2 EU / mL	< 2 EU / mL	< 2 EU / mL	< 2 EU / mL
Sterility	No growth at 14 days post-inoculation	No Growth	No Growth	No Growth	No Growth	No Growth
Residual Kryptofix 2.2.2	< 50 µg / mL (spot visibility less than standard)	No Spot, Pass	No Spot, Pass	No Spot, Pass	No Spot, Pass	No Spot, Pass

Table 2.6 Validation of Automated [^{18}F]THK-5351 Synthesis for Human Use

2.2.3 Discussion

Injection of crude reaction solvents, such as DMSO, is not recommended by column manufactures due to potential degradation to column performance and reduced column longevity. Performing SPE prior to HPLC purification greatly reduces potential to injection DMSO onto the purification column. In contrast to previous methods(95) that use a tC18 short cartridge with a larger dead volume, the tC18 light cartridge allows for a single-step elution of the cartridge making it more amenable to automation. A tC18 light cartridge could also be used prior to formulation of [^{18}F]THK-5351 to reduce the volume of ethanol in final formulation or to reduce the ethanol volume that needs to be evaporated where injection of ethanol is prohibited. Although, the higher cartridge backpressure is less favorable for SPE steps with gross dilutions and larger rinse volumes since more pressure is required to achieve the same flow rate.

When evaluating regular production methods for PET radiopharmaceuticals, one consideration is cost of production. In this section, it was shown that the total mass of precursor (THK-5351) can be dramatically reduced (factor of 6-30) from previous methods (96, 99) while providing adequate, and in the case of 0.5 mg comparable, radiochemical yields. This reduction in precursor mass is advantageous for both distribution centers and for single-injection sites that can further reduce the precursor mass to conserve precursor. Another advantage to reducing precursor mass is the improvement in HPLC purification, which was observed in this work when comparing batches made with ≥0.5 mg to batches made with 3 mg of precursor. An additional consideration that was not explored in this work is the dependence of radiochemical yield on the precursor mass concentration. Instead, a fixed volume (500 µL) was chosen based on previous experience with synthesizing [^{18}F]THK-5351 and the ability of automated devices to reliably add small volumes of reagents. Therefore, the reduction in radiofluorination yields with less precursor mass may also be attributed to a dilution effect complementary to a reduction in mass and should be further evaluated.

Differences in radiochemical yields were observed between the reaction rate experiment and the full automated synthesis routine. This difference can be attributed to QMA radioactivity losses (not accounted for in the reaction rate experiment), HPLC residual losses using the automated HPLC injection on the ELIXYS, and potentially loss of precursor mass and reagent volume due to the automated addition having high residual loss (~30%). These issues could be mitigated to varying extents by further QMA conditioning (data not shown), eluting the intermediate tC18 cartridge into a smaller external vial to avoid eluted product from sticking to the sides of the vessel, and using a manual addition line for precursor to minimize residual losses. Even without these modifications, decay-corrected yields using comparable precursor masses were similar to those previously reported,(96) although the total synthesis time was 20 minutes longer in the current work.

The most striking finding was the radiolytic decomposition observed with [^{18}F]THK-5351 when using an inert (argon) head gas, but not with USP air. This result is counterintuitive given proposed mechanisms for radiolysis of formulated radiopharmaceuticals that typically require the presence of oxygen for the formation of free radicals (100), although similar results have been observed in formulated ^{18}F-labeled PET pharmaceuticals in a Siemens patent (101). Further investigation into the interaction of vial head gas, PET isotope radioactive decay products, radioactivity concentration, and radioligand stability may provide insight into the mechanisms of radiopharmaceutical destabilization and degradation.

2.3 Optimization and Automated Radiosynthesis of [^{18}F]MK-6240

2.3.1 Background: Radiosynthesis of [^{18}F]MK-6240

The radiosynthesis of [^{18}F]MK-6240 has been previously described for preclinical (102) and human use (103). While both reports produce [^{18}F]MK-6240 in sufficient quantities for human studies, neither method is ideal for large-scale production. The first method used a temperature gradient microwave heating for the nucleophilic substitution for twelve minutes and involved rotoevaporation of the collected HPLC fraction prior to reconstitution in the formulation matrix (102). The second method used an automated synthesis, but requires a more complicated formulation matrix (10 mL 1 mg/mL ascorbic acid, 10 mL 0.9% sodium chloride for injection) that included HPLC mobile phase, and suffered from low [^{18}F]MK-6240 radiochemical yields (7.5±1.9% non-decay corrected after 90 minutes) (103). The goals of this section were to investigate using a SPE cartridge (tC18 light) for reformulation pre and post HPLC purification, improve the radiochemical yield of [^{18}F]MK-6240, automate the radiochemical production, and simplify the formulation matrix.

2.3.2 Materials and Methods

Materials

N-[(tert-butoxy)carbonyl]-N-(6-nitro-3-[1H-pyrrolo[2,3-c]pyridin-1-yl]isoqui-nolin-5-yl)carbamate ([^{18}F]MK-6240 precursor) was provided by Cerveau Technologies. Bulk precursor (up to 50 mg) was dissolved in anhydrous DMSO (Thermo Scientific) at a concentration of 1 mg per 100 µL and aliquoted into

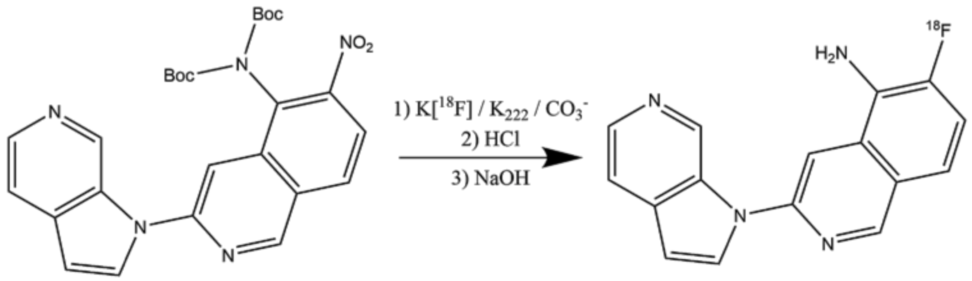

Figure 2.8 Radiosynthesis of [^{18}F]MK-6240

100 µL fractions in amber vials, which were sealed with Parafilm® (Bemis Company) and stored in a freezer at ~-20˚C until up to a month prior to synthesis when vials were placed in a ~5˚C refrigerator until immediately prior to the synthesis. USP grade SWI (Hospira), sterile bacteriostatic 0.9% sodium chloride for injection, USP (bacteriostatic saline, Hospira) and dehydrated ethanol (Decon Labs Inc.) were obtained from the UW Hospital or through UW purchasing services and were used without further purification. All other chemicals were purchased through Acros Organics, Fisher Scientific, and Sigma-Aldrich and used without further purification. Preconditioning of QMA, tC18 light, and tC18 short cartridges and the HPLC detectors, pumps and radiation detectors are described in section 2.2.2. Semi-preparative purification was performed with a Gemini C6-phenyl column (Phenomenex, 5 µm 110 Å, 250 x 10 mm) using 45% (v/v) ethanol, USP (Decon Labs) in 10 mM sodium acetate buffer mobile phase with a flow rate up to 4 mL / min. Analytical HPLC was performed using a Kinetex EVO C18 column (Phenomenex, 5 µm 100 Å, 150 x 4.6 mm) with 32% (v/v) acetonitrile in 10 mM dibasic sodium phosphate mobile phase at a flow rate of 2 mL/min. UV absorbance was set to 254 nm for both semi-preparative and analytical HPLC systems (102).

Radiosynthesis of [^{18}F]MK-6240

A schematic of the radiosynthesis is provided in Figure 2.8. Isotope generation, anion exchange and azeotropic distillation of [^{18}F]fluoride were performed as described in section 2.2.2. Nucleophilic radioflurination was performed on the ELIXYS radiosynthesizer(97) by addition of 1.0 mg MK-6240 precursor in 650 µL anhydrous DMSO followed by heating for 10 minutes at 140˚C and then cooled. Hydrolysis of the Boc protecting group was performed by addition of 750 µL 3N HCl (Lab Chem) and heating for 8 minutes at 90˚C (modification courtesy of Rachel Mulligan, Austin Health) followed by neutralization with 2.85 mL of 1M sodium hydroxide (Acros).

tC18 Sep-Pak Light Ethanol Elution Profile

The ethanol elution profile was characterized (n=2) using a tC18 light Sep-Pak cartridge. Crude [^{18}F]MK-6240 product was diluted with 2 mL DI water and trapped on a preconditioned tC18 light cartridge. The cartridge was stepwise eluted in 100 µL ethanol fractions with the eluate collected in a 50 mL Falcon tube (BD Biosciences), which was radioassayed (CRC-15R, Capintec) after the addition of each fraction. Radioassays were decay corrected and the percentage of radioactivity was determined using the total activity trapped on the tC18 cartridge as reference. Trapping efficiency was verified by collecting the waste from the trapping step, diluting it with 10 mL DI water, and trapping on a tC18 short cartridge, which was then rinsed with 10 mL DI water and eluted with 1 mL ethanol.

Automated Radiosynthesis using the Sofie ELIXYS and RadioChromaForm

Three automated productions were performed using the ELIXYS(97) and RadioChromaForm (see Appendix A). The ELIXYS sequence used two cassettes and two reactors. Reagents (except precursor) and preconditioned cartridges were loaded into cassette 1 as shown in Figure 2.9. The output of the SPE path from cassette 1 was routed to an external addition line on cassette 2. The HPLC injector loading line was connected to the output of the reactor 2 dip tube. Prior to synthesis, the HPLC injector was set to the load position using the calibration menu and the injection loop (5 mL) was back-loaded through the waste port with semi-preparative HPLC mobile phase to avoid air injection onto the HPLC system. Immediately prior to synthesis, dry ice and acetone were added to the vacuum trap Dewar and 550 µL anhydrous DMSO was added to a frozen precursor aliquot, which was then loaded onto the ELIXYS. ELIXYS unit operations were programmed to perform the following steps:

1) [^{18}F]Fluoride was transferred from a sealed v-vial, trapped on a QMA cartridge using the positive pressure line on the ELIXYS, and bulk [^{18}O]water was recovered.
2) The QMA cartridge was eluted into reactor one with K_{222}/K_2CO_3 solution (vial 1) and subsequently rinsed with anhydrous acetonitrile (vial 2) using the QMA elute unit operation.
3) Evaporation was carried out under vacuum and argon flush for six min at 110 ˚C, after which two subsequent evaporations were performed to visual dryness following anhydrous acetonitrile additions (vials 3 and 4, add path 1).

4) Precursor was added (vial 12, add path 1) to reactor one and the reactor was heated to 140˚C for 10 minutes in reaction position 1.

5) 3N HCl was added (vial 5, add path 2), and the reactor was heated to 90˚C for 8 minutes in reaction position 2.

6) 1M NaOH was added (vial 6, add path 2) to reactor one, followed by an addition of DI water (vial 7, add path 2).

7) Diluted crude product was trapped on a tC18 light using the SPE path on cassette one and the trap unit operation.

8) DI water (vials 8 and 9, add path 2) was added to reactor one, and the tC18 light cartridge was rinsed using the trap unit operation.

9) Ethanol was added to reactor 1 (vial 10, add path 2) and the tC18 light was eluted into reactor 2 with stirring on.

10) 10 mM NaOAc was added to reactor 1 (vial 11, add path 2), was passed through the tC18 light and was added to reactor 2 with stirring on.

11) The diluted and mixed eluate was loaded onto the HPLC loop by syringe suction through the waste port and was injected onto semi-preparative HPLC.

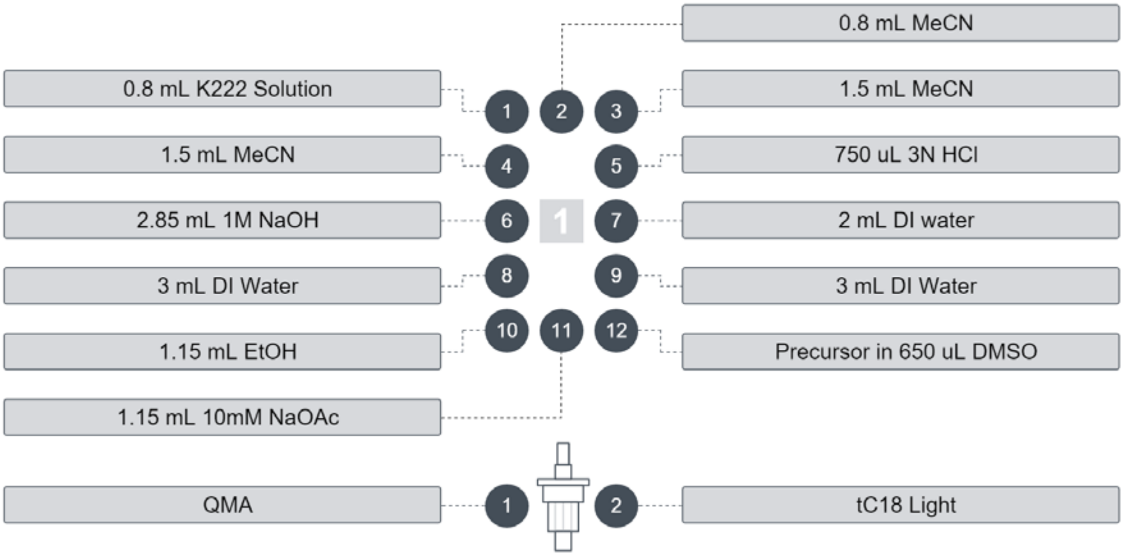

Figure 2.9 [^{18}F]MK-6240 ELIXYS Cassette 1 Setup

HPLC purification, post-purification SPE and final formulation were performed using RadioChromaForm and USP air for positive pressure additions. The radiofraction corresponding to [^{18}F]MK-6240 was collected into a 100 mL gross dilution bottle containing 35 mL SWI. Diluted product was trapped on a preconditioned tC18 short cartridge and the cartridge was rinsed with 15 mL SWI. The tC18 short cartridge was subsequently eluted with 1 mL dehydrated ethanol, USP and flushed with 9 mL bacteriostatic saline, USP, which were collected in a 30 mL sterile empty vial (Hospira, Lake Forest, IL) with a 20G sterile venting needle (International Medical Industries, Pompano Beach, FL) after in-line sterile filtration (SLFG025LS, EMD Millipore Corporation, Darmstadt, Germany). Final [^{18}F]MK-6240 product was tested according to USP <823> at EOS and stability tested at four hours post-EOS.

2.3.3 Results

tC18 Light Ethanol Elution

The [^{18}F]MK-6240 ethanol elution profile of the tC18 light cartridge is shown in Figure 2.10. One mL of ethanol was able to elute 90.0%±1.3% of the trapped radioactivity (n=2). Subsequent trapping of the waste product from the trapping and rinsing step on a tC18 short indicated trapping efficiency was maintained when using a total dilution volume (HCl, NaOH, and DI water) of 5 mL, which made automated SPE feasible on the ELIXYS without modification to the system.

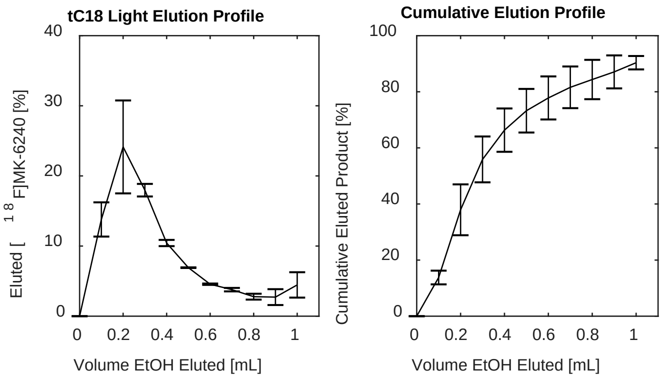

Figure 2.10 [^{18}F]MK-6240 tC18 Light Ethanol Elution Profile

Automated Production of [^{18}F]MK-6240

Non-decay corrected [^{18}F]MK-6240 radiochmeical yields relative to starting [^{18}F]fluoride were 11%±1% after 100±3 minutes using the combined ELIXYS and RadioChromaForm sequence. Product testing performed four hours post-EOS indicated radiochemical stability for activity strengths up to 334 MBq / mL using 10 % ethanol, USP in bacteriostatic saline. Characterization of the final product for validation

Test	Specification	Run #2	Run #3	Run #4	Mean ± SD
Radiochemical Yield	EOS Yield	3.34 GBq (90.2 mCi)	2.82 GBq (76.1 mCi)	2.13 GBq (57.6 mCi)	2.76 ± 0.60 GBq (74.6 ± 16.3 mCi)
Strength	Radioactivity concentration at EOS	334 MBq/mL	282 MBq/mL	213 MBq/mL	276 ± 60 MBq/mL (7.5 ± 1.6 mCi/mL)
Visual Solution Inspection	Clear, colorless, and free of particulate matter	Pass	Pass	Pass	Pass
Vial Integrity	Intact	Pass	Pass	Pass	Pass
Membrane Filer Integrity	Bubble point > 13 psi	20 psi	20 psi	20 psi	20 ± 0 psi
pH	4-8	7.5	7.5	7.5	7.5 ± 0
Radiochemical Identity	Retention time within ±10 % of MK-6240 standard	0.6 %	1.0 %	0.3 %	0.6 ± 0.3 %
Radiochemical Purity	[^{18}F]MK-6240 peak > 90% of the sum of all radioactivity peaks	99.7 %	99.5 %	99.6 %	99.6 ± 0.1 %
Chemical Purity	Non-MK-6240 mass peaks < 2.0 µg in 10 mL (360nm abs)	1.1 µg	1.2 µg	1.3 µg	1.2 ± 0.1 µg
Molar Activity	> 18.5 GBq / µmol	744 GBq/µmol	1032 GBq/µmol	860 GBq/µmol	879 ± 145 GBq / µmol
Residual Solvents	Acetonitrile <0.41 mg / mL	Pass	Pass	Pass	Pass
Radionuclidic Identity	Half-life 105-115 minutes	109.7	110.5	109.2	109.8 ± 0.6 min
Radionuclidic Purity	>99 % of total counts at 511 keV, 1022 keV or Compton scatter	100 %	100 %	100 %	100 ± 0 %
Bacterial Endotoxin Testing	<17.5 EU / mL	< 2 EU / mL	< 2 EU / mL	< 2 EU / mL	< 2 EU / mL
Sterility	No growth at 14 days post-inoculation	No Growth	No Growth	No Growth	No Growth
Residual Kryptofix 2.2.2	< 50 µg / mL (spot visibility less than standard)	No Spot, Pass	No Spot, Pass	No Spot, Pass	No Spot, Pass

Table 2.7 Validation of Automated [^{18}F]MK-6240 Synthesis for Human Use

radiochemistry indicated the combined automated radiosynthesis routine produced [^{18}F]MK-6240 radiopharmaceutical compliant with FDA regulatory requirements for investigational use in humans.

2.3.4 Discussion

SPE provides a quick and effective way of reconstituting radiopharmaceuticals prior to HPLC purification and final formulation. This work demonstrated that a tC18 cartridge can be used for reformulation of [^{18}F]MK-6240 with reasonable efficiency. However, given the relatively low radiochemical yields observed in this work (<15% non-decay corrected) it may be advantageous to eliminate the SPE steps before and after HPLC purification to reduce synthesis time (~12 minutes using the ELIXYS, ~5 minutes using RadioChromaCollector) and decrease losses due to cartridge trapping and eluting efficiencies. An advantage to using SPE for final product reformulation is that the volume of ethanol can be fixed, whereas methods that directly collect the ethanol-based mobile phase(103) will have variable volumes of ethanol in the final product, which depend on the duration of fraction collection and are higher (~3 mL) compared to the SPE approach (1 mL). In addition, the use of a tC18 cartridge prior to HPLC purification greatly reduces the amount of unreacted [^{18}F]fluoride in the HPLC waste reservoir, which is desirable to reduce shielding requirements for the purification system.

A key consideration when producing radiopharmaceuticals is radiochemical yield. Compared to previous methods(103), the method presented in this work improves NDC radiochemical yields by nearly 70% despite the total automated synthesis time being about 10 minutes longer than the previous report. Differences in NDC yield is potentially due to differences in the nucleophilic reaction temperature and reagent (DMSO vs DMF), hydrolysis conditions, and residual system losses, all of which were not formally evaluated. It is also worth noting that radiochemical yields have improved since the validation runs after performing system maintenance and modification to the ELIXYS (replacement of cassette one with a new cassette, swapping the anion exchange stopcocks with nylon stopcocks (Kimble® 420163-4503, DWK Life Sciences) and replacing the SPE stopcock with an external 3-way valve (HV3-3, 86727, Hamilton Company)). Since maintenance and system modification, the average radiochemical yield is 15.3%±2.4% (n=35 productions), slightly two times higher than the previous report. Radiochemical yields may potentially be further improved though modification the nucleophilic radiofluorination by increasing the mass of

Kryptofix, which has been shown to increase radiofluorination yields for other PET radioligands(104), or incorporating a more reactive leaving group into the MK-6240 precursor(105).

Another contributing factor to radiochemical yield is the duration of the synthesis. In the present work, the entire automated production took 100 minutes resulting in 53% loss due to radioactive decay alone. In addition to removing the SPE steps mentioned in the first paragraph of the discussion, a 2-step azeotropic distillation could be implemented (instead of 3-step) to reduce the total synthesis time. Combined, these changes would result in ~22 minutes synthesis resulting in a 15% increase in NDC yield due to radioactive decay and potentially another 23% increase due to SPE losses. It is worth noting that acetonitrile based separations (see appendix B) produced [^{18}F]MK-6240 that met chemical purity limits with shorter retention times (13 vs. 25 minutes), but were not used due to low HPLC recovery likely caused by radiolytic decomposition occurring during the separation. The addition of ethanol to the acetonitrile-based purification mobile phase may improve stability of [^{18}F]MK-6240 during the purification separation, thereby improving the recovery and simultaneously reducing the purification time, but this should be further evaluated.

The formulation matrix for PET radiopharmaceuticals is a balance between simplicity and radiochemical stability. Ethanol has been shown to improve radiochemical stability of ^{18}F-labeled compounds(106) and is thought to act as an oxygen free radical scavenger. Previous methods used an antioxidant (ascorbic acid), presumably as a formulation stabilizing agent. The results from the present work suggest that 10% (v/v) ethanol is sufficient to stabilize [^{18}F]MK-6240 in formulation at comparable activity strengths reported elsewhere(103). An advantage to the formulation method investigated in this work is that the total injection volume can be reduced (nearly three times), which can improve patient comfort, particularly for long scan durations. Interestingly, [^{18}F]MK-6240 radiochemical decomposition was observed when testing different HPLC purification methods (see Appendix B) that did not use an ethanol in the mobile phase even with low activity concentrations (70 MBq / mL), but were stable when using ethanol-based mobile phase. These results combined with the radiochemical stability observed in 10% (v/v) ethanol formulation further support the hypothesis that ethanol is a radiochemical stabilizing agent for [^{18}F]MK-6240.

2.4 Radiochemistry Discussion and Conclusions

Radiopharmaceutical production is a detailed, multi-step process. The work in this chapter demonstrates that small differences (e.g. vial head gas, ethanol content) within individual steps can have profound effects on the resultant radiotracer product. The optimized procedure involves balancing tradeoffs within the context of the application of use. Factors for optimization include foremost the quality of the injectable product and participant safety, radiochemical yield and quantity of studies, duration of processes and isotope half-life, radiation dose to lab personnel, the reliability and efficiency of the synthesis routine, and the longevity of system components. The implementation of automated and remotely operated systems allows for safe and reliable radiopharmaceutical production that minimizes radiation exposer to lab personnel. Finally, the results in this chapter reinforce the need to perform validation radiochemistry whenever the synthesis procedure or integrated systems are modified to confirm the radiopharmaceutical product is not adversely affected.

CHAPTER 3

IN VIVO EVALUATION OF NFT TAU PET RADIOLIGANDS

Section 3.3 was adapted with permission from *The Journal of Nuclear Medicine* from (107).

Section 3.4 was adapted with permission from *The Journal of Nuclear Medicine* from (108).

Once PET radioligands have been radiolabeled and have demonstrated efficacy and safety in preclinical models, human studies are conducted to evaluate the in vivo properties of the radioligand. These studies involve characterizing the biodistribution and radiation burden, and pharmacokinetic properties of the tracer and evaluating quantification strategies and the binding specificity of the radioligand to the target receptor. The focus of this chapter is to evaluate novel PET radioligands for imaging NFT pathology in human subjects.

3.1 PET Imaging of NFT Pathology

Following the success of the Aβ PET radioligand [^{11}C]PiB(63) and the FDA approval of several Aβ PET ligands(109) for ruling out AD clinically, research intensified for developing NFT-specific radioligands. [^{18}F]FDDNP was the first PET radiopharmaceutical to be identified for binding NFTs in humans(110). However, FDDNP has moderate affinity for both NFTs and Aβ plaques, which co-localize in AD, and thus this radiotracer lacks the specificity for monitoring these individual pathological processes. Nearly a decade after the discovery of FDDNP, research groups began reporting early successes with first-generation NFT-specific PET radioligands that had selectivity for NFTs over Aβ plaques and had favorable physicochemical properties for NFT PET neuroimaging.

Among these first generation radioligands was [^{11}C]PBB3 developed by the National Institute of Radiological Sciences (Chiba, Japan)(78), the Siemens developed thioflavin-S derivatives [^{18}F]T808 and [^{18}F]T807 (also called [^{18}F]AV-1451 and flortaucipir)(58, 111), and arylquinoline derivatives [^{18}F]THK-523, [^{18}F]THK-5105 and [^{18}F]THK-5117(79, 80) (the THK series) developed by Tohoku University (Sendai, Japan). These tracers, in particular [^{18}F]T807, were rapidly incorporated into validation and neurodegenerative disease studies(81, 82, 84, 87, 112, 113) despite having varying degrees of unfavorable characteristics. [^{11}C]PBB3 was discovered to have non-polar radiometabolites, which entered the brain and complicated analysis(114). [^{18}F]T807, despite being the most widely used NFT PET tracer is known to have off-target binding in the basal ganglia and choroid plexus, thought to be attributed to monoamine oxidase-

A (MAO-A) and neuromelanin, respectively(60, 82). [^{18}F]THK-523 and [^{18}F]THK-5105 indicated poor brain penetrance and slow in vivo kinetics, which were improved with [^{18}F]THK-5117, but these first-generation THK compounds exhibit high non-specific WM and basal ganglia binding(80).

The next (second) generation of NFT radiotracers are being developed to overcome the shortcomings of these first-generation compounds. Among the second-generation candidates for NFT PET imaging are [^{18}F]AM-PBB3 and [^{18}F]PM-PBB3(115), [^{18}F]THK-5351(116), [^{18}F]MK-6240(102, 117), [^{18}F]GTP1(118), [^{18}F]PI-2620(119) (aka MNI-960), and [^{18}F]JNJ64349311(120), and [^{18}F]RO6958948(121). Most of these compounds have had limited development in human subjects. This chapter focuses on evaluating *in vivo* pharmacokinetic properties, quantification strategies and the binding distribution of [^{18}F]THK-5317 ([^{18}F](S)THK-5117), [^{18}F]THK-5351, and [^{18}F]MK-6240 in human subjects.

3.2 Pharmacokinetic Modeling and Specific Binding Quantification of PET Radioligands

Receptor-Ligand Modeling

The goal of PET neuroimaging studies is to detect and quantify the density of radiotracer targets (e.g. NFTs, Aβ plaques, neuroreceptors, etc.). For reversibly bound radioligands, quantification involves applying compartment models that describe the distribution of the tracer within the blood plasma and tissue space. The receptor-ligand model, proposed by Mintun and collegues(122), consist of four compartments the radiotracer can occupy and first-order rate constants that describe the influx and efflux between compartments (Figure 3.1). The first compartment is the free tracer in blood plasma. The other three compartments are within the tissue space where the radioligand can be free in tissue plasma, non-specifically bound, or specifically bound to receptors. The non-specific and free tissue compartments

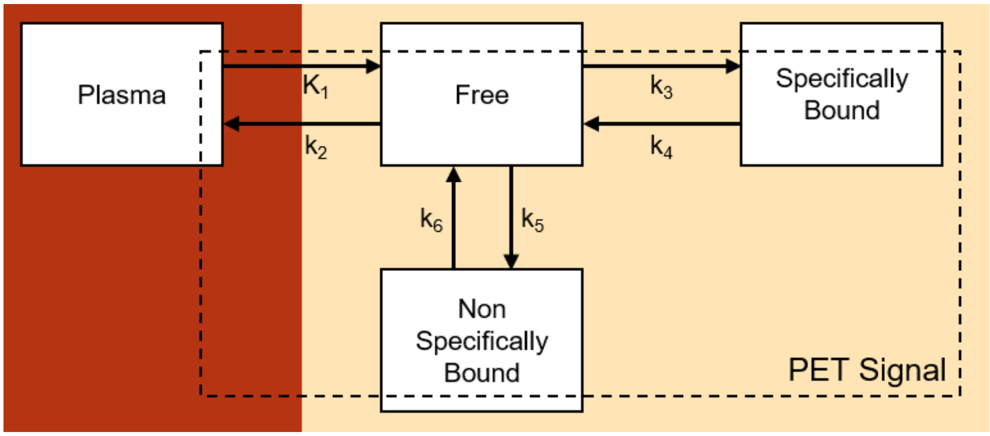

Figure 3.1 Receptor-Ligand Kinetic Model

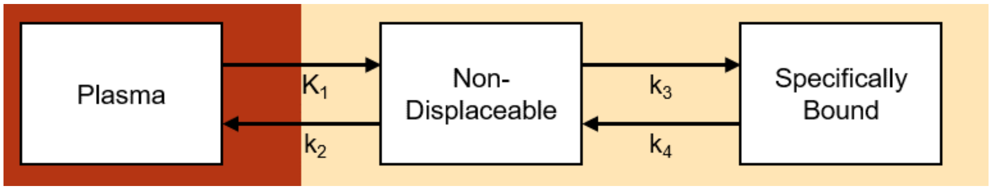

Figure 3.2 Two-Tissue Compartment Model

can be combined into a single, non-displaceable compartment if the exchange between these two compartments is sufficiently rapid. This model is referred to as the two-tissue compartment model (2TCM, Figure 3.2) and is the underlying foundation for quantification of receptor-ligand systems in the PET neuroimaging studies(122, 123).

The gold standard for pharmacokinetic characterization of PET tracers involves directly measuring the radioactivity concentration in the arterial blood and using the measured data as an input function to generate model data that are compared to measured 4D PET data to estimate the rate constant parameters. Uniquely identifying kinetic parameters is often confounded by parameter covariance, but ratios of kinetic parameters are often more reliable and provide physiological interpretation. One such macro parameter is the total distribution volume (V_T), which is defined in PET neuroimaging as the ratio of the concentration of tracer within a volume in the brain to the radiotracer concentration in blood plasma at equilibrium and is interpreted as the amount of blood plasma that would be required to have the same mass of drug as a volume of tissue(123). While V_T gives information about the distribution of tracer in tissue, the parameter of interest in PET receptor studies is the binding potential (BP), which under low (tracer) mass conditions is directly proportional to receptor density (B_{max}) and the receptor-ligand affinity ($1/K_D$), and can be related to the in vivo PET concentration of specifically bound (C_S) and free tracer (C_{FT}) in tissue.

$$BP = \frac{B_{max}}{K_D} = \frac{C_S}{C_{FT}} \qquad \textit{(Equation 3.1)}$$

While the specifically bound component is of interest since it describes the tracer that is bound to the receptor site, the PET signal is a combination of the three tissue compartments that cannot be independently measured without perturbing receptor-ligand binding. Therefore, an alternative definition of the binding potential is implemented the uses the non-displaceable signal as the reference for comparison.

$$BP_{ND} = \frac{V_S}{V_{ND}} = \frac{V_T - V_{ND}}{V_{ND}} = \frac{V_T}{V_{ND}} - 1 = DVR - 1 \qquad \textit{(Equation 3.2)}$$

This definition of the binding potential allows for the direct estimation of BP_{ND} or the distribution volume ratio (DVR) that 1) are proportional to receptor density, 2) can be obtained using a single dynamic PET scan acquired from the injection of the radiotracer, 3) do not require arterial blood sampling. BP_{ND} has physiological interpretation where values greater than zero (i.e. DVR > 1) imply specific (target receptor) binding of the radioligand. The concept of BP_{ND} is similar to the signal-to-noise ratio where the non-displaceable component comparable to the noise floor, and the specifically bound component is the signal of interest.

Reference Tissue Methods for Binding Quantification

Since PET studies involving arterial blood sampling are procedurally complex and impractical for large-scale clinical research studies, simplified approaches are advantageous. Reference tissue methods allow for direct estimation of DVR or BP_{ND} parameters from 4D PET data without requiring arterial cannulation, so long as a reference region of non-displaceable binding (i.e. a region devoid of target receptors with minimal specific binding) exists. Using a bolus injection, time activity curves are extracted for the reference region and regions of interest (ROIs). DVR or BP_{ND} are then estimated by applying graphical analysis (reference Logan graphical analysis (LGA), Equation 3.3, (124)), multiple regression analysis (multilinear reference tissue model, MRTM, Equation 3.4, (125)), or non-linear regression (simplified reference tissue model, SRTM, Equation 3.5, (126)) to transformed PET data. SRTM can be implemented using a basis function approach to make the optimization problem linear and reduce parameter noise and divergent solutions(127, 128). Additionally for MRTM and SRTM, the reference region k_2 parameter can be estimated and fixed (because it refers to the tissue efflux of the reference region) for a second iteration of parameter fitting to reduce estimated parameter noise (referred to as MRTM2(129) and SRTM2(130), respectively).

Parameter	Definition
C_T	Tissue Concentration
C_R	Reference Tissue Concentration
k_2	Tissue-to-Plasma Efflux Constant
int	Model Independent Intercept
b	Model independent fitting parameter
R_1	Ratio of K_1 between target and reference tissues
t	Time
DVR	Distribution Volume Ratio
BP_{ND}	Binding Potential Relative to Non-Displaceable Signal

Table 3.1 Reference Tissue Model Variable Definitions

$$\frac{\int_0^T C_T(t)dt}{C_T(t)} = DVR\left[\frac{\int_0^T C_R(t)dt + C_R(T)/\overline{k_2}}{C_T(T)}\right] + int \qquad \textit{(Equation 3.3)}$$

$$C_T(t) = -\frac{DVR}{b}\int_0^T C_R(t)dt + \frac{1}{b}\int_0^T C_T(t)dt - \frac{DVR}{k_2' b} C_R(T) \qquad \textit{(Equation 3.4)}$$

$$C_T(t) = R_1 C_R + \left[k_2 - \frac{R_1 k_2}{1+BP_{ND}}\right] C_R \otimes e^{-k_2 t/(1+BP_{ND})} \qquad \textit{(Equation 3.5)}$$

While LGA, MRTM and SRTM provide quantitative estimates of DVR or BP_{ND}, they require full dynamic data acquisition from tracer injection for a period of time determined by the *in vivo* pharmacokinetic properties of the radioligand. A further simplification involves taking the ratio of the standard uptake values (SUV = C_{PET} x body mass / injected dose) in a target region to the reference region, which is referred to as the standard uptake value ratio (SUVR) and is equivalent to the ratio of the PET concentrations in the respective regions ($C_T(t)$ / $C_R(t)$). Compared to DVR, SUVR analyses allow for parameter calculation using shorter scan durations, but are susceptible to bias due to differences in plasma clearance between low and high binding regions(131).

3.3 In Vivo Characterization and Quantification of [^{18}F]THK-5317 and [^{18}F]THK-5351

3.3.1 Overview of Arylquinoline Derivatives

The THK series developed by investigators at Tohoku University showed early promise for *in vivo* detection of AD NFT pathology. *In vitro* studies indicated THK-5117 has affinity for NFTs over Aβ plaques and binding patterns consistent with AD tau deposits in autoradiography experiments(57, 80, 132). THK-5117 also demonstrates binding in other non-AD tauopathies(133), binds to the combination of 3R and 4R isoforms found in paired helical filament tau aggregates both intracellularly and extracellularly (ghost tangles), and is sensitive to beta-sheet disruption(57), suggesting protein conformation plays a key role in tracer binding. THK-5117 is a racemic mixture of (R) and (S) stereoisomers, which could preclude accurate *in vivo* quantification. Both enantiomers show similar spatial distributions in autoradiography, but S-enantiomers of THK compounds display higher affinity for human NFTs in AD and faster in vivo kinetic properties in rodents(134). PET imaging of ^{18}F-THK-5317 (racemically pure [^{18}F]-(S)THK-5117) with arterial blood sampling in subjects with MCI and AD demonstrates favorable *in vivo* kinetics, which can be modeled with using the 2TCM in target regions(135). BP_{ND} and DVR binding estimates using reference tissue methods (SRTM(127), SRTM2(130) and Logan(124)) demonstrated agreement with binding measures derived from arterial sampling. Both THK-5117 and THK-5317 show high non-specific WM binding, which may limit accurate quantification in adjacent GM regions and visual assessment in clinical applications(87, 94, 135). Despite these potential confounds, cross-sectional and longitudinal studies demonstrate the utility of [^{18}F]THK-5117 and [^{18}F]THK-5317 for monitoring the *in vivo* spatial distribution of NFT tau (86, 87, 136).

[^{18}F]THK-5351, the antecessor to [^{18}F]THK-5117, is chemically similar to the optically pure THK-5317(94). The substitution of a pyridine for benzene at the 2-aryl group decreased the lipophilicity of the molecule (Log P = 1.5 vs. 2.3) in an effort to reduce non-specific WM binding(95). *In vitro* and *in vivo* investigation of THK-5351 is consistent with THK-5117 in selectivity for NFTs over other amyloids and yielded a higher affinity in hippocampal brain homogenates of AD brains when compared to THK-5117(94). *In vivo* comparison in two AD subjects indicates [^{18}F]THK-5351 has reduced WM binding, lower brain uptake, and slightly faster pharmacokinetic properties in GM compared to THK-5117. A recent study suggests reference LGA using 60 minutes of dynamic data and SUVR (40-60 minutes post-injection) are suitable for binding estimation of THK-5351(137). While early study of [^{18}F]THK-5351 indicated promise for detecting *in vivo* NFT pathology, a recent study in humans has indicated [^{18}F]THK-5351 signal is reduced when participants are given an MAO-B inhibitor prior to the PET scan suggesting THK-5351 might also bind to MAO-B(138). More recently, *in vitro* study comparing several NFT PET radioligands indicated both THK-5351 and THK-5117 have affinity for MAO-B, but the ratio of NFT to MAO-B signal is considerably lower (~x5) for THK-5117 when compared to THK-5351(139). This section investigates and directly compares *in vivo* quantification methods and binding patterns of [^{18}F]THK-5317 and [^{18}F]THK-5351 in human participants ranging from cognitively normal older adults to persons with dementia.

3.3.2 Methods

Recruiting and Cohort Summary

Participants (N=28) were recruited from the University of Wisconsin Alzheimer's Disease Research Center (MCI and AD) or the Wisconsin Registry for Alzheimer's Prevention (WRAP, cognitively stable (CS) an cognitively declining (CD))(140, 141). The sample consisted of 18 APOE-ε4 carriers and 15 individuals with parental history of AD (Table 3.2). Participants were 53 to 85 years old (mean 71±7 years) and ranged from cognitively stable to frank dementia. At-risk individuals were grouped as cognitively stable (CS, n=9) or cognitively declining (CD, n=10) based on longitudinal neuropsychological evaluation(74). Amnestic MCI (n=3) and probable AD (n=6) groups were classified based on consensus diagnosis at the annual evaluation

Group	*Mean Age, Range [yrs]*	*Sex*	*APOE-ε4 Carriers*	*MMSE/ MoCa*	*PiB(+)*
Cognitively Stable (n=9)	66±8, 53-75	6F,3M	3	29.9±0.3	3
Cognitively Declining (n=10)	71±3, 65-75	4F, 6M	5 (1 N.A.)	28.9±1.0	4
MCI (n=3)	82±3, 80-85	1F, 2M	1	27.0±2.6	2
Probable AD (n=6)	70±7 ,61-82	4F, 2M	5	21.0±5.7 (n=2) 15.3±5.9	5
Total (N=28)	70 ± 7, 53-85	15F, 13M	18 (1 N.A.)		14

Table 3.2 THK Participant Descriptive Statistics

closest to scanning prior to the availability of tau and Aβ biomarker data. Fourteen subjects indicated elevated Aβ and 14 did not based on global [^{11}C]PiB DVR (see below). This study was approved by the Institutional Review Board and signature of written informed consent was obtained for all participants prior to participation in this study. [^{18}F]THK-5351 and [^{11}C]PiB PET scans were carried out under a FDA approved INDs, and [^{18}F]THK-5317 under the University of Wisconsin-Madison Radioactive Drug Research Committee.

Radiochemical Synthesis of [^{11}C]PiB

[^{11}C]PiB was synthesized as previously described(73, 142). Briefly, [^{11}C]methane was produced by ~50 μA·hr proton irradiation of a nitrogen target containing 10% hydrogen, cryogenically trapped at -180ºC, and converted to [^{11}C]methyl iodide by multiple pass iodination. [^{11}C]methyl trifluoromethanesulfonate was generated by reacting [^{11}C]methyl iodide with silver triflate at 190-200ºC using a multiple flow-through system (ScanSys, Denmark). [^{11}C]methyl triflate is then trapped in a solution containing 1 mg of 6-OH-BTA-0 ([^{11}C]PiB precursor) dissolved in 150 μL of methyl ethyl ketone. After up to 15 minutes of room temperature reaction, the crude product is purified by HPLC (35/65 (v/v) acetonitrile/50mM triethylamine phosphate buffer, 10 mL/min, 250x10 mm, Prodigy 10 µm PREP ODS 100Å, Phenomenex) and subsequent SPE (90 mL SWI dilution, C18 Sep-Pak Light, 10 mL SWI rinse). The SPE cartridge was then eluted with 1 mL of dehydrated ethanol, USP, flushed with 14 mL of bacteriostatic saline and in-line filtered (SLFG025LS, EMD Millipore Corporation) prior to collection into a vented 30 mL sterile empty vial (Hospira).

Radiochemical Synthesis of [^{18}F]THK-5351 and [^{18}F]THK-5317

[^{18}F]THK-5317 and [^{18}F]THK-5351 were synthesized similar to previously described methods(80, 94), but modified to improve purification. Notably, this work was performed prior to optimization and full automation of the [^{18}F]THK-5351 radiosynthesis, which differs slightly from the methods in Chapter 2. Generation of [^{18}F]fluoride and preparation of the [^{18}F]KF solution was performed as described in Section 2.2.2. [^{18}F]THK-5317 was synthesized using an automated chemistry module (Siemens Explora FDG4, Siemens Healthcare, Knoxville, TN) by performing twice azeotropic distillation of [^{18}F]KF/K$_{222}$/CO$_3$ solution, nucleophilic substitution of tosylate precursor (S)-2-(4-methylaminophenyl)-6-[[2-(tetrahydro-2H-pyran-2-yloxy)-3-tosyloxy]propoxy]quinolone ((S)THK-5119-2, Tohoku University, Sendai, Japan) for 10 minutes at 110˚C, and hydrolysis of the protecting group (THP) for 3 minutes at 110˚C, which was neutralized with 2M potassium acetate. Crude product was diluted with 7 mL DI water, trapped on a tC18 short cartridge, which was rinsed with 7 mL DI water. The cartridge was eluted with ethanol in 2 fractions (400 µL to waste, 700 µL collected). The collected SPE fraction was diluted with 700 µL DI water and purified by semi-preparative HPLC (Inertsil ODS-4 5µ 250x10 mm, GL Sciences, Inc., Tokyo, Japan, 60/40 (v/v) 20 mM monobasic sodium phosphate/acetonitrile). Subsequent SPE (35 mL SWI dilution, tC18 short, 10 mL SWI rinse) was performed to remove organic solvents. The second tC18 short cartridge was then eluted with 1 mL dehydrated ethanol, diluted with 9 mL 0.9% sodium chloride for injection, USP and passed through an inline 0.22 µm sterile filter (SLFG025LS, EMD Millipore Corporation), and collected in a vented 30 mL sterile empty vial (Hospira). [^{18}F]THK-5351 was synthesized similarly to [^{18}F]THK-5317 except for semi-preparative HPLC purification (Phenomenex Luna 10µ 250x10 mm, 78/22 (v/v) acetonitrile/20 mM monobasic sodium phosphate).

Magnetic Resonance Imaging and Processing

All study participants underwent MRI scans using a 3.0 T GE SIGNA 750 scanner (GE Healthcare, UK) with an 8- or 32-channel head coil. T1-weighted anatomical data were acquired in the transverse or sagittal plane using a 3D inversion recovery fast spoiled gradient-echo sequence (TI: 450 ms; TR: 8.1 ms; TE: 3.2 ms; flip angle: 12˚; matrix: 256 x 256 x 156; voxel dimensions: 1 mm x 1 mm x 1 mm; FOV: 256 mm; slice thickness: 1.0 mm). T1-w images were aligned along the anterior and posterior commissure and were corrected from magnetic field inhomogeneity (SPM12). T1-w images were tissue-class segmented (SPM12) for GM, WM, and CSF.

PET Imaging

PET data were acquired on a Siemens ECAT EXACT HR+ tomograph in 3D mode. All PET scans began with a ^{68}Ge/^{68}Ga transmission scan, which was used for attenuation and scatter correction. *[^{11}C]PiB* Dynamic [^{11}C]PiB data were acquired for 70 minutes following a nominal 15 mCi bolus injection. PET data were reconstructed using filtered backprojection (matrix size 128x128x63, voxel dimensions 2.57x2.57x2.43 mm, 4mm in-plane Gaussian Filter, brain mode on, axial filtering off, zoom=2). The dynamic time series (5x2 min/fr, 12x5 min/fr) was interframe realigned (SPM12), denoised (HYPR-LR, 9 mm Gaussian composite smoothing (143, 144)), and summed data (0-10 minutes) were coregistered to the GM probability map (SPM12, see tissue segmentation below) to derive the spatial transformation matrix that was applied to the full dynamic time series. Cerebellar time-activity-curves (TACs) were extracted from the coregistered PET time series and used to generate parametric LGA DVR images in native PET space, which were transformed to MRI space by applying the sum PET affine transformation matrix. Subjects were then dichotomized as PiB(+) or PiB(-) based on a regional global average(145) to indicate Aβ plaque status for descriptive purposes.

THK PET Participants underwent [^{18}F]THK-5317 (n=14) or [^{18}F]THK-5351 (n=24) PET scans. A subset of 10 subjects (5 CS, 4 CD, 1 MCI, age 69±8, 53-81 years) were scanned with both THK radiotracers with an average of 321±46 days between scans due to a protocol amendment to evaluate [^{18}F]THK-5351 in humans. Following the transmission scan, dynamic 90-minute emission scan (5x2 min/fr, 16x5 min/fr) initiated with bolus injection in the antecubital vein of a nominal 185 MBq dose for [^{18}F]THK-5317 and a 185 or 370 nominal MBq dose for [^{18}F]THK-5351. PET images were reconstructed using filtered backprojection (matrix size 128x128x63, voxel dimensions 2.57x2.57x2.43 mm, 4mm in-plane Gaussian Filter, brain mode on, axial filtering off) with corrections applied for normalization, detection deadtime, attenuation and radioactive decay.

THK Image Processing and Quantification of Specific Binding Using Reference Tissue Methods

The reconstructed PET time series images were pre-smoothed with a 3 mm isotropic Gaussian kernel, realigned for inter-frame motion (SPM12), denoised (HYPR-LR-FC(144), 9 mm isotropic Gaussian composite smoothing), and coregistered to the T1-w MRI (SPM12). TACs were extracted from the coregistered dynamic PET data for FreeSurfer defined ROIs (see below). Cerebellar GM was used as a reference region of non-displaceable binding based on the lack of NFT pathology observed in the cerebellum in neuropathology studies(146), and previous *in vitro* validation studies of THK-5117 and T807 (60, 132). DVR estimates were calculated by applying LGA(124), MRTM2(129), and the basis function implementation of SRTM(127). For LGA and MRTM2, the parameter stability time (t*) was evaluated by comparison of within method differences using t*=10, 20, 30, 40, 50, and 60 minutes. The LGA was implemented with k_2 fixed to the average of MRTM2 and SRTM k_2' estimates, and with the k_2 term removed. SRTM was implemented by generating 200 basis functions using θ_3=0.001-0.2 min^{-1} in .001 min^{-1} increments. Stability of DVR estimates for shorter scan durations was assessed by truncating the THK PET time series to 50, 60, and 70 minutes and comparing within-method differences with DVR estimates derived from the full 90-minute dataset. In addition to dynamic methods, 20-minute scan windows starting 10 to 70 minutes post-injection were investigated in stepwise 10 minute intervals to assess the stability of SUVR. Parametric DVR and SUVR images were generated for visual comparison of THK-5351 and THK-5317.

Region of Interest Delineation.

ROI segmentation of the MRI was performed using FreeSurfer 5.3 (http://surfer.nmr.mgh.harvard.edu/). FreeSurfer defined cerebellar GM and cerebral WM masks were eroded to limit spillover from adjacent regions. This was accomplished by smoothing binary FreeSurfer ROIs with an isotropic 8 mm Gaussian kernel (to simulate PET resolution) and removing voxels <0.6 for GM and <0.95 for cerebral WM (thresholds selected based on apparent spillover of summed PET images). Examples of some of the ROIs used for this analysis are shown in Appendix D.

Comparison of [^{18}F]THK-53517 and [^{18}F]THK-5351 Binding Estimates

Nine a priori regions were selected for analysis based on previously reported regions affected by NFT tau in AD (15, 82, 87, 112, 136). Regions included the entorhinal cortex, hippocampus, fusiform gyrus, inferior, middle and superior temporal gyrus, inferior parietal cortex and the peristriate region of the occipital cortex. With the exception of WM and cerebellar GM, ROIs were split unilaterally. Within and between method differences in DVR (or SUVR) were assessed using a Bland-Altman(147, 148) approach and by calculating the mean and standard deviation of DVR differences across all subjects and analyzed ROIs.

Bland-Altman plots, as opposed to regression and correlation analyses, have an advantage in the context of DVR and SUVR comparison since effects related to the magnitude of binding and noise can be more easily identified (see Appendix C).

3.3.3 Results

Comparison of THK-5317 and THK-5351 In Vivo Kinetics

Summary statistics for the radiosyntheses of [^{18}F]THK-5317 and [^{18}F]THK-5351 are presented in Table 3.3. Figure 3.3 compares the dynamic SUV and target-to-cerebellar GM ratios averaged across the 10 subjects that received both ^{18}F-THK-5351 and ^{18}F-THK-5317 PET scans. SUV was lower for THK-5351 in all regions. THK-5351 had slightly faster clearance after bolus passage for cerebellar GM and faster clearance for cortical WM. WM-to-cerebellum ratios were higher for THK-5351 from 0-30 minutes and peaked at 45-50 minutes, after which ratios declined. Whereas for THK-5317, WM-to-cerebellum ratios were greater than those for THK-5351 after 35 minutes and increased throughout the entire scan. Target-

Metric	[^{18}F]THK-5317 (n=14)	[^{18}F]THK-5351 (n=24)
EOS Yield* [MBq]	2627 ± 888	3737 ± 1147
Molar Activity* [MBq / μmol]	318 ± 85	233 ± 70
Injected Dose* [MBq]	200 ± 4	340 ± 89
Injected Mass* [nmol]	0.98 ± 0.43	2.26 ± 0.75

Table 3.3 [^{18}F]THK-5317 and [^{18}F]THK-5351 Radiochemical Synthesis Summary Statistics. (indicates $p<0.01$)*

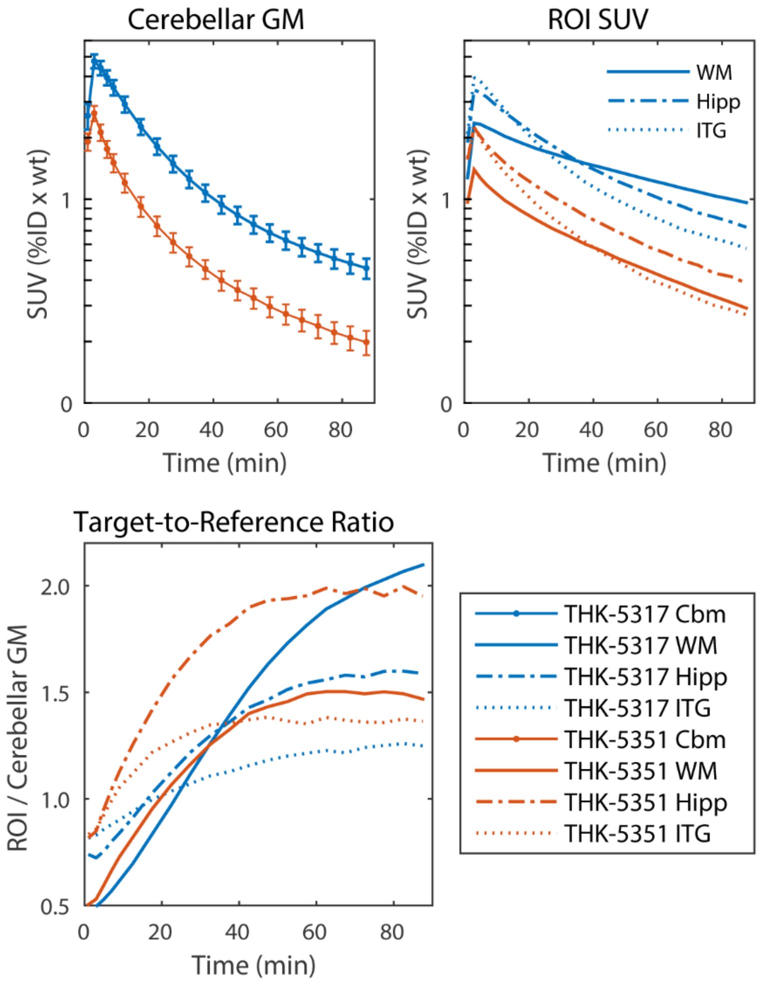

Figure 3.3 Average [^{18}F]THK-5317 and [^{18}F]THK-5351 TACs

to-cerebellum ratios for high binding regions associated with NFT tau were observed to plateau later than regions with low/negligible binding for both tracers.

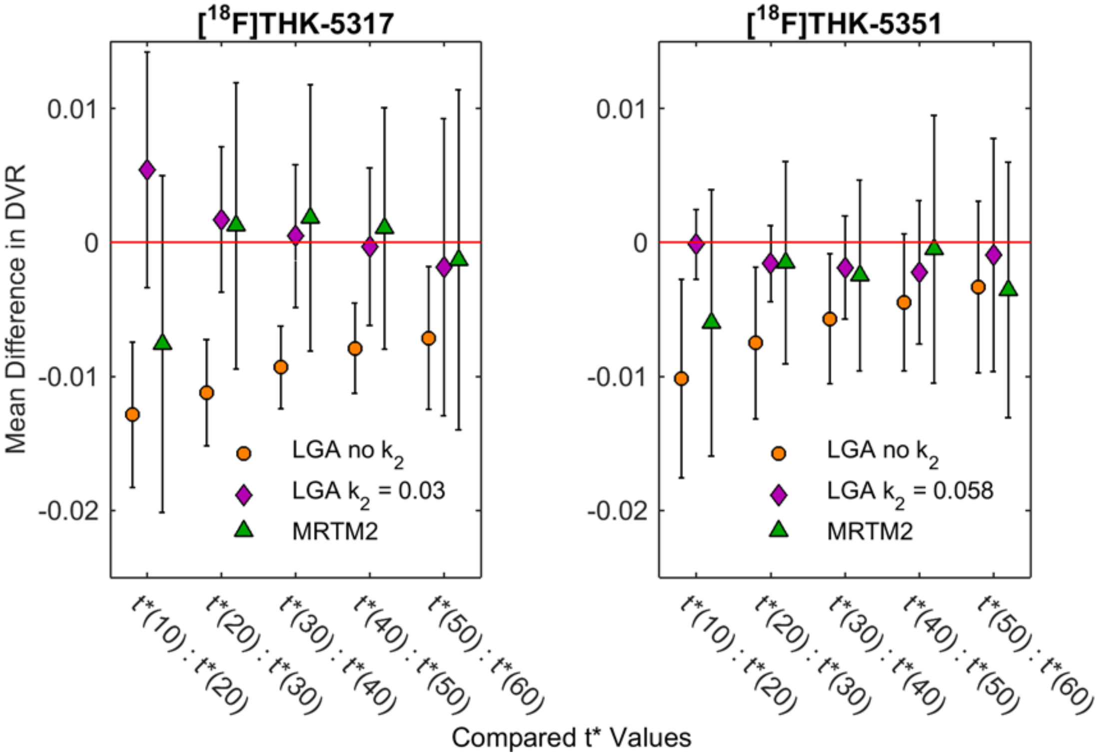

Figure 3.5 LGA and MRTM2 t Determination for THK Compounds*

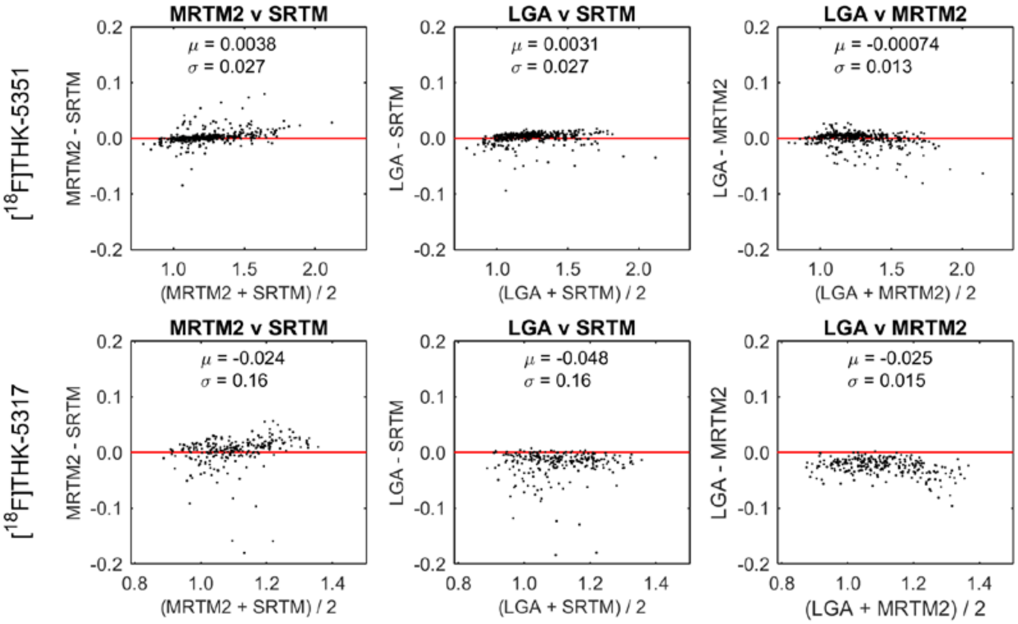

Figure 3.4 Comparisons of DVR Methods for Quantification of THK Compounds

Comparison of Reference Tissue DVR Methods

MRTM2 DVR estimates were stable for t*≥20 minutes, although the within method variability was lowest for t*=30 and 40 minutes (Figure 3.5). Within method comparisons of LGA DVRs indicated later stability (t*=40 min) with DVRs derived from t*<40 minutes showing an underestimation associated with the level of binding. LGA DVR estimates were also sensitive to combinations of $\overline{k_2}$ and t*. Results were consistent for both THK-5351 and THK-5317. Since the $\overline{k_2}$ term introduced more noise for DVR estimates and there was minimal improvement in DVR stability for earlier t*, LGA was implemented without the $\overline{k_2}$ term for further comparisons.

Figure 3.4 shows the between-method comparison of DVR estimates for LGA (t*=40 min, no $\overline{k_2}$

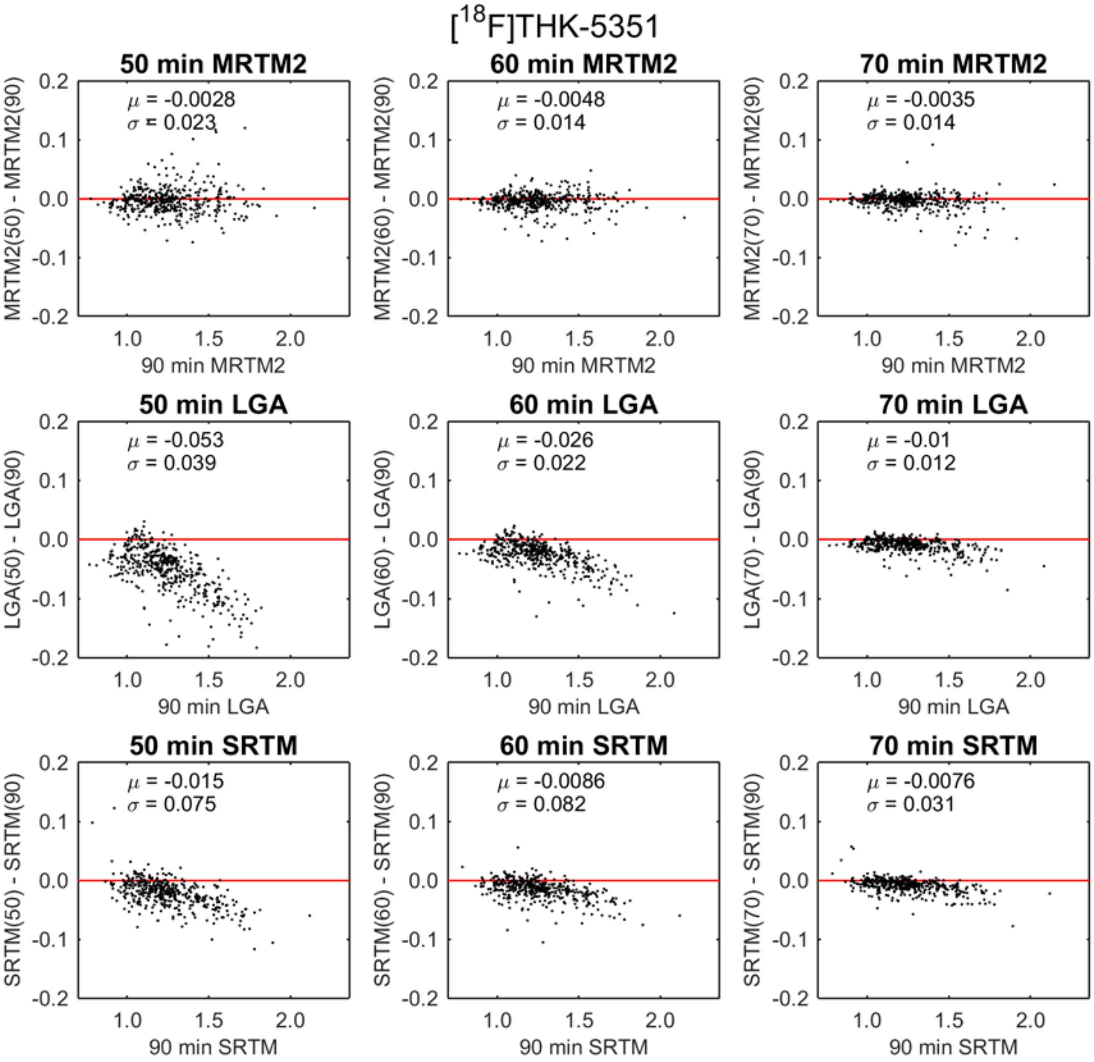

Figure 3.6 [^{18}F]THK-5351 DVR Stability with Shortened Scans

term), MRTM2 (t*=30 min) and SRTM. For THK-5351, minimal differences were observed overall between methods indicated by low mean difference and standard deviation over the range of DVRs. However, for THK-5317 there was less agreement between methods, with LGA underestimating both SRTM and MRTM2. Further, MRTM2 yielded higher values for regions with elevated DVR (> 1.2) compared to LGA and SRTM, although MRTM2 and SRTM estimates were otherwise similar. Overall, between-method variability was higher for THK-5317 compared to THK-5351.

Results comparing the effects of scan duration on MRTM2, LGA and SRTM [^{18}F]THK-5351 DVR estimates are shown in Figure 3.6 and Figure 3.7 for [^{18}F]THK-5317. MRTM2 estimates using shortened scans were similar to 90-minute MRTM2 DVR estimates and did not indicate any trends with increasing

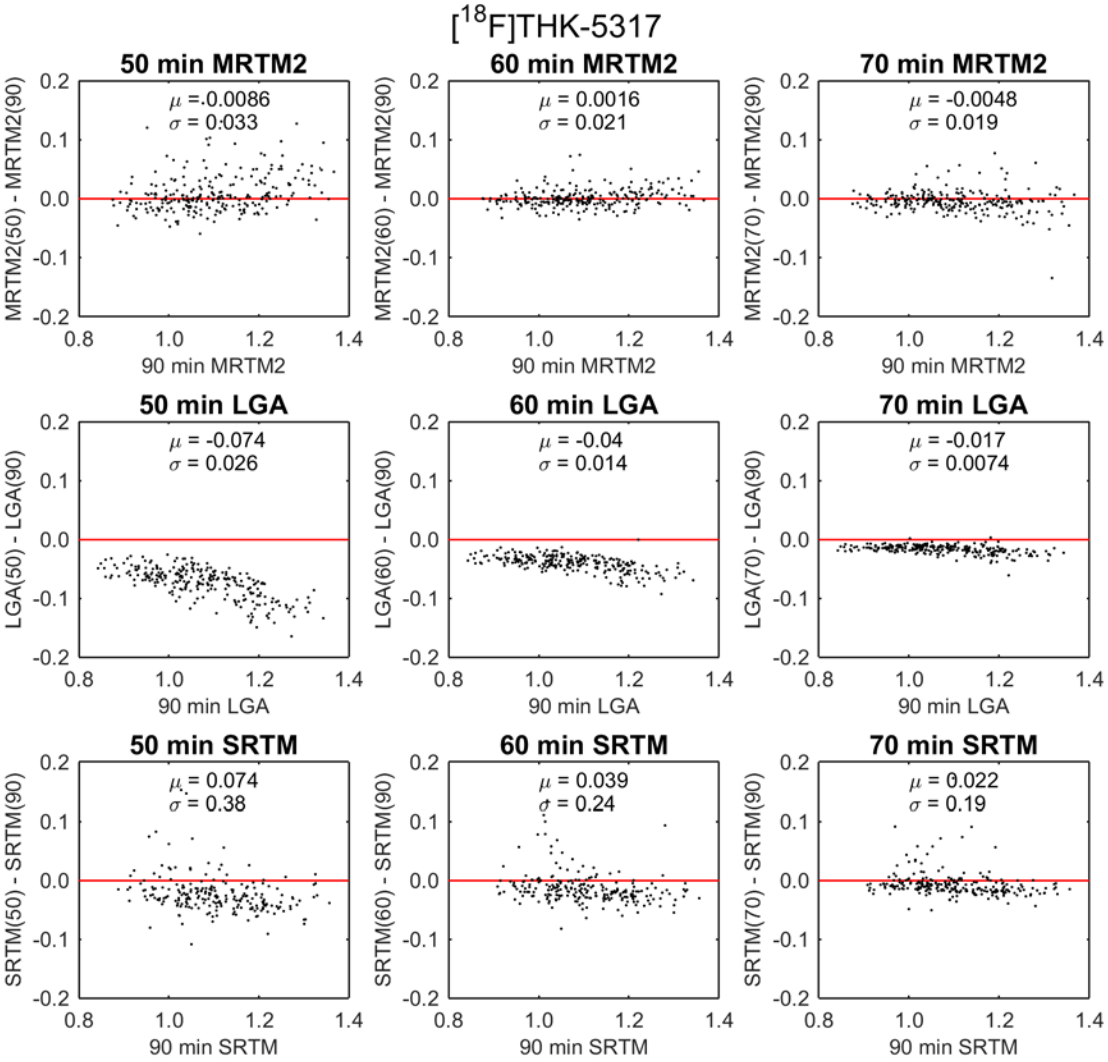

Figure 3.7 [^{18}F]THK-5317 DVR Stability with Shortened Scans

DVR, although 50-minute scans resulted in noticeably higher variability. LGA estimates underestimated DVR for shorter scan durations (≤60 minutes), especially at higher DVR values. This underestimation in DVR was still apparent in 70-minute scans, but was reduced compared to shorter scans. Effects of shortening the PET scan duration for SRTM were similar to LGA, but did not show as much of a binding dependent underestimation in DVR.

Temporal Stability of SUVR

SUVR estimates were temporally stable 50-70 minutes post-injection (Figure 3.8). SUVRs were lower in higher binding regions for windows before 50-70 minutes. For [18F]THK-5317, a negative global difference was observed for SUVR taken from 50-70 minutes when compared to 60-80 minute SUVR estimates, but binding dependent differences were minimal(Figure 3.9). SUVRs for windows earlier than 50-70 minutes exhibited underestimation in higher binding regions. Regression of

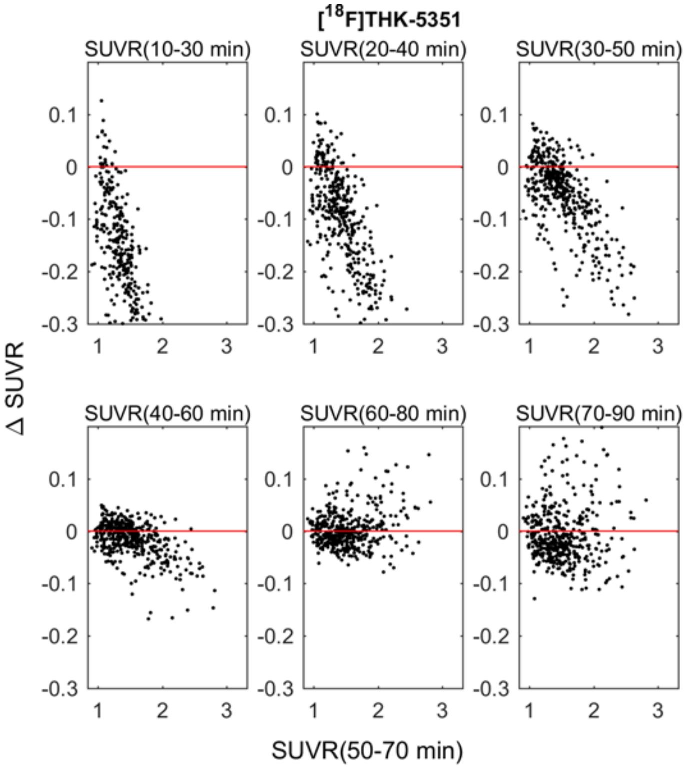

Figure 3.8 [^{18}F]THK-5351 SUVR Temporal Stability

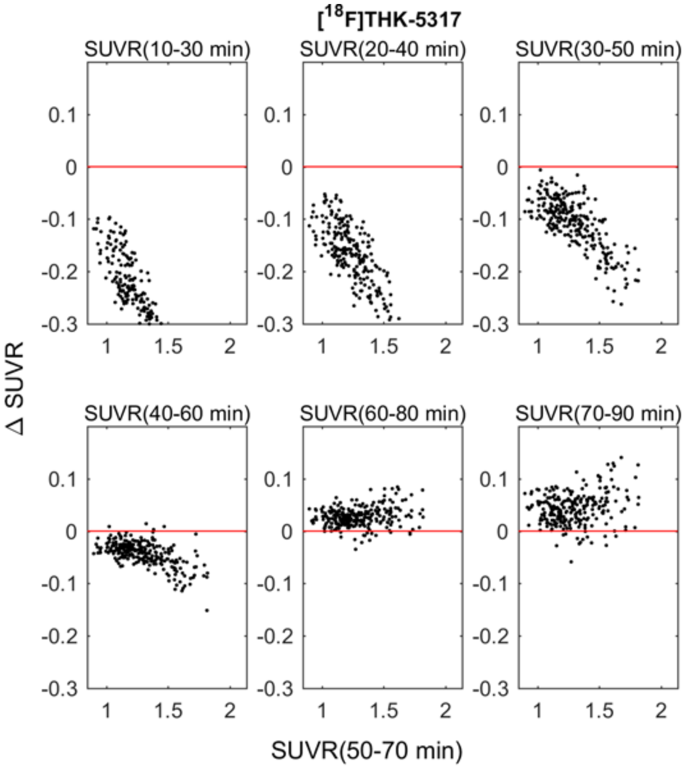

Figure 3.9 [^{18}F]THK-5317 SUVR Temporal Stability

SUVR on DVR indicated minimal changes in regression parameters for 20-minute windows starting 50 minutes post-injection or later (Figure 3.10).

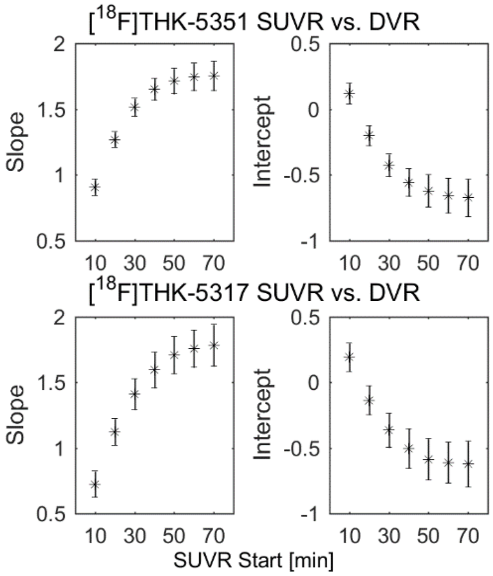

Figure 3.10 SUVR vs DVR Regression Parameters for THK Compounds

Comparison of Parametric DVR and SUVR Images

LGA and MRTM2 produced similar parametric DVR images for [^{18}F]THK-5351 (Figure 3.11). However, MRTM2 parametric images had considerably higher DVR values in WM for [^{18}F]THK-5317. Compared to DVR images, SUVR images (50-70 minutes) had higher WM signal relative to GM, although for [^{18}F]THK-5317, MRTM2 had greater sensitivity for WM.

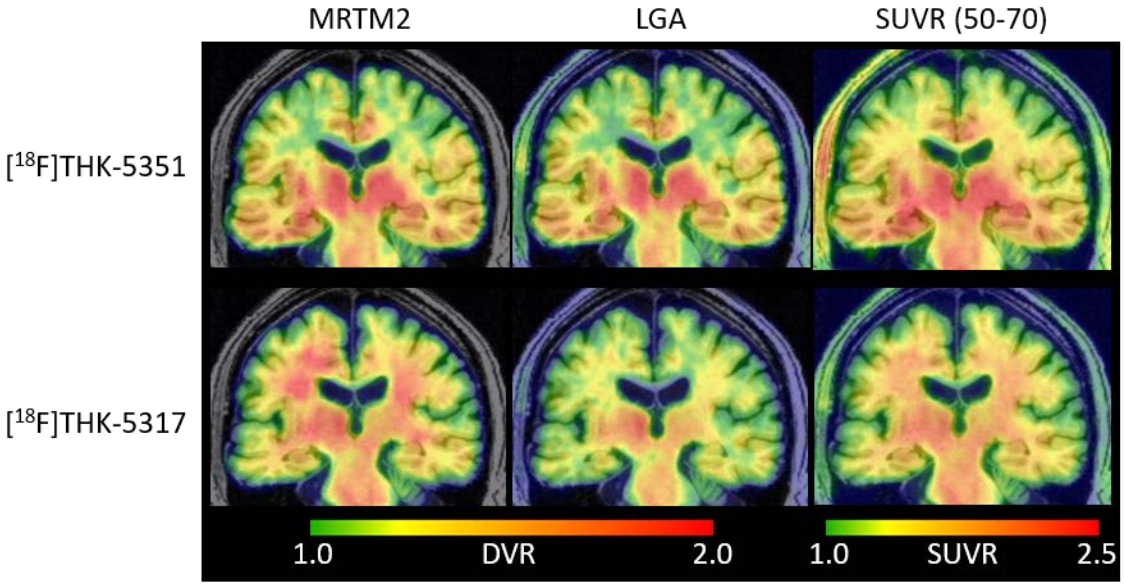

Figure 3.11 Parametric Image Comparison for THK Compounds

Comparison of [^{18}F]THK-5317 and [^{18}F]THK-5351 DVR Estimates

General agreement was observed between [^{18}F]THK-5317 and [^{18}F]THK-5351 in regions associated with tau pathology (Figure 3.12 and Table 3.4), with the exception of SRTM which failed to converge in some ROIs for [^{18}F]THK-5317. [^{18}F]THK-5351 DVR estimates were higher in GM, and lower in

WM compared to [^{18}F]THK-5317. Adjusting for the time between [^{18}F]THK-5351 and [^{18}F]THK-5317 scans did not change regression parameters.

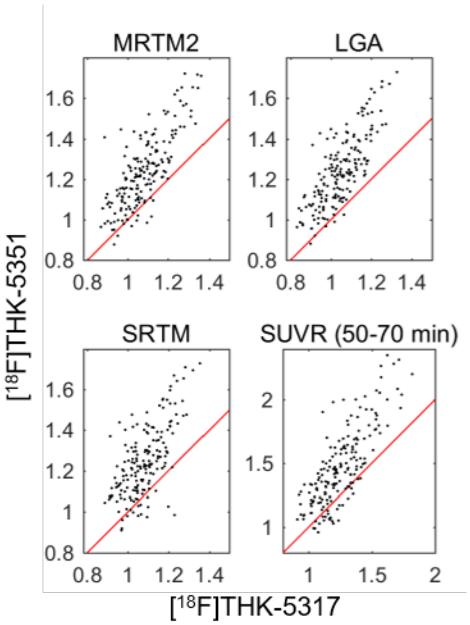

Figure 3.12 Comparison of [^{18}F]THK-5351 and [^{18}F]THK-5317 Binding Estimates

3.3.4 Discussion

The most apparent differences between the THK tracers pertained to whole brain uptake (blood-brain barrier penetrance), specific GM binding, and non-specific WM binding. A global reduction in SUV was observed for [^{18}F]THK-5351 compared to [^{18}F]THK-5317 indicating reduced brain penetrance, which is consistent with the differences in lipophilicity of the THK compounds ($logP_{5351}$ = 1.5, $logP_{5317}$ = 2.32)(94). WM clearance was faster for [^{18}F]THK-5351, in agreement with previously reported results showing slow *in vivo* WM clearance for [^{18}F]THK-5317(135) and faster *in vitro* WM dissociation for THK-5351(94). Higher DVR values for [^{18}F]THK-5351 in regions associated with tau pathology is potentially attributed to a higher ligand-receptor affinity observed with THK-5351 in AD hippocampal homogenates(94, 95, 123). The difference in binding estimates was not likely due to the systematic delay between [^{18}F]THK-5351 and [^{18}F]THK-5317 scans ([^{18}F]THK-5351 always occurred after [^{18}F]THK-5317) since regression parameters comparing within method binding estimates were not changed when covarying for this interval, and the average increase in [^{18}F]THK-5351 GM signal was more than 3-fold higher than the highest annual rate of change reported in a longitudinal study [^{18}F]THK-5117 study(136). Additionally, differences in injection protocols (injected mass and radioactivity) could also have been a confound for comparisons, but this is unlikely based on the apparent K_D of the THK compounds

Method	Coefficient	β (SE)	95% CI	R^2
MRTM2	Slope	1.28 (0.08)	1.12, 1.43	0.61
	Intercept	0.01 (0.00)	-0.30, 0.03	
LGA	Slope	1.34 (0.08)	1.19, 1.50	0.63
	Intercept	-0.15 (0.08)	0.32, 0.00	
SRTM	Slope	0.70 (0.77)	-0.82, 2.21	0.00
	Intercept	0.01 (0.02)	-0.03, 0.06	
SUVR (50-70 min)	Slope	1.31 (0.07)	1.16, 1.45	0.63
	Intercept	-0.17 (0.09)	-0.35, 0.02	

Table 3.4 Regression Summary of [^{18}F]THK-5351 on [^{18}F]THK-5317

Accurate and reliable specific binding quantification is needed for PET neuroimaging studies investigating cross-sectional and longitudinal pathological differences. [^{18}F]THK-5351 DVR estimates were generally comparable between methods when using the entire 90-minute dynamic PET series, suggesting DVR methods provide reliable quantification. However, within method variability was higher for [^{18}F]THK-5317 in GM and large differences were observed in WM between DVR methods. While WM does not represent a target region for NFT pathology in AD, WM spill in was likely a contributing factor of additional variability between methods and between tracers when comparing GM regions, but this was not formally investigated.

In addition to quantitative accuracy, the PET scan duration needs to be minimized for large-scale studies to accommodate higher scan volume and improve comfort of aging and cognitively impaired individuals. The MRTM2 method was least sensitive to bias and variability when using shorter scan durations for THK compounds and indicated minimal variability for 60- or 70-minute scans when compared to 90-minute scans. These comparisons suggest that 60-minute scans using the MRTM2 method will be sufficient for accurate binding quantification, but this may need to be reevaluated for AD persons with extensive NFT pathology (i.e. higher THK specific binding). SUVR has also been proposed to reduce scan duration with several different timing windows suggested in the THK literature (87, 135-137). Within-method comparisons of stepwise SUVR estimates and comparisons with DVR estimates in this work suggest that SUVRs are stable for 20-minute scans starting 50 minutes post-injection and are changing rapidly for earlier time points. Fifty to 70 minute SUVR overestimates DVR by a factor of nearly two. Despite having a more one-to-one relationship with DVR at earlier time points, the rapid changes in SUVR occurring prior to 50 minutes post-injection would result in considerable parameter bias dependent on small differences in the uptake period, which would introduce more variability into SUVR measures. Windows later than 50-70 minutes are also disadvantageous, especially for [^{18}F]THK-5317, due to increasing contribution of non-specific WM signal at later time points. The balance between scan duration and quantification should be considered in the context of study, wherein DVR methods provide lower within-method variability compared to SUVR, and are better suited for detecting small changes in longitudinal studies.

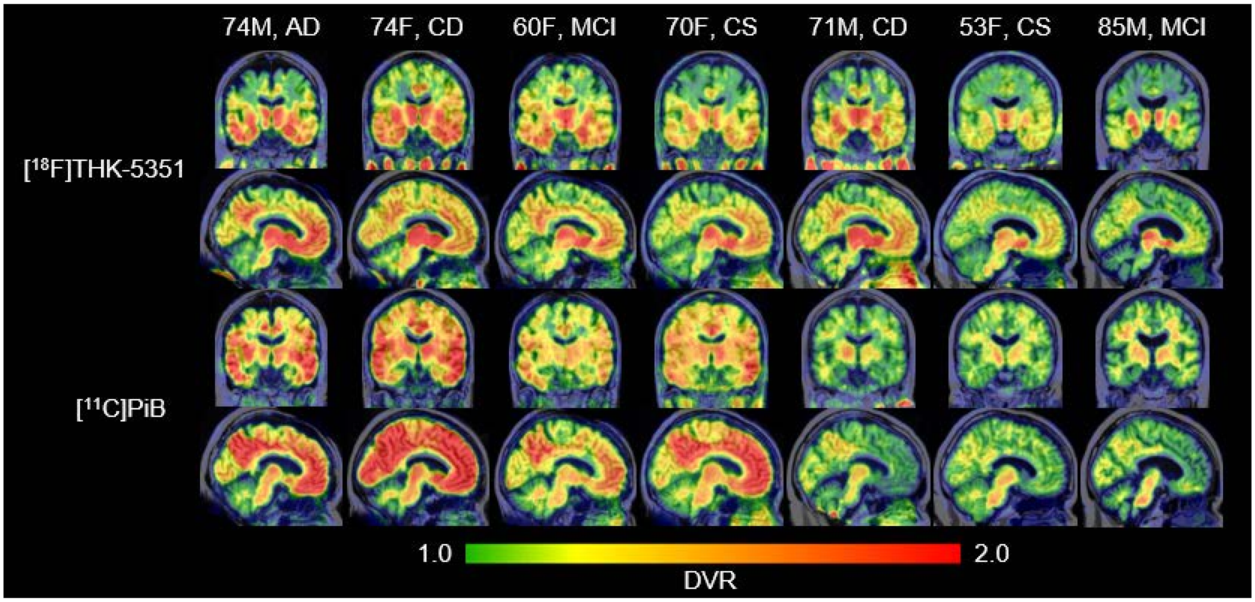

Figure 3.13 [^{18}F]THK-5351 and [^{11}C]PiB Parametric Images

While the primary goal of this study was to evaluate quantification methods and compare *in vivo* THK radiotracer pharmacokinetic properties, it is also important to discuss the spatial binding characteristics in the context of AD NFT neuroimaging. When excluding the basal ganglia and hippocampus, the spatial extent and magnitude of THK binding corresponded to hierarchical spatial patterns observed in neuropathological staging of NFTs, particularly for PiB(+) individuals (Figure 3.13). These patterns were more evident with [^{18}F]THK-5351 than with [^{18}F]THK-5317. When comparing the two THK compounds, [^{18}F]THK-5351 has less non-specific WM binding, faster pharmacokinetic properties, and a higher dynamic range suggesting [^{18}F]THK-5351 it is better suited for NFT imaging in AD. Discussion of target and off-target THK binding is continued in section 3.5.3 where these tracers are compared to [^{18}F]MK-6240.

3.4 In Vivo Characterization and Quantification of [^{18}F]MK-6240

3.4.1 Overview of [^{18}F]MK-6240

[^{18}F]MK-6240 was developed by Merck using a sophisticated drug optimization process with the goals of a high affinity for NFTs, high selectivity for NFTs over Aβ plaques, low nonspecific binding, including WM, and limiting results to compounds that were amendable to radiofluorination(117). Preclinical studies of [^{18}F]MK-6240 indicated high *in vitro* affinity and selectivity for NFTs over both Aβ plaques(102). In addition, *in vivo* self-blocking studies comparing [^{18}F]MK-6240 and [^{18}F]T807 in non-human primates that do not express NFT pathology showed [^{18}F]MK-6240 was not displaceable indicating [^{18}F]MK-6240 did not exhibit specific binding to non-NFT targets common to macaques and humans (e.g. MAO-A and MAO-B). In contrast, [^{18}F]AV-1451 was displaceable in macaques, which indicates specific binding to non-NFT targets(102). [^{18}F]MK-6240 also did not show high non-displaceable signal (V_T ~5 mL/ cm^3) in macaques including WM. These preclinical results provide evidence that [^{18}F]MK-6240 has potential for selective imaging of AD tau aggregates in humans, and may be more sensitive for detecting NFTs in regions associated with early NFT deposition (e.g. hippocampus) due to an absence of off-target binding near critical structures. The central aims of this section are to 1) evaluate the in vivo pharmacokinetics, 2) investigate dynamic and static reference tissue methods for quantification of specific binding, 3) characterize the in vivo spatial distribution of binding related to NFTs, and 4) identify regions of potential off-target binding of [^{18}F]MK-6240 in humans ranging from cognitively unimpaired young adults to clinically diagnosed probable AD.

3.4.2 Methods

Participants and Recruitment

Participants (n=51) were recruited from the University of Wisconsin-Madison Alzheimer’s Disease Research Center and its affiliated clinics, or the Wisconsin Registry for Alzheimer’s Prevention(141). AD dementia individuals were determined based on clinical diagnosis of probable AD that was not informed by AD biomarkers. All other participants were grouped as young controls (participants 45 years and under), older controls, cognitive decliners, and mild cognitive impairment (MCI). The latter three diagnoses were based on longitudinal neuropsychological evaluation and consensus diagnosis(141). Descriptive statistics for the groups are summarized in Table 3.5. Written informed consent was obtained from all individuals prior to participation. This study was conducted under the University of Wisconsin-Madison Institutional

Group	Mean Age, Range [yrs]	Sex	APOE-ε4 Carriers	MMSE/ MoCa	PiB(+)
Young Controls (n=3)	35 ± 9, 27-45	1F, 2M	N.A.	N.A.	N.A.
Older Controls (n=33)	67 ± 5, 56-77	20F,13M	14	29±.8	7
Cognitive Decliners (n=6)	65 ± 2, 61-68	4F, 2M	4	28±1	3
MCI (n=2)	69 ± 10	1F, 1M	2	26±2	1
Probable AD (n=7)	73 ± 3, 67-79	2F, 5M	2 (2 N.A.)	17±2	5
Total (N=51)	66 ± 10, 27-79	28F, 23M	22 (5 N.A.)		16 (3 N.A.)

Table 3.5 Descriptive Statistics for [^{18}F]MK-6240 Study Participants

Review Board and the FDA Investigational New Drug mechanism for [^{18}F]MK-6240 and [^{11}C]PiB PET studies.

MRI and Anatomical Delineation

All participants underwent a T1-weighted 3D inversion recovery fast spoiled gradient-echo sequence on a 3T MRI scanner (Signa 750, GE Healthcare) with a 32-channel head coil (inversion time, 450 ms; repetition time, 8.1 ms; echo time, 3.2 ms; flip angle, 12°; matrix, 256 × 256 × 156; voxel dimensions, 1 × 1 × 1 mm; field of view, 256 mm; slice thickness, 1.0 mm). The T1-w image was corrected for magnetic field inhomogeneity (SPM12) and tissue class segmented for white matter (WM), gray matter (GM), and cerebrospinal fluid (CSF). The deformation field obtained from the tissue-class segmentation was used to inverse warp regions of interest (ROIs) from MNI template space to native MRI space.

Radiochemical Synthesis of [^{11}C]PiB and [^{18}F]MK-6240

[^{11}C]PiB Radiochemical synthesis of [^{11}C]PiB was performed as described in Section 3.3.2 yielding specific activity of 650±161 MBq/nmol (mean ± standard deviation, n=48) for this study sample. [^{18}F]MK-6240 was synthesized as described in Chapter 2. [^{18}F]MK-6240 radiochemical syntheses and injections are summarized in Table 3.6.

Metric (N=51)	Mean ± SD
Specific Activity [MBq / nmol]	852 ± 375
NDC Yield [%]	12.5 ± 4.0
Synthesis Time [min]	101 ± 13
Injected Activity [MBq]	393 ± 7
Injected Mass [nmol]	0.69 ± 0.28

Table 3.6 [^{18}F]MK-6240 Radiosynthesis and Injection Summary Statistics

PET Imaging

PET scans were acquired using a Siemens ECAT EXACT HR+ tomograph. *[^{11}C]PiB* Dynamic [^{11}C]PiB scans were acquired from 0-70 minutes after a nominal 555 MBq injection for all participants except young controls, who were assumed to be devoid of Aβ pathology based on their age(17). DVRs (LGA, cerebellar GM reference region) were estimated(73) and a global DVR threshold(145) was used to ascertain PiB status (PiB(+) or PiB(-)) for descriptive purposes. *[^{18}F]MK-6240* A total of 51 participants underwent [^{18}F]MK-6240 PET scans following a nominal 370 MBq injection. A subset of nineteen participants (3 young controls, 6 older controls, 2 cognitive decliners, 1 MCI, 7 probable AD) were scanned dynamically from bolus tracer injection for a total duration of either 90, 105, or 120 minutes. The remaining 32 participants were scanned for 60 minutes following a 60-minute uptake period. [^{18}F]MK-6240 PET images were reconstructed using optimized subset expectation maximization (ECAT v7.2.2, 4 iterations, 16 subsets, brain mode on, ramp filter, voxel size 2.57x2.57x2.425 mm, matrix size 128x128x63, corrections applied: segmented attenuation, detector deadtime, scatter, detector normalization and radioisotope decay).

Data Extraction, Quantification and Analysis of Simplified Methods

The reconstructed [^{18}F]MK-6240 PET time series was interframe realigned, and coregistered to T1-w MRI (SPM12). HYPR-LR denoising(144) was applied in native PET space after interframe realignment for PET scans with full dynamic data used for DVR analysis (see below). Parametric [^{18}F]MK-6240 standard uptake value ratio ($SUVR = C(t) / C_{ref}(t)$) images were generated using data from 70-90 minutes post injection (inferior cerebellar GM reference region). [^{18}F]MK-6240 time-activity curves (TACs) were extracted from the coregistered PET time series in native T1 space. Pons and off-target ROIs were delineated in MNI space based on an in-depth imaging review of [^{18}F]MK-6240 parametric SUVR images in individual cases and SUVR images averaged across control subjects (see below). Additionally, an inferior cerebellum ROI was generated for reference region analysis by combining Automated Anatomical Labeling (AAL, Neurodegenerative Diseases Institute, Université de Bordeaux) ROIs (93, 94, 101-104) in native T1 space and eroding the mask to limit spill-in from adjacent WM, CSF. The inferior cerebellum (henceforth referred to as “cerebellum”) was used, as opposed to the entire cerebellar GM, due to focal binding observed in the superior cerebellum and to avoid contamination from occipital spillover observed in AD participants with high occipital retention. Brain penetrance and evaluation of reference regions (cerebellum and pons) was performed by comparing SUVs across all subjects. DVRs were determined at the ROI level using reference tissue LGA(124) and MRTM2(129) for all participants with full dynamic acquisitions (n=19). LGA and MRTM2 parameter stability times (t*) were determined by comparing DVR estimates using stepwise t* values (see Appendix C). Stability of the DVR as a function of scan duration was evaluated within each method by regressing DVR estimates derived from truncated data (i.e. shorter scans) onto DVRs derived from full-length scans. SUVRs derived from stepwise 20-minute windows starting 40 minutes post-injection were regressed onto LGA and MRTM2 DVR to assess the quantitative accuracy of SUVR.

Regions of Interest

ROIs consisted of the AAL atlas, which was restricted to voxels with GM probabilities greater than thirty percent, and manually segmented ROIs drawn in MNI space in regions with apparent off-target binding. Regions for regression analyses included all AAL ROIs (n=90) except cerebellar regions and also did not include the manually segmented off-target ROIs. This was done to capture the full range of binding observed in this study throughout the entire brain and a lack of off-target binding observed in the brain for PiB(-) controls. Examples of some of the modified AAL ROIs are provided in Appendix D.

[^{18}F]MK-6240 Image Review

Individual parametric [^{18}F]MK-6240 SUVR images were reviewed to identify regions of potential off-target binding (not consistent with neuropathology literature) and on-target tau binding (consistent with neuropathology literature) by a neuroradiologist (Rowley) and experienced neuroimagers blinded to amyloid imaging, cognitive trajectory and clinical group. Additionally, [^{18}F]MK-6240 parametric images normalized to MNI space were averaged for PiB(-) controls and PiB(+) AD and MCI cases to aid in the identification of common off-target binding regions and off-target ROI delineation.

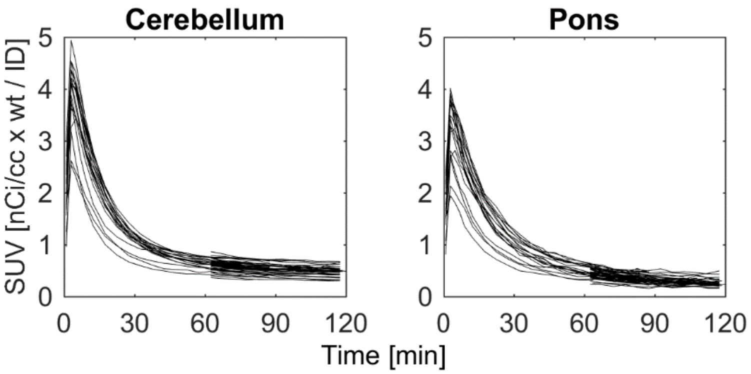

Figure 3.14 [^{18}F]MK-6240 SUV TACs

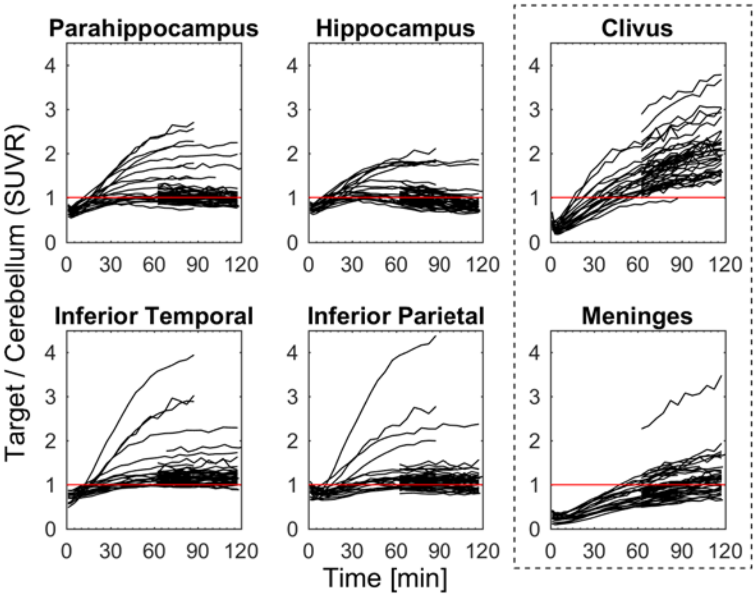

Figure 3.15 [^{18}F]MK-6240 SUVR TACs in Target and Off-Target Regions

3.4.3 Results

Reference Region Evaluation

SUV TACs indicated consistent washout across all 51 subjects in the cerebellum and the pons (Figure 3.14), and brain penetrance similar to other PET radioligands (peak SUV ~ 2.5-5). The cerebellum was used as reference region for the remainder of the analyses due to the larger volume ROI volume (17.1±3.8 cm^3 vs. 2.2±0.4 cm^3) and previous validation with other tau PET radioligands(60, 132).

Pharmacokinetic Evaluation of [^{18}F]MK-6240

Target-to-cerebellum TACs (Figure 3.15) became stable around 70 minutes post injection for moderate binding subjects and regions, but were still increasing at 90 minutes in neocortical regions of the highest binding AD subjects (SUVR > 3). TACs relative to cerebellum in off-target regions that included bone marrow (ethmoid sinus, clivus, sphenotemporal buttress) were increasing throughout the entire 120-minute scan duration (figure 2) and had SUVR values similar to the parahippocampus and the inferior temporal gyrus of PiB(+) AD and MCI individuals around 90 minutes. Similarly, TACs in the meninges relative to cerebellum were increasing throughout the entire 120 minute scan and varied considerably in magnitude across subjects (SUVR range 0.5 to 3.5 at 120 minutes).

Quantification of [^{18}F]MK-6240 Specific Binding

The initial fitting times for LGA ($k_2 = 0.04$ min^{-1}, based on median MRTM2 and SRTM2 estimates) and MRTM2 were 35 and 30 minutes, respectively. Regression (Table 3.7) of MRTM2 onto LGA DVR using the full dynamic scan duration was near unity with LGA slightly underestimating MRTM2 DVR (Figure 3.16). This is potentially due to the noise-dependent bias inherent in LGA graphical analysis(149).

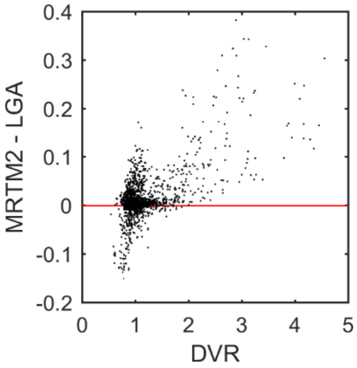

Figure 3.16 [^{18}F]MK-6240 DVR Method Comparison

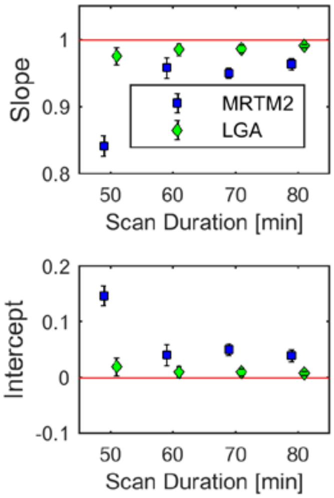

Figure 3.17 [^{18}F]MK-6240 DVR Stability with Shortened Scans

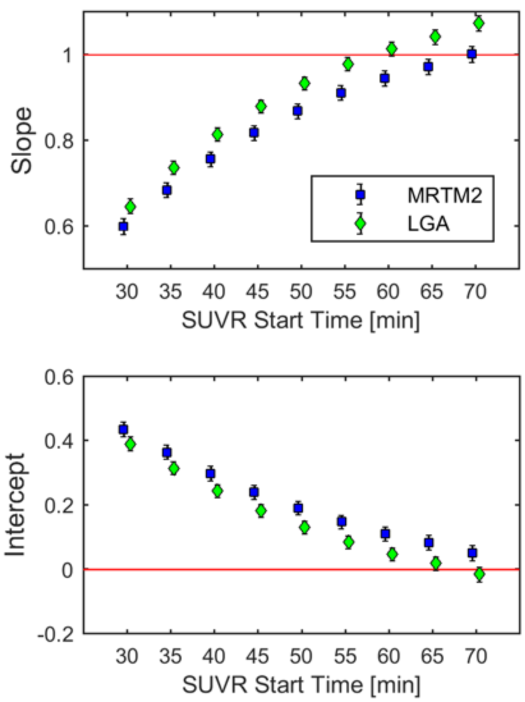

Figure 3.18 [^{18}F]MK-6240 Regression of SUVR vs. DVR

Regression outcomes were similar when removing regions with DVR values less than 1.3 from the regression analysis. When shortening the dynamic scan duration, DVR estimates remained stable down to 60 minutes for LGA and 70 minutes for MRTM2 with lower intra-method variability for LGA as compared to MRTM2 for the same scan durations (Figure 3.17).

Regression of SUVR onto DVR for 20-minute scans beginning 60 or 70 minutes post-injection (Figure 3.18) indicated regression outcomes near unity (Table 3.7) with SUVR underestimating DVR (LGA and MRTM2) for 20-minute windows starting earlier than 60 minutes. Plots of SUVR onto DVR appeared bi-linear, with values around 1.0 having a different slope than values above ~1.5 DVR. Fitting parameters closest to unity between SUVR and MRTM2 were chosen as the criteria for the timing window (70-90 min) used for parametric SUVR image generation since the LGA method is known to exhibit a negative bias.

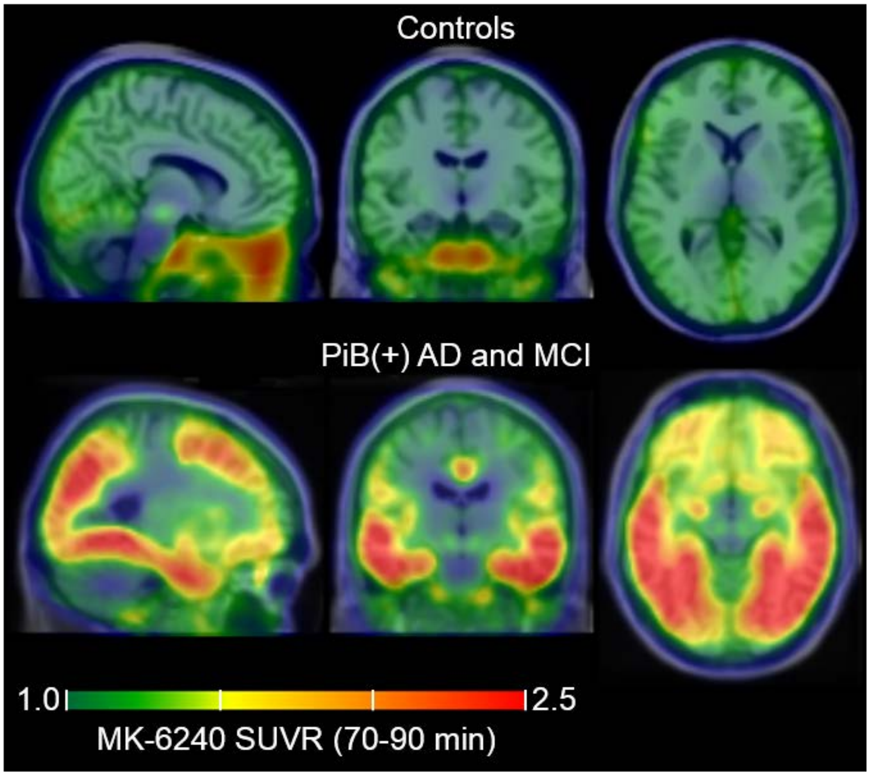

Figure 3.19 Mean [^{18}F]MK-6240 SUVR Images

[^{18}F]MK-6240 Imaging Features

Regions of potential off-target binding identified using mean

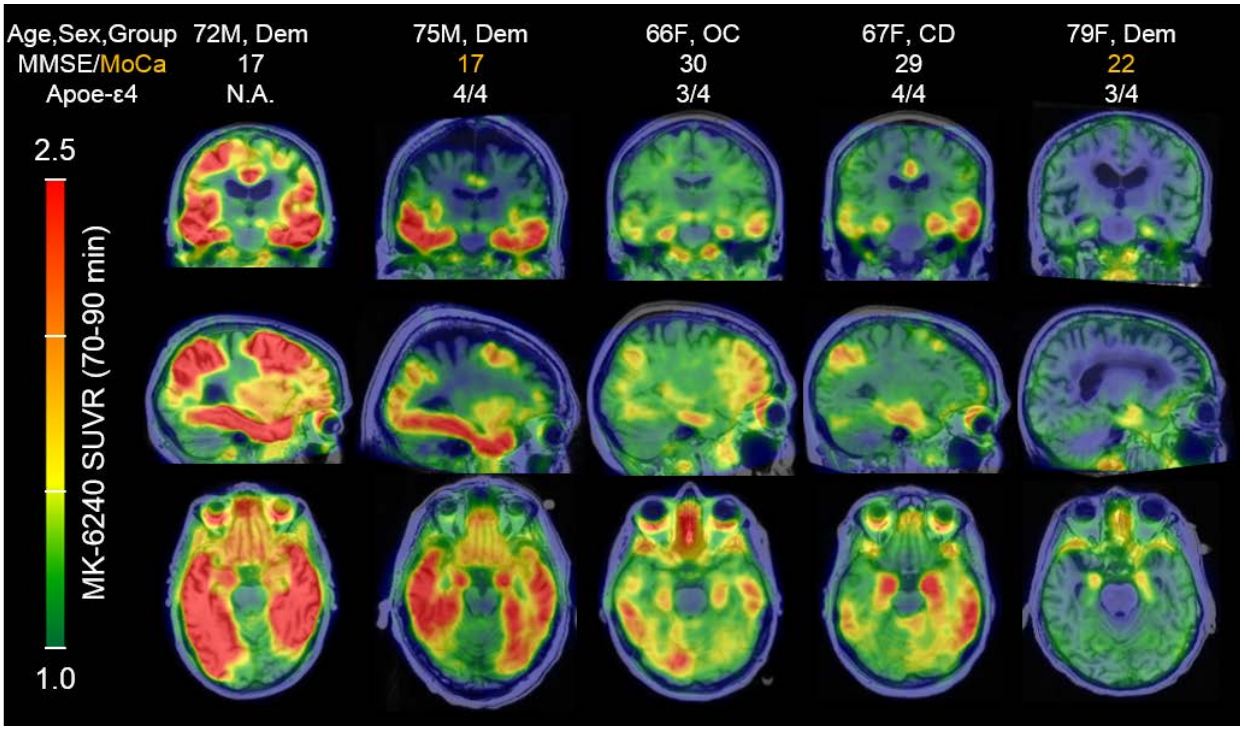

Figure 3.20 [^{18}F]MK-6240 in PiB(+) Individuals

SUVR images of controls and individual cases included the ethmoid sinus, clivus, sphenotemporal buttress, pineal gland, substantia nigra, superior anterior vermis, superior cerebellum, and the meninges and varied in magnitude and spatial extent across all subjects (Figure 3.19). In some extreme cases (6 of 51), meninges binding was observed to spill into adjacent cortical areas. In two cases, focal binding was observed in benign calvarial lesions. Elevated binding was generally not observed in the basal ganglia, choroid plexus (except 1 moderate case), or other regions of the brain that appeared to preclude binding quantification in NFT associated regions. All individuals that were PiB(+) and indicated visually elevated binding in pathological tau-associated regions followed patterns consistent with neuropathological NFT staging (Figure 3.20).

3.4.4 Discussion

PET radiopharmaceuticals for detecting NFTs in AD require 1) a high selectivity over other amyloids (e.g. Aβ), 2) high *in vivo* affinity to NFTs to improve sensitivity for detecting early and longitudinal changes, 3) low off-target binding near regions of interest, and 4) pharmacokinetic properties that enable timely PET acquisition. The kinetics properties of [^{18}F]MK-6240 were favorable for PET imaging and comparable to [^{18}F]T807(150). [^{18}F]MK6240 DVR values in AD participants were high (DVR>4) suggesting a combination of high *in vivo* affinity to NFTs and low non-displaceable signal. Compared to first generation tau ligands(82, 138), MK-6240 does not appear to have any substantial binding in regions of the brain that would preclude detection of NFTs (e.g. basal ganglia, choroid plexus), particularly in medial temporal regions (e.g. entorhinal cortex and the hippocampus) where tau pathology is implicated relatively early in the disease process(22). In addition, among the subset that were identified as being amyloid positive, MK-6240 binding patterns recapitulated neuropathological staging of NFTs including Braak I and II regions, which supports the sensitivity of the ligand to detect and characterize tau aggregates during early-stage disease. Notably, the lack of off-target binding near the hippocampus (e.g. choroid plexus), a region associated with learning and memory, may allow [^{18}F]MK-6240 to differentiate relationships between tau and other features of AD (beta amyloid, atrophy, glucose metabolism, etc.) and their impact on declining cognition. It is also noteworthy that only one of 35 PiB(-) individuals displayed elevated [^{18}F]MK-6240 binding in the brain, which was asymmetric and was not regionally concordant with neuropathological NFT staging.

Regression	Coefficient	B (SE)	95% CI	R^2
MRTM2 vs. LGA DVR	Slope	1.066 (0.002)	1.062,1.069	0.995
	Intercept	-0.060 (0.002)	-0.064,-0.055	
LGA DVR (50 min vs. full)	Slope	0.976 (0.003)	0.970, 0.983	0.981
	Intercept	0.019 (0.004)	0.012, 0.028	
LGA DVR (60 min vs. full)	Slope	0.986 (0.002)	0.982, 0.990	0.992
	Intercept	0.010 (0.003)	0.005, 0.016	
LGA DVR (70 min vs. full)	Slope	0.987 (0.001)	0.984, 0.989	0.997
	Intercept	0.010 (0.002)	0.007, 0.013	
LGA DVR (80 min vs. full)	Slope	0.991 (0.001)	0.990, 0.992	0.999
	Intercept	0.008 (0.001)	0.007, 0.010	
MRTM2 DVR (50 min vs. full)	Slope	0.841 (0.004)	0.834, 0.848	0.966
	Intercept	0.147 (0.005)	0.138, 0.157	
MRTM2 DVR (60 min vs. full)	Slope	0.958 (0.004)	0.951, 0.966	0.974
	Intercept	0.040 (0.005)	0.031, 0.050	
MRTM2 DVR (70 min vs. full)	Slope	0.951 (0.002)	0.947, 0.955	0.993
	Intercept	0.051 (0.002)	0.046, 0.056	
MRTM2 DVR (80 min vs. full)	Slope	0.964 (0.002)	0.959, 0.968	0.991
	Intercept	0.040 (0.003)	0.034, 0.045	
SUVR 40-60 vs. LGA full	Slope	0.814 (0.004)	0.806, 0.822	0.96
	Intercept	0.245 (0.005)	0.235, 0.255	
SUVR 50-70 vs. LGA full	Slope	0.934 (0.004)	0.926, 0.941	0.971
	Intercept	0.131 (0.005)	0.122, 0.141	
SUVR 60-80 vs. LGA full	Slope	1.014 (0.004)	1.006, 1.022	0.972
	Intercept	0.048 (0.005)	0.038, 0.058	
SUVR 70-90 vs. LGA full	Slope	1.073 (0.005)	1.064, 1.082	0.970
	Intercept	-0.015 (0.006)	-0.026, -0.004	
SUVR 40-60 vs. MRTM2 full	Slope	0.757 (0.004)	0.748, 0.766	0.947
	Intercept	0.299 (0.006)	0.288, 0.310	
SUVR 50-70 vs. MRTM2 full	Slope	0.869 (0.004)	0.861, 0.878	0.960
	Intercept	0.192 (0.006)	0.181, 0.203	
SUVR 60-80 vs. MRTM2 full	Slope	0.945 (0.004)	0.937, 0.954	0.964
	Intercept	0.112 (0.006)	0.101, 0.123	
SUVR 70-90 vs. MRTM2 full	Slope	1.002 (0.005)	0.993, 1.011	0.964
	Intercept	0.052 (0.006)	0.040, 0.063	

Table 3.7[^{18}F]MK-6240 Regression Summary Statistics

As mentioned previously, it is desirable to reduce the PET scan duration to accommodate aging and symptomatic individuals that can experience discomfort, and to maximize the efficiency of the tomograph usage in multi-tracer studies. While DVR estimates were stable using as little as 60 minutes of dynamic data, SUVR quantification with static imaging may be more practical for persons with AD since the overall emission scan duration can be reduced to 20-minutes and still achieve binding estimates comparable to DVR methods.

The selection of the scan duration for SUVR estimation with [^{18}F]MK-6240 involves a trade-off between unwanted spill-in from sites outside of the brain with the accuracy of quantification. In particular, regions that could potentially influence cortical binding estimates (ethmoid, clivus and meninges) had SUVRs that were increasing through 120 minutes. Notably, signal in the ethmoid sinus was observed to spill into the orbitofrontal cortex, which could limit quantification of tau-related signal. In contrast, SUVRs in target regions were in agreement with DVR estimates when using data from 70-90 minutes, although SUVRs in target regions were still increasing in higher binding AD subjects at this time. Taken together, this suggests that the 70-90 minute acquisition window will produce accurate binding estimates while reducing potential contamination from off-target binding. This may need to be re-evaluated in studies looking to characterize changes (longitudinal and therapeutic intervention) in SUVR in high binding AD subjects.

A limitation of this study was the absence of arterial blood sampling, which would have provided the gold standard comparison for the DVR and SUVR estimates. However, since there has been extensive evaluation of the cerebellum as a reference region with other tau tracers(60, 132, 135, 150) and the cerebellum is used in large-scale tau PET neuroimaging studies (82, 84, 112) it is likely the results presented in this work will accurately represent comparisons with arterial derived specific binding estimates, but this should be confirmed.

3.5 Case Study Comparison of [^{18}F]THK-5317, [^{18}F]THK-5351, and [^{18}F]MK-6240

During the course of evaluating the NFT PET radiotracers investigated in this chapter, there were five participants that underwent PET scans with all three tau tracers ([^{18}F]THK-5317, [^{18}F]THK-5351, and [^{18}F]MK-6240). These studies were carried out as the radiotracers were made available for development and study protocols were approved for humans investigation resulting in [^{18}F]THK-5317 and [^{18}F]THK-5351 scans being acquired 2.79±0.17 years and 1.87±0.18 years prior to the [^{18}F]MK-6240 scans and always in the same order ([^{18}F]THK-5317 first, [^{18}F]THK-5351 second, and [^{18}F]MK-6240 third). Despite physiological changes that could have occurred during the time between scans, there were still useful observations with regard to the extent of *in vivo* target and off-target binding of the THK compounds. This section gives direct comparison of the three NFT radiotracers in human subjects.

3.5.1 Methods

Participants and Image Processing

Participants in this section represent a subset of those included in sections 3.3 and 3.4. Cognitive groups were determined based on the most recent neuropsychological evaluation nearest to the [^{18}F]MK-6240 scan. Descriptive statistics and the time gap between PET scans is given in Table 3.8. Image acquisition and processing methods were the same as described previously in this chapter.

Age	Sex	Group	CDR	MMSE	PiB	[^{18}F]MK-6240 Equivalent NFT Stage	Δt THK-5317 to MK-6240 [years]	Δt THK-5351 to MK-6240 [years]
77	F	MCI	0	28	+	2	2.75	1.98
72	F	MCI	0	30	+	5	3.06	2.01
64	F	OC	0	30	+	0	2.64	1.71
67	F	CD	0	29	+	4	2.65	1.63
59	F	OC	0	30	-	0	2.84	2.00

Table 3.8 Summary of Participants with [^{18}F]THK-5317, [^{18}F]THK-5351, and [^{18}F]MK-6240

[^{18}F]THK-5317 and [^{18}F]THK-5351 MRTM2 DVR and [^{18}F]MK-6240 SUVR(70-90 min) parametric images were coregistered to the most recent T1-w MRI scan (closet to the [^{18}F]MK-6240 scan). No attempt was made to account for registration bias that may have occurred due to the temporal differences between PET and MRI scans. Regional DVR and SUVR values were extracted from the parametric images using AAL ROIs modified as described in section 3.4 (restricted to GM).

Analysis

Coregistered PET images were visually assessed in native MRI space to compare image features in target and off-target regions. Since the spatial distributions of the individual tracers were described in previous sections, the image review focused primarily on comparing the similarities and differences observed within individual cases.

Linear regression was used to compare binding estimates between all three radiotracers in NFT rich target regions (parahippocampus, fusiform, inferior, middle and superior temporal, inferior parietal, supramarginal, inferior occipital, and middle and superior medial frontal cortex and the precuneus) and MAO-B rich off-target regions (caudate, putamen, pallidum, and thalamus). ROIs were selected based on binding patterns observed with all three radiotracers, the distribution of NFTs in neuropathology and [^{18}F]T807 PET studies (15, 22, 81, 82), and the distribution of MAO-B observed in [^{11}C]-L-deprenyl PET studies *in vivo* (151-153).

3.5.2 Results

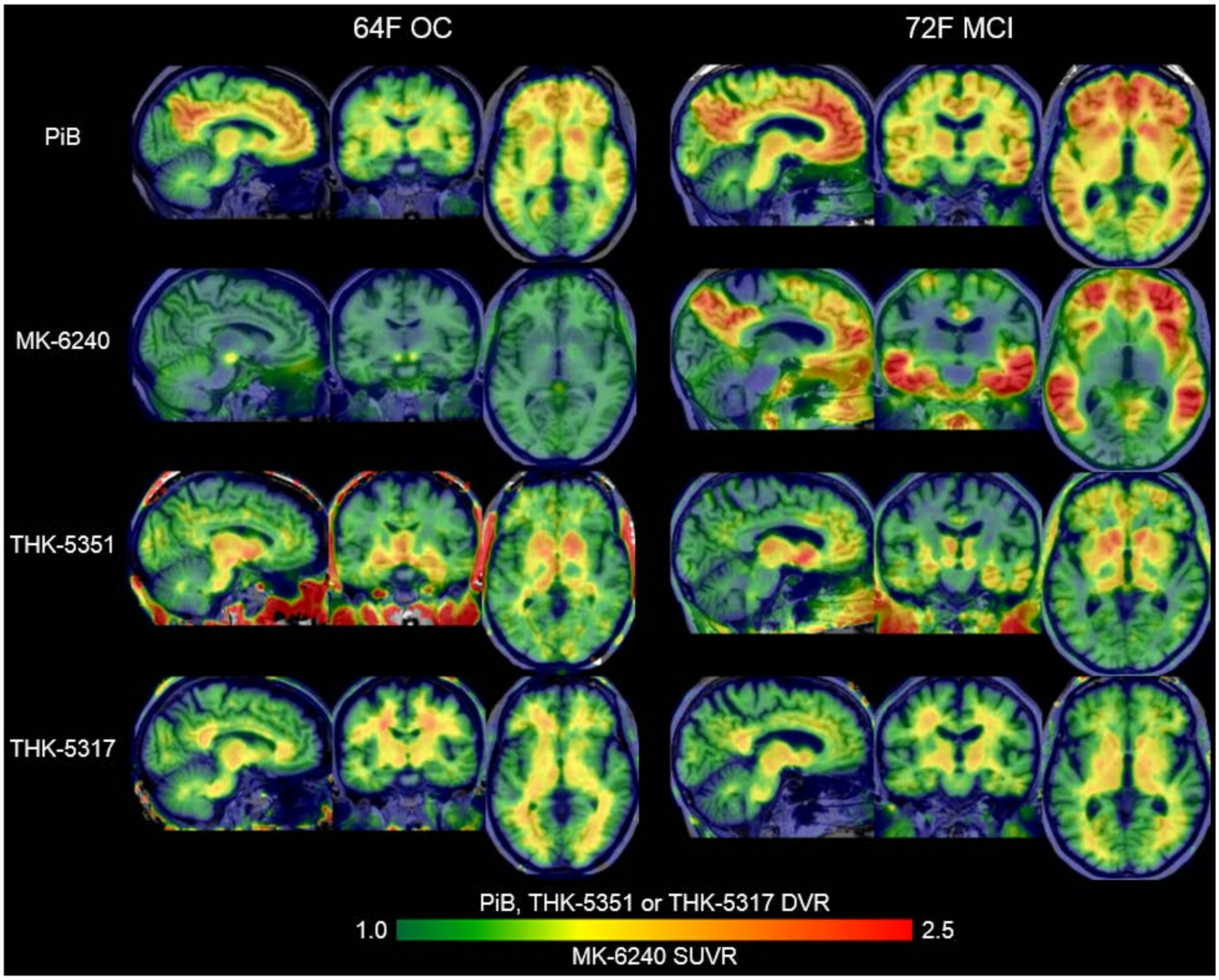

Figure 3.21 Image Comparison of [^{18}F]MK-6240, [^{18}F]THK-5351, and [^{18}F]THK-5317

THK compounds indicated high binding in the basal ganglia, which was highest for [^{18}F]THK-5351, whereas [^{18}F]MK-6240 was devoid of binding in these regions (Figure 3.21). In two subjects with [^{18}F]MK-6240 binding consistent with neuropathological NFT stage V and SUVRs as high as four, [^{18}F]THK-5351 binding was only slightly elevated and [^{18}F]THK-5317 binding was mostly precluded by high non-specific binding even when viewed with lower maximum thresholds than those shown in Figure 3.21. In a PiB(+) subject with [^{18}F]MK-6240 binding consistent with Braak II NFT staging, both [^{18}F]THK-5351 and [^{18}F]THK-5317 binding in the hippocampus and entorhinal cortex was lower and had a greater spatial extent than [^{18}F]MK-6240.

Figure 3.22 shows the scatter plots comparing [^{18}F]MK-6240, [^{18}F]THK-5351, and [^{18}F]THK-5317 in the five cases with the summary of the linear regressions of target and off-target regions given in Table 3.9. [^{18}F]MK-6240 SUVR was nearly a factor of two higher in high binding target regions ([^{18}F]MK-6240 SUVR = 3). [^{18}F]MK-6240 appeared somewhat linear with THK compounds in target regions, which was more apparent for [^{18}F]THK-5317. In off-target regions associated with MAO-B (i.e. basal ganglia), [^{18}F]MK-6240 SUVR was centered around one (0.94±0.57 mean SUVR±SD) and was not correlated with DVR for

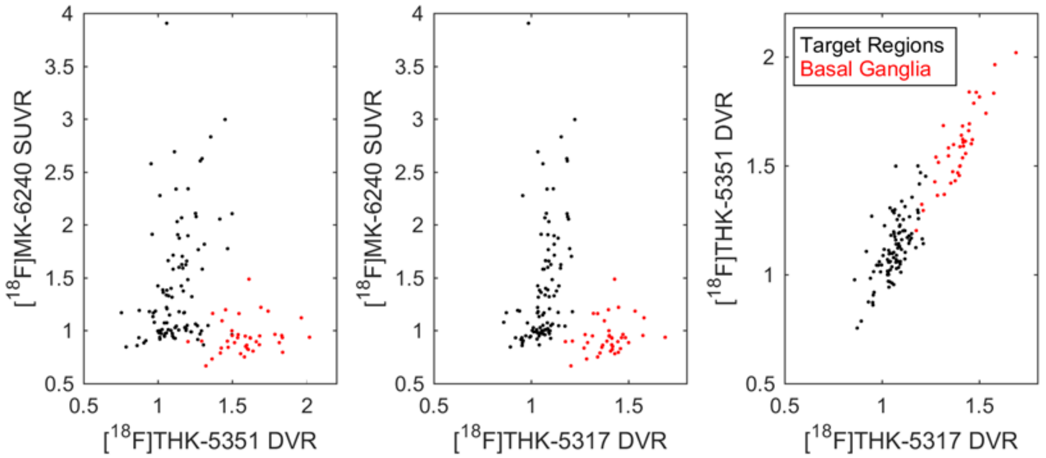

Figure 3.22 Comparison of [^{18}F]THK-5317, [^{18}F]THK-5351, and [^{18}F]MK-6240

Regression	Coefficient	Target Regions			Off-Target Regions		
		B	95% CI	R^2	B	95% CI	R^2
MK-6240 vs. THK-5351	Slope	1.30	(0.54, 2.06)	0.11	0.14	(-0.15, 0.43)	0.03
	Intercept	-0.05	(-0.90, 0.81)		0.71	(0.25, 1.18)	
MK-6240 vs. THK-5317	Slope	3.09	(1.67, 4.51)	0.16	0.40	(-0.09, 0.89)	0.07
	Intercept	-1.88	(-3.39, -0.36)		0.38	(-0.31, 1.06)	
THK-5351 vs. THK-5317	Slope	1.31	(1.03, 1.60)	0.46	1.52	(1.24, 1.79)	0.77
	Intercept	-0.27	(-0.58, 0.03)		-0.53	(-0.91, -0.15)	

Table 3.9 Regression Comparisons of [^{18}F]MK-6240, [^{18}F]THK-5351, and [^{18}F]THK-5317

either THK compound ($R^2 \leq 0.07$). However, the plots between [^{18}F]THK-5317 and [^{18}F]THK-5351 were highly linear and were moderately correlated in target regions ($R^2=0.46$) and strongly correlated in off-target regions ($R^2=0.77$).

3.5.3 Discussion

Specific binding of radioligands targeting NFT pathology should recapitulate the hierarchical spatial organization observed in neuropathology studies, including early stages, which would support the specificity and sensitivity of the radioligand for detecting NFT pathology *in vivo*. [^{18}F]MK-6240 spatial binding patterns were far more consistent with neuropathological staging of NFTs, especially in PiB(+) individuals with elevated binding in NFT stage I and II regions. Interestingly, neuropathology literature often observe sparse tau tangles in NFT stages I and II that are devoid of Aβ plaque pathology(22), whereas, with the exception of one individual, [^{18}F]MK-6240 was only observed in PiB(+) individuals. This discord is likely due differences in sensitivity between [^{11}C]PiB and [^{18}F]MK-6240 PET imaging and histopathology studies, which are capable of identifying pre-tangles(21) and individual tau tangles. Additionally, there are differences between binding targets of immunohistopathological markers targeting phosphorylated tau (Ser202, Thr205) and PET tracers, which are sensitive to protein conformational changes(57, 60, 77), that occur after hyperphophorylation(24). These preliminary [^{18}F]MK-6240 data are also in agreement with the biomarker cascade proposed by Jack, et al. suggesting that detectable *in vivo* changes in Aβ occur prior to detectable changes in pathological tau (41, 42, 154). To a lesser extent than [^{18}F]MK-6240, THK compounds do have some correspondence with NFTs, but interpretation of the *in vivo* signal is confounded by off-target binding as is detection of NFTs in early affected regions (e.g. entorhinal cortex and hippocampus).

The most obvious deviation from neuropathological NFT staging with regard to the THK tracers is the high *in vivo* signal present in the thalamus, striatum, and the cingulate cortex, even in mid 50’s PiB(-) cognitively stable individuals. This binding for [^{18}F]THK-5351 has been shown to be reduced *in vivo* with pharmacological doses of a MAO-B inhibitor L-deprenyl (aka selegiline)(138) and is consistent with spatial patterns observed in [^{11}C]-L-deprenyl PET studies(151, 153). Interestingly, a recent *in vitro* study comparing several tau PET radioligands (T807, THK-5117, THK-5351 and PBB3) observed competition between THK-

5351 and both THK-5117 and T807 with a similar affinity for a high affinity binding site (0.2 pM, 0.3 pM, 0.2 pM for THK-5351, THK-5117, and T807, respectively), but different affinities for a second moderate binding site (16 nM, 20 nM, and 78 nM for THK-5351, THK-5117, and T807, respectively)(139), and also observed competition with THK-5117 and T807 and [^{3}H]L-deprenyl in the putamen and hippocampus with much lower affinities (145 nM and 135 nM for THK-5117 and T807, respectively). The authors conclude that THK-5351 binds to MAO-B and NFTs with high affinity, and that the MAO-B binding relative to NFT binding is lower for THK-5117 suggesting the latter will be a suitable tracer for detecting NFTs *in vivo*. However, the results presented in this section contrasting MK-6240 and THK compounds suggest that both THK tracers bind to MAO-B and with similar relative affinities to NFTs. This is evidenced by several *in vivo* observations in this chapter. 1) Comparisons of binding estimates between [^{18}F]MK-6240 and THK compounds showed different relationships in NFT rich, MAO-B poor and NFT poor, MAO-B rich regions where [^{18}F]MK-6240 binding was not observed in MAO-B rich regions. 2) [^{18}F]MK-6240 binding was not correlated with either THK compound in the basal ganglia ($R^2 \leq 0.07$) and was poorly correlated in NFT target regions. 3) Comparisons of binding estimates between THK compounds were highly linear and highly correlated in both NFT rich ($R^2 = 0.46$) and MAO-B rich ($R^2 = 0.77$) regions. 4) THK compounds indicated high binding in MAO-B rich regions in all subjects studied in this chapter, including PiB(-) individuals whereas no PiB(-) individuals indicated elevated [^{18}F]MK-6240 binding in these same regions. The differences observed between these *in vivo* observations and the *in vitro* studies(94, 139) may be attributed to *in vitro* tissue sample preparation, which has been shown to be responsible for a lack of MAO-B binding in autoradiography(94, 155). Regardless of the *in vitro* evidence, the *in vivo* evidence overwhelmingly points towards both [^{18}F]THK-5351 and [^{18}F]THK-5317 having high affinity for MAO-B. This could be confirmed for [^{18}F]THK-5317 by performing an *in viv o*r MAO-B inhibition study similar to that performed for [^{18}F]THK-5351(138).

On Repurposing THK Compounds

Beyond tau imaging, considerable resources have been put towards developing PET radiopharmaceuticals for detecting and monitoring neuroinflamation(156-159), which is suggested to be systemically elevated during neurodegenerative disease processes(4, 160). A recent [^{18}F]THK-5351 study anteceding the discovery of *in vivo* MAO-B binding suggested that *in vivo* [^{18}F]THK-5351 binding may be a marker of neuroinflmmatory processes. However, this study along with the present work suffer from a major methodological confound for reference tissue analysis of THK compounds. Namely, MAO-B is present in the cerebellum and increases with age (~7% per decade)(152). Ng and colleagues showed that [^{18}F]THK-5351 SUV was decreased by >40% in the cerebellum following administration of L-deprenyl, which provides evidence of the extent of MAO-B contamination in the proposed reference region. Thus, reference regions other than the cerebellum (e.g. WM or pons) would need to be explored and validated prior to implementation of THK compounds for other applications. Even if a suitable reference region does exist for THK compounds, their application to neuroinflammation is likely not likely warranted given the abundance of translocator protein PET radiotracers, which monitor processes less distal to neuroinflammation than THK compounds, and the PET signal binds to at least two targets (NFTs and MAO-B), which both have individual effects with disease in humans and thus interpretation would be greatly limited.

3.6 NFT PET Imaging Summary and Conclusions

This chapter demonstrated the need for thorough evaluation of novel PET radiopharmaceuticals and quantification strategies used for NFT imaging. Selection of the optimal quantification method is a compromise between quantification accuracy and precision, tracer binding features, and participant comfort considered in the context of study or clinical application. This was demonstrated for both THK compounds wherein different DVR and SUVR methods produced differences in non-specific WM binding estimates relative to GM specific binding, and for both THK compounds and [^{18}F]MK-6240 where the optimal SUVR timing windows were a balance between accurate quantification and minimizing spill-in from signal outside of GM ROIs that increased at later time points.

As next-generation NFT PET tracers continue to become available, comparisons between new and existing PET radioligands will allow researchers to better understand and characterize binding specificity, sensitivity, and the limitations associated with *in vivo* NFT imaging. The comparisons made between [^{18}F]MK-6240, a more selective NFT radiotracer, and the THK compounds elucidated the extent of off-target MAO-B binding for THK compounds and gave a sense of how much this signal will confound detection of NFT pathology or other proposed applications. This work also provided further evidence of the discordance between *in vitro* binding assays and *in vivo* PET signal, which continues to be observed with NFT PET radioligands and highlights the difficulty of identifying and screening PET radiopharmaceuticals for *in vivo* NFT imaging in humans.

The striking agreement between spatial patterns observed with [^{18}F]MK-6240 binding and neuropathological staging of NFTs is highly encouraging for detection of NFTs and for characterizing the *in vivo* topographical spatiotemporal development of tau pathology along the AD continuum. When comparing PET imaging studies with neuropathological or other AD biomarkers (e.g. CSF assays), it is important to consider differences in detection efficiency and molecular targets between these methods. Without this context, the finding that elevated [^{11}C]PiB binding occurs prior to elevated [^{18}F]MK-6240 would suggest Aβ plaque deposition precedes NFT deposition, which is contraindicated by neuropathology studies where NFTs in early stages are commonly observed prior to Aβ plaques. Much of these differences can be explained when considering differences in the relative concentrations of the aggregates, detection thresholds of molecular probes, and differences in molecular targets for the same pathological feature (e.g. for tau: phosphorylation sites (CSF and immunohistochemical), argyrophilic properties (histochemical), or protein conformation-specific binding sites (PET)). Further characterization of molecular biomarkers in multimodal studies, and antemortem to postmortem evaluation is needed to understand these nuances. Despite the above differences, preliminary studies and evaluation of NFT radiotracers like [^{18}F]MK-6240 indicate PET will provide much needed insight into the pathological process of NFT aggregation and interactions between NFTs and other pathological changes occurring in AD.

CHAPTER 4

DOSIMETRIC CONSIDERATIONS FOR PET IMAGING

Chapter 4 was adapted with permission from Elsevier from (161).

Multi-tracer PET studies are becoming the norm in longitudinal AD research owing to the complex interactions of pathological features and neurobiological systems (e.g. NFTs, Aβ plaques, neuroinflammation, glucose metabolism, etc.)(91) and the availability of specific PET radioligands that can uniquely monitor targets antemortem. While PET studies provide needed insight into pathological changes occurring in AD, they also involve administration of radioisotopes that emit ionizing radiation, which causes damage to tissues within the body. Thus, an increasingly important characteristic of PET radiotracers used in AD research is that individual participants are not exposed to unreasonable levels of radiation within a single PET scan and over several PET scans in multi-tracer studies.

4.1 Radiation Dosimetry and PET Imaging of Cholinergic Receptors

Internal Radiation Dosimetry

Quantifying the radiation burden of PET radiopharmaceuticals is the focus of internal radiation dosimetry. During development of radiopharmaceuticals, radiation doses are estimated in rodents and extrapolated to humans prior to translation to approximate a safe injectable dose. If a radioligand shows potential for promise, radiotracer biodistribution and internal dosimetry estimated are reevaluated in human subjects using whole body (WB) PET scans. The method for estimating the internal radiation dose burden was established by the Society of Nuclear Medicine Medical Internal Radiation Dose Committee (referred to as the MIRD method), which prompted the development of reference phantoms(162) and software packages (MIRDOSE(163), OLINDA(164)) to standardize quantification of radiation burden for parenterally administered radiopharmaceuticals(165). Radiation dose limits for human PET studies are specified in FDA 21 CFR 361.1 and are summarized in Table 4.1.

Organs	*Limit Type*	*Dose Limit [rems]*
Whole body, active blood-forming organs, lens of the eye, and gonads	Single Dose	3
	Annual and Total Dose Commitment	5
Other organs	Single Dose	5
	Annual and Total Dose Commitment	15

Table 4.1 FDA 21 CFR 361.1 Radiation Dose Limits for Radioactive Drugs

The MIRD method uses modeling to derive a series of equations that take into account the spatial and temporal distribution of the radiotracer and radioisotope decay products and there biological effects. Residence times (the amount of time the radioisotope occupies an organ) are calculated for source organs (organs that have significant uptake of the radioisotope) by integrating TACs from WB PET imaging extrapolated to infinity, multiplying by organ mass and dividing by the injected dose. Residence times are then multiplied by weighting factors that account for the biological effects of the radioisotope decay products, spatial relationships within and between source organs and target organs, and standard organ masses for each organ resulting in dose estimates for individual organs. Organ doses are then multiplied by organ weighting factors to establish a global measure of radiation burden (effective dose or effective dose equivalent, which differ in organ weighting factors), which allows comparison with risks posed by exposure to other source of ionizing radiation (e.g. CT or x-ray imaging, background atmospheric radiation, high-altitude flight, etc.).

The Cholinergic Hypothesis

Dysregulation of the cholinergic system, hypothesized to be caused by a loss of cholinergic neurons in the basal forebrain, is associated with functional and cognitive symptoms in AD(166, 167). Nicotinic acetylcholine receptors (nAChRs), which are decreased in AD concomitant with co-localization of Aβ plaques and NFTs, are associated with learning, memory and cognition(4). NAChRs with α4β2 subunits are the most abundant nAChR in the human brain(168), have been shown to be inhibited by the Aβ protein (169), are present in glial processes (170), and have been shown to have associations between receptor loss and memory deficits in AD(171). Further, acetylcholinesterase, an enzyme involved in catalyzing degradation of acetylcholine, has been shown to be associated with NFT and Aβ plaques(172). Findings relating the cholinergic system with cognitive deficits and dysregulated processes in AD ultimately led to the development of several FDA approved acetylcholinesterase inhibitors that can moderately improve cognitive symptoms of MCI and early AD patients(4) and remain a mainstay in symptomatic treatment of AD.

PET Imaging of the Nicotinic Acetylcholine Receptor System

Ongoing studies investigating the role of the cholinergic system in disease and addiction has spurred development of several PET(173-181) and SPECT(182) radiotracers designed to target nAChRs. First generation PET radioligand 2-[^{18}F]FA-85380 (2-FA, (173)) has enabled in vivo characterization of α4β2* nAChRs (* indicating heteromeric combinations of α4 and β2 subunits with other α and β subunits) in AD(183), but suffered from slow pharmacokinetic properties resulting in long uptake and PET scan durations. Several second generation α4β2 nAChR PET radioligands have since been developed to improve on the slow kinetic properties of 2-FA(175-177, 181). [^{18}F]Nifene is a high affinity α4β2* nAChR partial agonist PET radioligand(184) that has demonstrated rapid in vivo kinetics in non-human primates(185) and in humans(186), and shows promise for imaging α4β2 nAChRs in addiction and disease(184). Prior to translation to humans, internal dosimetry was investigated in mice(187) and extrapolated to humans, but requires validation in human. The focus of this section is to evaluate the biodistribution and radiation burden of [^{18}F]nifene in humans, facilitating safe study of the α4β2 nAChR* system in humans.

4.2 Materials and Methods

Study Participants

Four participants (2M, 2F) aged 27 to 78 years were recruited for whole-body PET/CT imaging. Individuals were included for the study if they were between the ages of 18-88 years and had a BMI of 22-28. Participants were excluded from the study if they were taking medication that would directly interact with the α4β2* nAChR system, were pregnant or nursing, or had participated in the brain characterization portion related to this human evaluation study(186). Prior to imaging, participants underwent a medical history evaluation, physical examination, echocardiogram, and blood and urine were collected for a blood chemistry profile, complete blood count, and urinalysis. Nonpregnant status was determined by a urine test for females. Vital signs were monitored once participants were positioned on the scanner bed and repeated periodically for a minimum of two hours after injection of [^{18}]nifene. Following the PET scan, the pre-scan tests were repeated with the exception of the medical history review and pregnancy test. Written informed consent was obtained from all individuals prior to participation in the study. All human studies were approved by the University of Wisconsin-Madison Institutional Review Board approval and carried out under the FDA IND mechanism.

Radiochemical Synthesis and [^{18}F]Nifene PET/CT Imaging

[^{18}F]Nifene was synthesized at the University of Wisconsin Waisman Center according to previously reported methods (185). Imaging data were acquired on a Discovery 710 PET/CT (GE Healthcare) at the University of Wisconsin Institute of Medical Research. Prior to imaging, participants were positioned supine with arms at their sides and immobilized. A low-dose computed tomography (CT) scan was obtained and used for anatomical ROI delineation and PET attenuation correction. WB PET acquisition commenced with bolus injection of a 189±8 MBq dose of [^{18}F]nifene administered in the antecubital vein. WB PET scans consisting of eight bed positions each were acquired starting with bolus injection (30 s/bed), and at 10 (30 s/bed), 21 (1 min/bed), 36 (2 min/bed), and 59 (3 min/bed) minutes post injection, spanning spatially from the top of the head to mid-thigh. Two subjects were scanned head to thigh and the direction was reversed for the remaining two subjects. Participants remained immobilized for the entire duration of the study to avoid registration errors.

PET Data Analysis and Residence Time Calculation

PET Processing and Data Extraction: PET data were reconstructed using OSEM (Vue Point FX-TOF, 3 iterations, 24 subsets, 4.4 mm Gaussian smoothing, 192 x 192 x 299 matrix, and 3.65 x 3.65 x 3.27 mm) and corrected for attenuation (CT-based), scatter, deadtime, and radioactive decay to the beginning of bolus injection. Regions of interest (ROIs) were hand drawn on CT images for source organs that indicated elevated uptake relative to background, which included brain, gallbladder, heart, kidneys, liver, lower large intestine, lungs, muscle (ROI in gluteal muscle), pancreas, small intestine, red marrow (ROI in lumbar spine), spleen, stomach, and urinary bladder. ROIs were drawn proximal to organ boundaries to mitigate partial volume effects. Time-activity curves (TACs) were extracted for all source organs. In the case where an organ spanned multiple bed positions, multiple time points were included in TACs, one for each bed position. *Residence Time Calculation:* TACs normalized to injected radioactivity and body mass (standard uptake value, SUV) were fit to one of three exponential models based on the shape of the SUV TACs and expected physiological clearance using code developed in our lab (MATLAB 2015a). Fitting parameters were used to generate model data incorporating radioactive decay with one-minute sampling intervals for each source organ spanning a total of ten F-18 half-lives (1090 min, representing >99.99% of all decays) assuming extrapolated values beyond the scan duration. Residence times for each organ were calculated by integrating the model SUV data (trapezoidal method) and multiplying by the ratio of organ mass to the whole body mass. The residence time for the rest of the body was determined by subtracting the residence time of ^{18}F in hours (2.64 hours) from the sum of all source organ residence times.

Organ	Residence Time [h]
Brain	0.050 ± 0.014
Gallbladder Contents	0.010 ± 0.008
Heart Contents	0.032 ± 0.004
Kidneys	0.057 ± 0.017
Liver	0.177 ± 0.019
Lower Large Intestine	0.017 ± 0.009
Lung	0.026 ± 0.009
Muscle	0.684 ± 0.076
Pancreas	0.004 ± 0.002
Small Intestine Contents	0.097 ± 0.022
Red Marrow	0.162 ± 0.062
Spleen	0.012 ± 0.002
Stomach	0.037 ± 0.026
Urinary Bladder (no voiding)	0.363 ± 0.122
Urinary Bladder (with voiding)	0.186 ± 0.056
Rest of Body	0.914 ± 0.137

Table 4.2 [^{18}F]Nifene Source Organ Residence Times

Organ	Dose [μSv/MBq]	Dose with Voiding [μSv/MBq]
Adrenals	12.10 ± 0.56	12.03 ± 0.57
Brain	10.41 ± 2.19	10.41 ± 2.19
Breasts	6.22 ± 0.50	6.20 ± 0.51
Gallbladder Wall	28.53 ± 12.99	28.30 ± 13.06
LLI Wall	24.93 ± 5.82	22.53 ± 4.82
Small Intestine	30.80 ± 4.39	29.90 ± 4.35
Stomach Wall	23.10 ± 9.37	22.95 ± 9.38
ULI Wall	14.53 ± 0.79	13.83 ± 0.94
Heart Wall	15.78 ± 0.80	15.78 ± 0.80
Kidneys	42.28 ± 10.08	42.13 ± 10.00
Liver	26.75 ± 2.31	26.65 ± 2.31
Lungs	10.30 ± 1.52	10.30 ± 1.52
Muscle	10.73 ± 0.38	10.13 ± 0.59
Ovaries	16.45 ± 1.11	14.23 ± 0.52
Pancreas	17.60 ± 3.92	17.50 ± 3.92
Red Marrow	20.30 ± 4.18	19.90 ± 4.20
Osteogenic Cells	17.20 ± 1.94	16.98 ± 1.94
Skin	6.01 ± 0.39	5.80 ± 0.48
Spleen	19.83 ± 2.96	19.75 ± 2.92
Testes	10.17 ± 0.61	8.55 ± 0.64
Thymus	8.15 ± 0.60	8.14 ± 0.61
Thyroid	7.47 ± 0.73	7.46 ± 0.73
Urinary Bladder Wall	179.75 ± 56.67	96.40 ± 25.73
Uterus	21.88 ± 2.90	16.60 ± 1.17
Total Body	11.68 ± 0.17	11.18 ± 0.43
Effective Dose Equivalent	28.38 ± 3.77	22.63 ± 1.88
Effective Dose	24.90 ± 4.30	19.88 ± 2.55

Table 4.3 Human Radiation Dose Estimates of [^{18}F]Nifene

Radiation Dose Estimation

OLINDA software (V1.1) was used to estimate organ and whole body effective radiation dose (164). Residence times were entered into OLINDA for all source organs and dose estimates were obtained using the hermaphroditic adult phantom (162). Since urinary bladder voiding was not performed during the study, a voiding model(188) was implemented in OLINDA. The bladder-voiding model assumed hourly micturition following injection of the radiotracer, and used parameter estimates from the residence time calculation to determine the excretion fraction and biological half-life of the urinary clearance. Dose estimates are reported both with and without the use of the bladder-voiding model.

4.3 Results

There were no adverse events or clinically significant changes observed during the course of this study. SUV TACs for all source organs are provided in Figure 4.1. Dosimetry estimates and visual

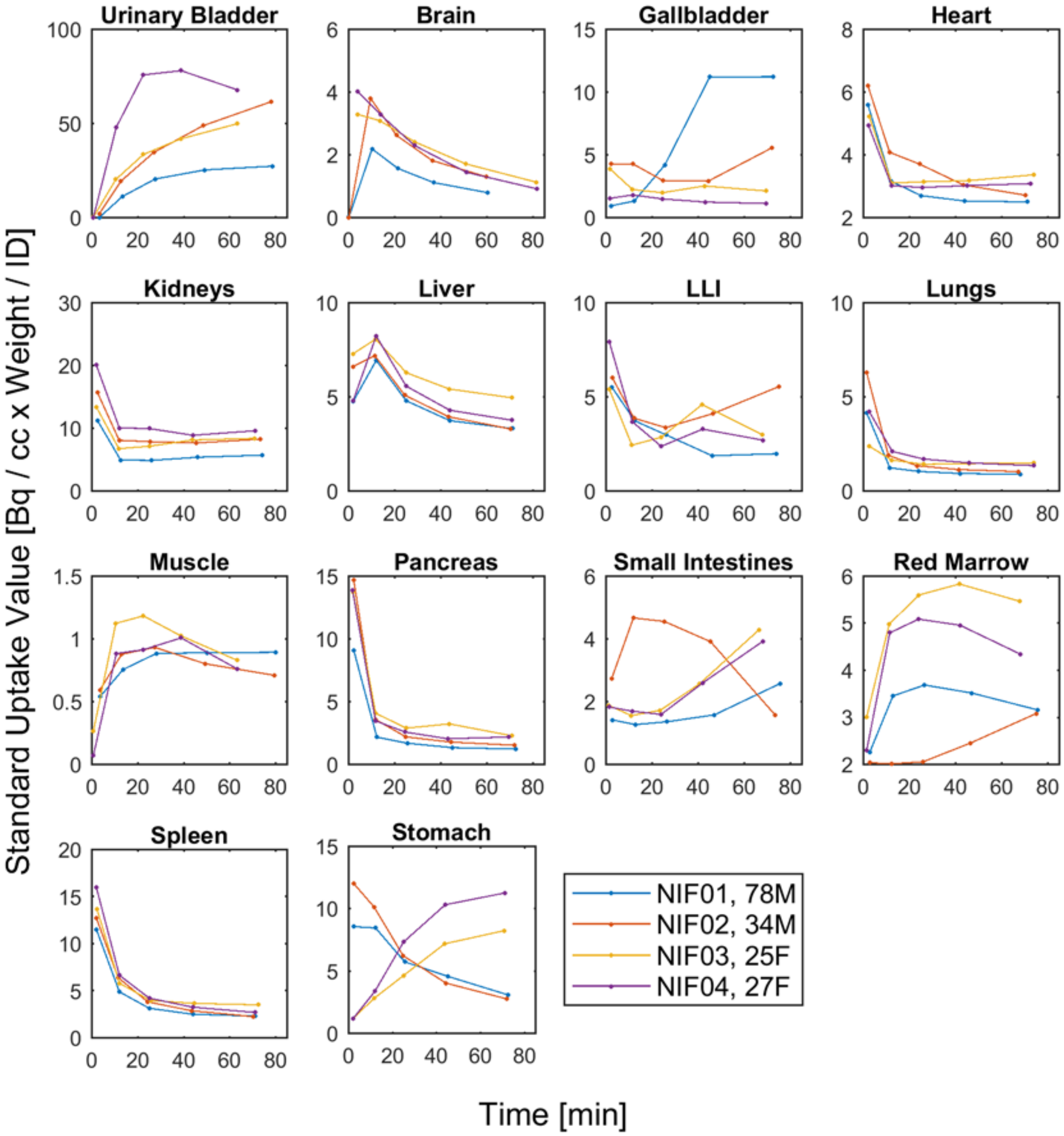

Figure 4.1 Source Organ Time-Activity Curves for [^{18}F]Nifene in Humans

assessment of whole body images indicated the renal pathway as the primary clearance mechanism of [^{18}F]nifene (Figure 4.2). Parameterization of the urinary bladder clearance indicated a mean %ID of 35%±10% with a mean biological half-life of 19±10 min. In the older male subject, high retention was observed in the gallbladder, but this was not observed in other subjects.

Table 4.2 gives the average residence times for male and female subjects for all source organs including the urinary bladder with and without voiding. Human dosimetry estimates are given for the hermaphroditic male phantom in Table 4.3. The highest organ dose was observed in the urinary bladder wall (1.80E-01 mSv/MBq without voiding, 9.64E-02 mSv/MBq with bladder voiding), followed by the kidneys, small intestine, gallbladder wall and liver. The mean effective dose across the four subjects was 24.9±4.3 μSv/MBq.

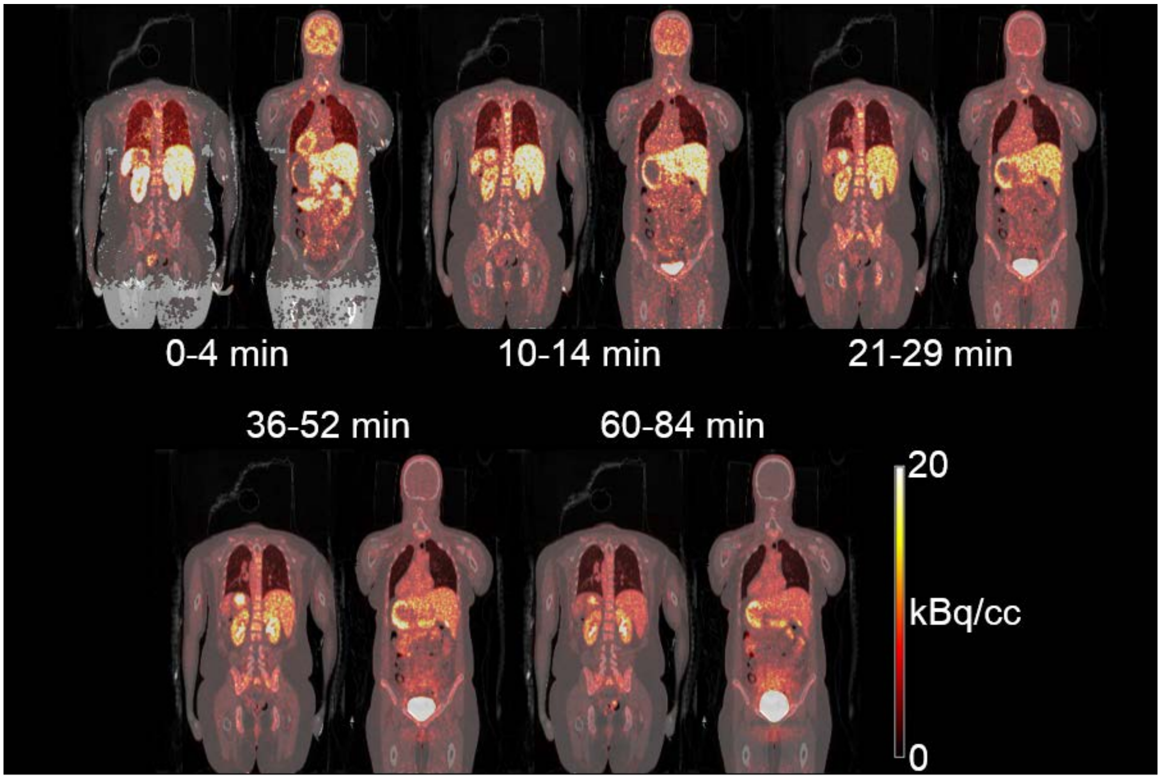

Figure 4.2 Whole Body Biodistribution of [^{18}F]Nifene in a Female Human

4.4 Discussion

These data provide measurements of the WB biodistribution and source organ residence times of [^{18}F]nifene in four subjects, which were used to estimate the radiation burden of [^{18}F]nifene in humans.

Radiation dose limits specified in 21 CFR 361.1 sets maximum doses of three rem per scan for whole body, blood-forming organs, lens of the eye, and gonads, and five rem per scan for other organs. In this context, the urinary bladder is the dose-limiting organ for [^{18}F]nifene. Based on the maximum allowable dose of five rem for the urinary bladder, the maximum injected dose is 278 MBq (7.5 mCi) without bladder voiding, and 519 MBq (14 mCi) when bladder voiding is performed hourly following dose administration. Previous human neuroimaging studies performed as part of this first-in-human evaluation of [^{18}F]nifene (186) indicate that a 185 MBq injection of [^{18}F]nifene is sufficient to obtain reliable binding estimates in the brain, which would result in a WB effective dose of 0.5 rem and a urinary bladder dose of 3.33 rem per scan (1.78 rem with hourly voiding). This would allow for up to four 185 MBq [^{18}F]nifene scans within the period of a year, which is beneficial for studies that might require baseline and subsequent follow-up scans, such as blocking and interventional drug development paradigms.

The biodistribution of [^{18}F]nifene has been previously studied in BALB/c mice and dose estimates were extrapolated to humans (187). Overall, the preclinical biodistribution was consistent between species. However, the magnitude of the dose estimates was lower using the data from mice, particularly for clearance organs (urinary bladder, kidneys, and gastrointestinal organs). In most organs, human dose estimates derived from mouse data were lower (-19%±31% mean difference across all organs) than dose estimates derived from human subjects. Additionally, the WB effective dose was 37% lower using mouse data. However, when the interspecies comparison was made implementing the bladder-voiding model in humans, the dose estimates between species showed better agreement (-15%±29% mean difference across all organs, WB effective dose was 21% lower in mouse data). This suggests that differences in renal clearance are responsible for a considerable amount of the discrepancies between species. In this case, mouse models provide good initial estimates of radiotracer dosimetry, however the differences between mouse and human dose estimates highlight the need for confirmation of dosimetry in the species intended for study.

Human dosimetry studies have been performed for several ^{18}F-labeled α4β2* nAChR PET tracers (175, 189, 190) and are compared to [^{18}F]nifene in Figure 4.3. Overall, individual organ doses and whole body effective doses are similar between the various radiotracers with the greatest differences present in the urinary bladder wall. When bladder voiding is performed, the urinary bladder wall dose is only slightly higher for [^{18}F]nifene when compared to 2-[^{18}F]FA, [^{18}F]Flubatine, and [^{18}F]AZAN. A recent study performed in mice and extrapolated to humans (176) suggests another second-generation α4β2* PET tracer ([^{18}F]XTRA) has a urinary bladder wall dose nearly five times higher than other ^{18}F-labeled α4β2* nAChR tracers. When considering kinetics and imaging characteristics of the various tracers that have been studied in humans, an advantage of [^{18}F]nifene is the rapid stability of DVR estimates, which results in short scan durations (~40 min dynamic scan) for quantification of neuroreceptor binding. Given the high bladder dose of α4β2* nAChR tracers, [^{18}F]nifene is more favorable from a dosimetry standpoint since shorter scans enable earlier bladder voiding resulting in considerably lower radiation burden.

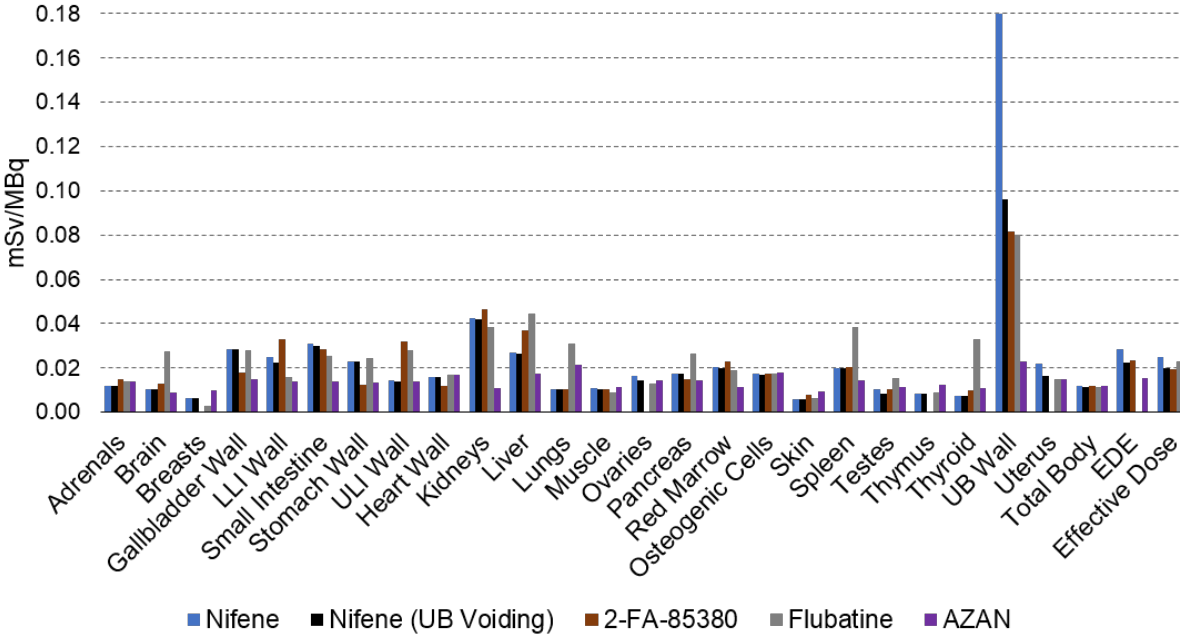

Figure 4.3 Comparison of α4β2 nAChR PET Radioligand Human Dosimetry Estimates*

4.5 Summary and Conclusions

Longitudinal multi-tracer PET studies are becoming more common to investigate the interactions between several molecular targets in a variety of applications. As such, the internal radiation burden received during the course of study is becoming an increasingly important feature of PET radiopharmaceuticals and imaging protocol design. This is especially true in European countries, which often have more restrictions for lifetime radiation burden from research studies. Radiotracers that demonstrate rapid metabolism and clearance primarily through the renal system are advantageous for reducing radiation burden since they can be quickly excreted thereby limiting the quantity and time of exposure to injected radioactivity. This was demonstrated by the considerable reduction in radiation dose observed with [^{18}F]nifene when implementing the bladder voiding model.

Extrapolation of non-human dosimetry estimates to humans provides a useful starting point for safe administration of PET radiopharmaceuticals in initial human studies. However, differences between non-human and human derived dose estimates demonstrate the need for dosimetry studies to be performed in the species intended for study. This is further supported by marked differences in brain penetrance and metabolism of PET radioligands that are often observed when translating between species.

Optimization of the PET study protocol, including radiopharmaceutical administration, PET scan duration, and pre- and post-scanning micturition schedule, involves balancing imaging properties and quantification with participant safety. PET protocols need to be optimized in the context of use (e.g. serial, longitudinal and/or multi-tracer studies). Preliminary human studies combined with the human dosimetry findings presented in this work suggest that [^{18}F]nifene will provide a safe and effective biomarker for monitoring α4β2* nAChRs *in vivo* and allow for up to four 185 MBq [^{18}F]nifene scans annually in the U.S.A.

CHAPTER 5

DATA PROCESSING AND ANALYSIS PIPELINES FOR CLINICAL RESEARCH

5.1 Image Processing and Analysis of longitudinal MRI and [^{18}F]MK-6240, and [^{11}C]PiB PET

Neurodegenerative research studies have increasingly adopted neuroimaging using multiple PET radioligands and MRI sequences to investigate interactions between biomarkers and their biological inferences. These studies frequently involve acquisition of longitudinal imaging data that need to be reconstructed, processed, analyzed, and organized to facilitate investigation. This chapter describes a semi-automated pipeline developed in MATLAB (The MathWorks, Inc., Natick, MA) to process and analyze longitudinal, multimodal, multi-tracer PET and MRI data. In addition to this pipeline, the effects of attenuation correction methods on longitudinal DVR estimates are investigated using [^{11}C]PiB data acquired in two cycles 2-3 years apart.

5.1.1 Data Organization and Input Variables

The processing and analysis code were developed for a longitudinal study design that includes [^{11}C]PiB, [^{18}F]MK-6240, and T1-weighted MRI neuroimaging, but allows for the inclusion of additional radiotracers and MRI sequences. A schematic representation of the data structure is presented in Figure

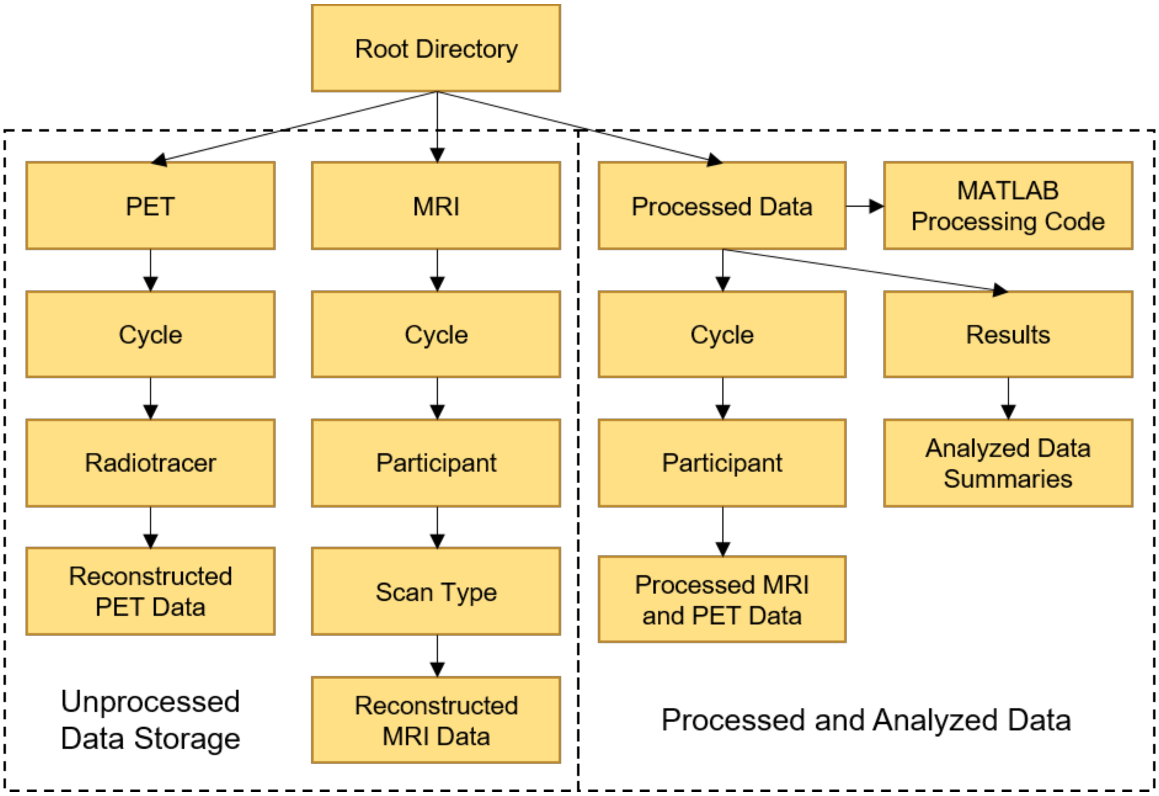

Figure 5.1 Data Structure for Neuroimaging Processing and Analysis Pipeline

5.1. Reconstructed PET and MRI data from the scanners are deposited into directories organized by modality, data cycle, and then radiotracer for PET, and sequence type for MRI. A front-end script with inputs for the participant ID, data cycle, and PET and MRI processing options is used for directory creation for individual subjects and cycles as needed, and manages calls to sub-functions containing processing and analysis sequences for MRI and PET data. Results from the analysis code are then saved in Microsoft Excel documents in a separate consolidated results directory. For a new participant with unprocessed data, the MRI processing sequence is called first, which produces data used for the autonomous PET processing sequences.

5.1.2 MRI Processing Sequence and ROI Delineation and Transformation

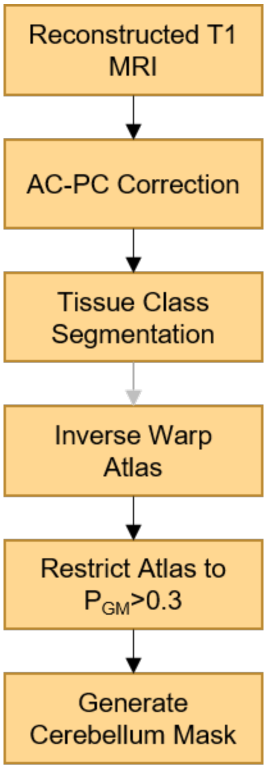

Figure 5.2 T1-Weighted MRI Processing Schematic

A schematic representation of the MRI processing sequence is shown in Figure 5.2. Reconstructed T1-weighted MRI images are first manually aligned along the anterior-posterior commissure (SPM12), and the origin of the NIFTI image is set to the anterior commissure. This is the only step in the processing pipeline that requires user intervention. The aligned data are resliced to 1mm isotropic resolution, and then corrected for magnetic field inhomogeneity during the tissue class segmentation process (GM, WM, and CSF) using the SPM12 segmentation function. The deformation fields describing the non-affine registration between MRI and MNI spaces defined during the tissue class segmentation are saved for warping atlases, MRI and PET between spaces. The deformation field is applied to the AAL atlas to define ROIs in native MRI space. To avoid deformations outside the brain from affecting ROIs, the AAL ROIs in MRI space are restricted to voxels with gray matter probabilities greater than 0.3. Finally, a composite of AAL cerebellum ROIs (ROIs 91-108 for PiB, and ROIs 93, 94, and 101-104 for MK-6240 and other tau tracers) is created to generate a reference region ROI used for parametric PET images. The binarized mask is then eroded to limit spill-in present in PET images from regions adjacent to the cerebellum by smoothing with an isotropic 8 mm Gaussian kernel (to simulate PET resolution) and keeping voxels within the smoothed mask greater than 0.7.

5.1.3 PET Image Processing and Analysis

PET data are processed using one of two sequences depending on the nature of the data acquisition. Both sequences require that the MRI sequence has already been performed since data from the MRI sequence are used to define the reference region for PET analysis.

Dynamic PET Processing and Analysis Sequence

The dynamic sequence (Figure 5.3) is used for generating DVR binding estimates. This sequence begins by converting ECAT 7.2 format PET data to the NIFTI format using code developed by Bradley Christian and Raymond Muzic and the NIFTI toolbox ("Tools for NifTi and ANALYZE image", Jimmy Shen, MathWorks File Exchange). The 4D NIFTI image is then smoothed with an isotropic 3mm Gaussian smoothing kernel and a summed image of all frames is generated for interframe realignment, which is performed using the SPM12 realignment function with a two-pass approach (see Appendix E for additional for interframe realignment of dynamic [^{18}F]MK-6240 data). After realignment, the PET time series is denoised using HYPR-LR (9mm Gaussian composite), which has been shown to nearly eliminate LGA noise dependent bias with [^{11}C]PiB while preserving spatial resolution (143, 144). A new summed image of the first ten minutes is then generated and is coregistered to the GM tissue probability map in MRI space using the SPM12 coregister function. The affine transformation matrix is then applied to the denoised 4D dataset to register the PET time series to the MRI space atlas.

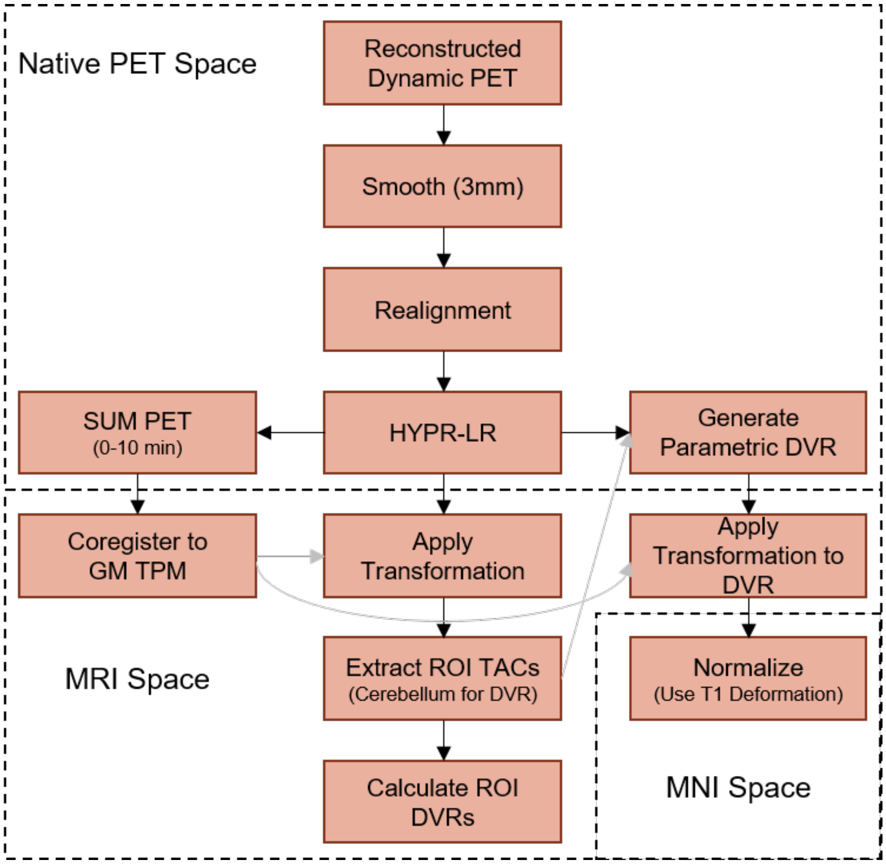

Figure 5.3 PET Processing Sequence for Dynamic PET Data

TACs are then extracted for all modified AAL ROIs for later analyses, and the cerebellum reference region ROI, which is then used to generate a parametric DVR image from the denoised PET time series in native PET space. The parametric DVR image is then registered to MRI space using the previously defined affine transformation matrix. The parametric image is then warped to standard MNI space by applying the deformation field defined in the T1 tissue class segmentation step of the MRI processing. Finally, ROI TACs are used to calculate regional DVRs for ROI-level analyses and ROI volumes are determined. TAC and data are saved within the participant's processed data hierarchy by cycle, and ROI volumes and regional DVRs are saved to a common Excel spreadsheet with individual sheets for each tracer and data cycle. Once TAC data are analyzed, intermediate PET image files are deleted, and the coregistered 4D PET file (>1Gb) can be optionally deleted.

Static PET Processing and Analysis Sequence

The static imaging sequence (Figure 5.4) is similar to the dynamic sequence with modifications made due to the limitations imposed by the lack of fully dynamic PET acquisition from bolus injection. This acquisition can still include multiple frames, but the processing pipeline assumes that all PET frames are used for the generation of parametric images. Therefore, this sequence relies on a larger spatial smoothing kernel for denoising since HYPR-LR would offer no additional benefit in this context. The sequence coregistration uses the entire T1-w MRI image for reference because early blood-flow information is not available in the PET data. Parametric SUVR images are generated after coregistration to MRI space by dividing the summed PET time series by the cerebellum ROI. The data extraction and analysis, normalization, and summary data organization are the same as those used in the dynamic PET sequence, with the exception that SUVRs are calculated in place of DVRs.

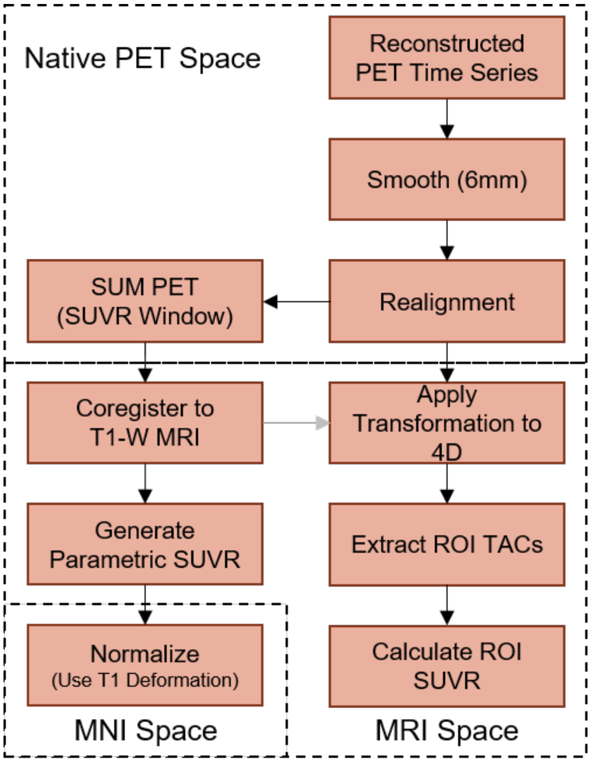

Figure 5.4 PET Processing Sequence for Static PET Data

5.2 Effects of PET Attenuation Correction on Longitudinal Binding Estimates

Once PET data are acquired, several corrections are applied during the image reconstruction process to ensure quantitative accuracy. These corrections account for differences in detector efficiencies (normalization), detection of random coincidences, scattered radiation, photon attenuation, and detector dead time, all of which affect the absolute quantitative accuracy of reconstructed PET images(191-197). The recent advent of hybrid PET/MR imaging systems has spurred new focus and development in accurate PET attenuation correction(198-201). This section examines the effect of PET attenuation correction (AC) methods and parameters of standalone PET systems on reference tissue based DVR estimates using longitudinally acquired [^{11}C]PiB PET neuroimaging data. These results are then discussed in the context of longitudinal study and inferences are extended to PET/MR systems.

5.2.1 PET Attenuation Correction Methods

AC in PET accounts for photon attenuation occurring along the paths of the coincident 511 keV annihilation gamma photons. In neuroimaging, attenuation mediums are largely soft tissue (i.e. brain) and bone (i.e. skull), which have PET (i.e. 511 keV) attenuation coefficients (μ) of 0.096 cm^{-1} and 0.172 cm^{-1}, respectively(202). Additionally, sinuses within the head can have μ values similar to those observed in the lungs (0.010-0.065 cm^{-1})(203).

Depending on the configuration of the tomograph (i.e. standalone PET, or hybrid PET/CT or PET/MR), different strategies are employed to directly measure or approximate attenuation correction factors (ACFs) used during image reconstruction. PET/CT systems directly measure attenuation (converted to Hounsfield units) of lower energy photons, which are subsequently converted to 511 keV attenuation coefficients(202). PET/MR systems cannot measure photon attenuation, and therefore generate parametric maps of attenuation coefficients (μ-maps) based on MR scans using either atlas-based and/or segmentation algorithms(198-201). Both CT- and MRI-derived μ-maps can then be forward projected to PET sinogram space to derive ACFs used for AC of PET data. Standalone PET systems can directly measure ACFs by acquiring transmission scans with and without (scans with medium referred to as a blank scans) the imaging medium/patient in the scanner using rotating rod sources containing long-lived 511-keV emitting isotope (e.g. ^{68}Ge)(204, 205). Additionally, standalone PET scanners can reconstruct measured

ACFs to generate μ-maps in image space, which can be further processed to reduce noise and potential bias that propagate to the final reconstructed image(s). One such algorithm employed by the ECAT HR+ tomograph uses a histogram of the measured μ-map attenuation coefficients to generate local thresholds defining attenuation mediums (e.g. bone, soft tissue, lung) present in the PET field of view(203, 206). Segmentation algorithms are particularly useful to minimize bias when activity is present in the field of view during the transmission scan, such as radiotracers that have a pre-scan uptake period. In this section, AC strategies and parameters are investigated to determine their impact on the variability of DVR binding estimates in longitudinally acquired [^{11}C]PiB PET data.

5.2.2 Methods

Participants and Data Acquisition

Two cycles of longitudinal [^{11}C]PiB data (2.16±0.29 years apart, mean±SD) from 17 PiB(-) individuals were included in this analysis (demographics in Table 5.1). [^{11}C]PiB was synthesized according to methods described in Chapter 3. For each data cycle, [^{11}C]PiB PET data were acquired on a Siemens ECAT HR+ tomograph in 3D mode. The PET scanning protocol began with a 6-minute transmission scan, followed by a 70-minute dynamic emission scan (5x2 min/fr,12x5 min/fr) beginning with a nominal 555 MBq [^{11}C]PiB bolus injection.

Group	*Mean ± SD Age, Range [yrs]*	*Sex*	*MMSE*
Cognitively Stable (n=13)	61 ± 5	11F,2M	29.5 ± 0.7
Cognitively Declining (n=4)	61 ± 2	3F, 1M	29.3 ± 0.8
Total (N=17)	61 ± 5, 55-73	14F, 3M	29.5 ± 0.8

Table 5.1 Attenuation Correction Comparison Participant Demographics

PET Image Reconstruction and Attenuation Correction Methods

Emission data were reconstructed using filtered backprojection with corrections applied for radioisotope decay, detector normalization, random events, attenuation and scatter (matrix size 128x128x63, voxel dimensions 2.57x2.57x2.43 mm, 4mm in-plane Gaussian Filter, brain mode on, axial filtering off, zoom=2). A single set of cycle one data was generated using segmented AC. For this data set, ACFs were generated by reconstructing the measured ACFs (9mm Gaussian smoothing, zoom=1, brain mode on, axial filtering and scatter correction=on) to generate a measured μ-map, which was segmented and subsequently forward projected to sinogram space.

Four sets of cycle two reconstructions were created to test for differences between measured and segmented AC and the effect of using different smoothing kernels (9mm or 6mm) during reconstruction of the measured μ-map used for μ-map segmentation. Emission scan reconstruction parameters were the same as cycle one, with the exception of the different AC approaches. The first set of reconstructions used 9mm smoothing in the measured μ-map reconstruction prior to μ-map segmentation (segmented 9mm). The second set (segmented 6mm) was produced similarly, but with a 6mm smoothing applied prior to segmentation. The third set (coregistered segmented cycle 1) used the cycle one μ-map, which was coregistered to the segmented 9mm cycle two μ-map. The final dataset (measured) reconstructed the measured ACFs using 9mm Gaussian smoothing (to reduce noise from measured ACFs), and was then forward projected to sinogram space without segmentation.

Post-Reconstruction Data Processing and Parametric Image Generation

Reconstructed cycle one emission data were interframe realigned, denoised (HYPR-LR), and coregistered to the cycle two T1-w MRI as described in the previous section. The cycle two MRI was used to avoid potential differences in the spatial alignment of the cerebellum reference region between cycles. The four cycle two reconstructed emission datasets were similarly processed, but used the same affine realignment and coregistration matrices defined by the cycle two segmented 9mm dataset. Cerebellum TACs were extracted from all coregistered PET data using the same cerebellar reference region ROI for all datasets. Parametric DVR images were generated (LGA, $t^*=35$ min, $k_2'=0.149$ min^{-1}) in native PET space and transformed to MRI space by applying the previously defined coregistration matrix. Coregistered parametric DVR images were subsequently warped into MNI space using the same deformation field for all DVR images within individual subjects defined from the tissue class segmentation of the T1-w MRI. DVRs were also determined from ROI extracted TACs using inverse-warped AAL ROIs restricted to $P_{GM}>0.3$ as described in section one of this chapter.

Inter-Method and Longitudinal Analyses

ROI analyses consisted of comparing TACs and DVR estimates regions affected by Aβ plaques. Regions were selected *a priori* based on previous analyses of [^{11}C]PiB data and the distribution of Aβ in neuropathology(16, 43, 207), and included in the analysis were the angular gyrus, anterior and posterior cingulate gyri, medial orbitofrontal gyrus, precuneus, supramarginal gyrus, and the middle and superior temporal gyri. In additional to individual ROIs, a global average of these ROIs was included in comparisons.

Inter-method comparisons were made using the cycle two datasets with the segmented 9mm dataset as the standard of comparison. The segmented 9mm dataset was used as the reference because this AC scheme was the same as the cycle one reconstructions and is the method used in the multi-site Alzheimer's Disease Neuroimaging Initiative (ADNI)(208). TACs for each cycle two dataset relative to the segmented 9mm method were averaged across all 17 subjects and compared in the cerebellum and the global average of the ROIs. Additionally, the average (across subject) of the ratio of the global mean to the cerebellum TACs was compared across the four cycle two datasets. ROI and global DVR estimates were compared using Bland Altman plots. Spatial differences between AC methods were assessed by averaging parametric DVR images in normalized space for each method and dividing by the average DVR image from the segmented 9mm dataset.

Comparisons between cycle one and cycle two DVRs were performed in two ways. The first comparison examined the absolute difference relative to the cycle one scan, similar to a test-retest measure $\left(\frac{DVR_2-DVR_1}{DVR_1}\times 100\right)$, at the ROI level. Additionally, longitudinal DVR rates of change (%DVR/yr) from cycle one to cycle two were calculated as a percentage of the cycle one scan $\left(\frac{DVR_2-DVR_1}{DVR_1\times(t_2-t_1)}\times 100\right)$ at the ROI level and by generating parametric images. For all comparisons, data are reported as the mean ± standard error taken across the 17 subjects. Similarly, parametric images were averaged across all subjects.

5.2.3 Results

Inter-Method Comparisons Using Cycle Two Data

TACs comparing cycle two reconstructions using segmented 6mm, measured, and coregistered cycle one AC methods were slightly higher than the segmented 9mm reconstructions in both the cerebellum and the global average for the segmented 6mm and coregistered cycle one methods (Figure 5.5). The measured AC method produced reconstructed activity concentrations that were ~12% higher in the cerebellum, and ~10% higher in the global average. These relationships were mostly consistent throughout the entire 70-minute PET scan duration. TACs normalized to the cerebellum within each method indicated minimal differences between methods with the exception of the

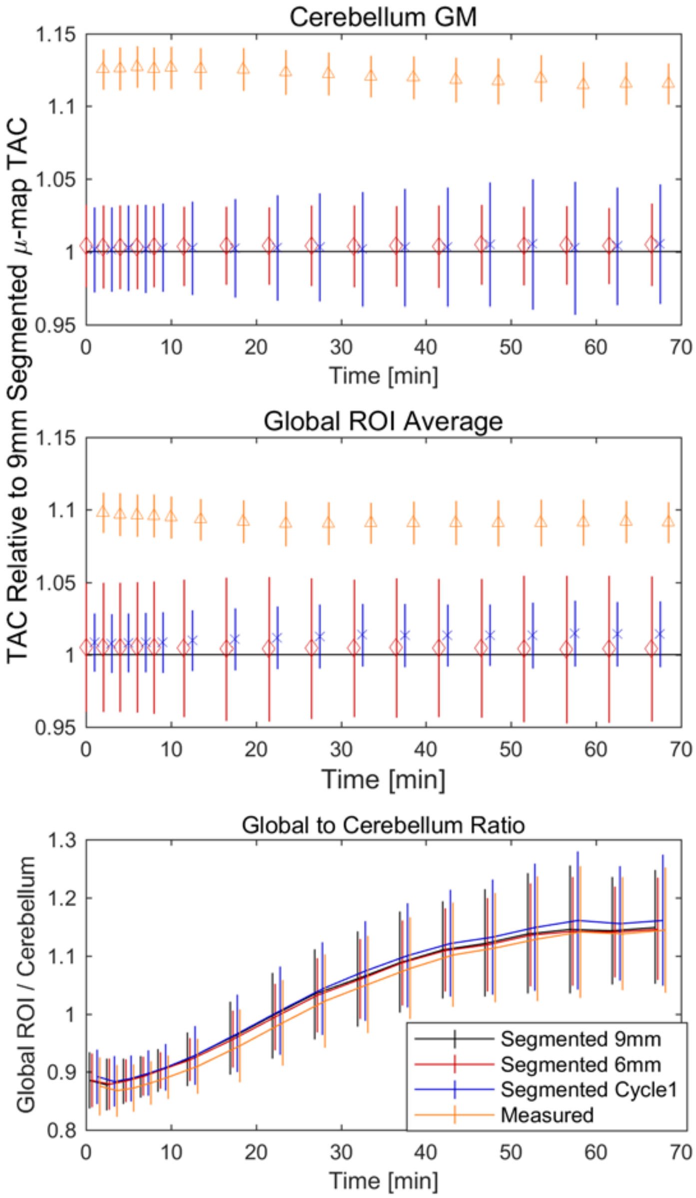

Figure 5.5 [11C]PiB TAC Comparisons Between Attenuation Correction Methods

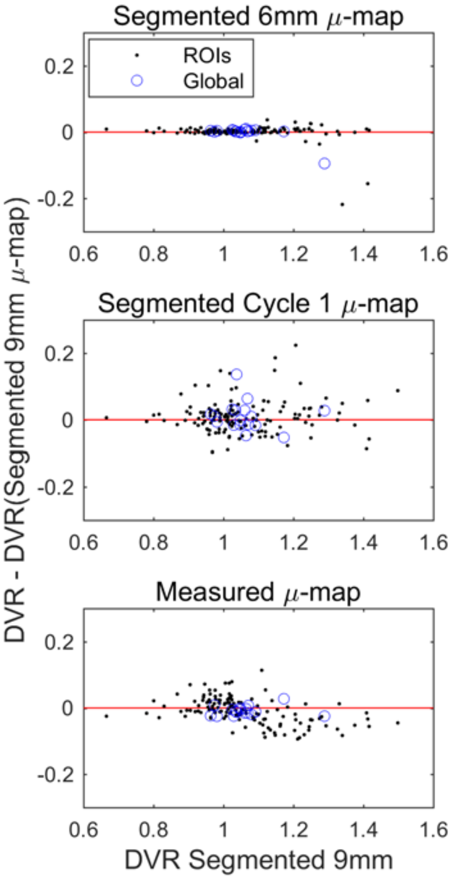

Figure 5.6 [11C]PiB DVR Comparisons Between Attenuation Correction Methods

measured AC correction that had slightly lower values prior to 60 minutes post-injection.

DVR comparisons between AC methods at the ROI and global levels indicated the highest agreement between the segmented 9mm and segmented 6mm methods (Figure 5.6). Using the coregistered cycle one or measured µ-maps for AC showed increased variability in DVR estimates and a marked reduction in DVR for the measured method in ROIs for DVR>1.1 when compared to the segmented 9mm method.

Parametric DVR image comparisons (Figure 5.7) indicated spatially dependent patterns of over and underestimation for the measured and coregistered cycle one AC methods, and a slight overall

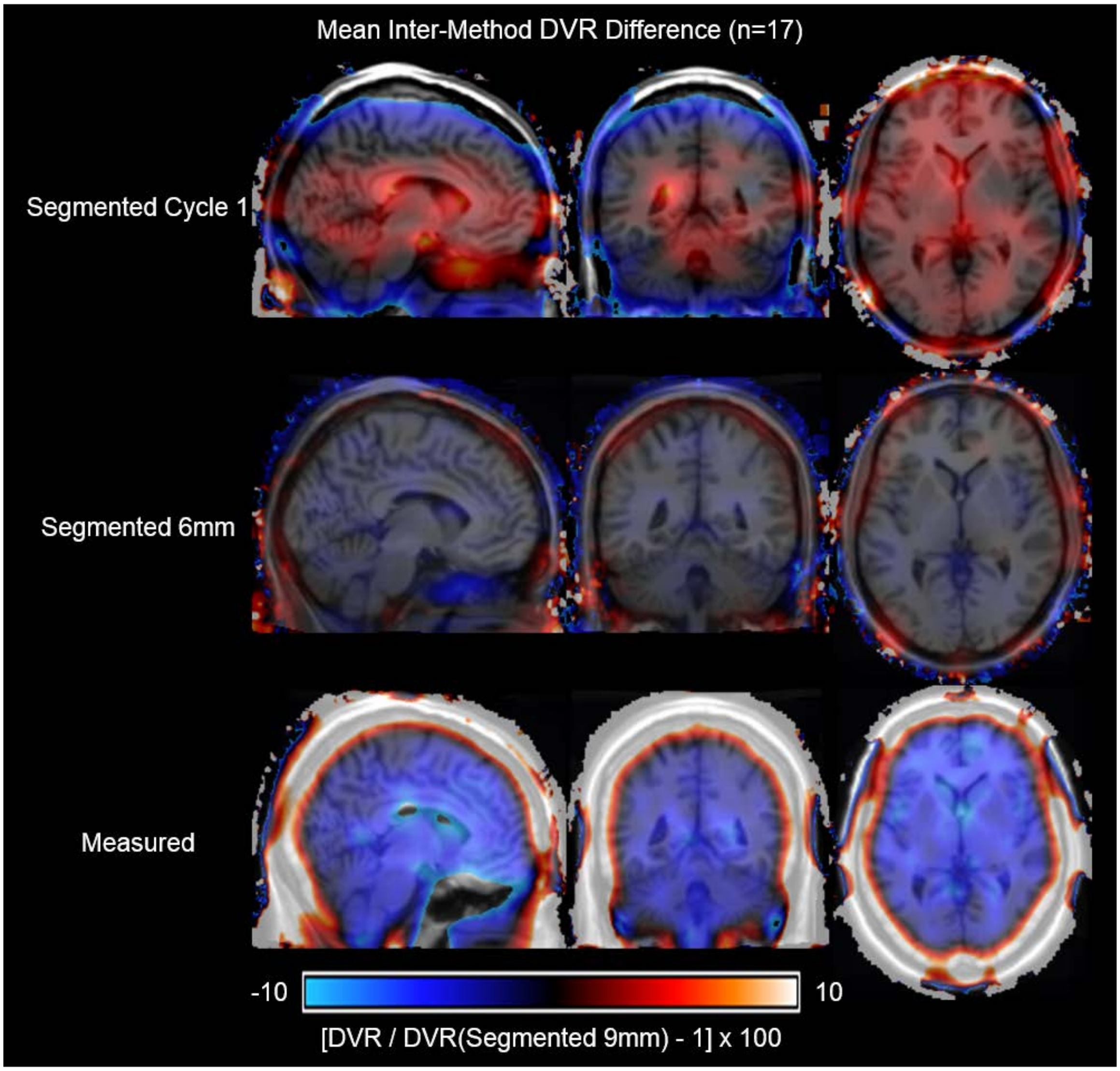

Figure 5.7 Parametric [^{11}C]PiB DVR Comparisons Using Different Attenuation Correction Methods

negative difference for the segmented 6mm method relative to the segmented 9mm method. The coregistered cycle one method indicated a banded pattern present in sagittal and coronal slices where DVR values in the superior and inferior portions of the PET image were lower with a central band between these regions that was higher than the segmented 9mm data. The greatest differences in parametric DVR images were observed using the measured AC approach, where values corresponding to the skull were >10% higher, and values in the center of the brain were ~10% lower than the segmented 9mm DVR images.

Comparisons of Longitudinal [^{11}C]PiB DVR

The absolute difference between cycle one and two DVRs varied by region and ranged from 3-9% (Figure 5.8). Inter-subject standard errors ranged by ROI and were generally comparable between AC methods, but were slightly lower for cycle two data reconstructed using the coregistered cycle one µ-map and highest for cycle two data reconstructed using the measured AC method.

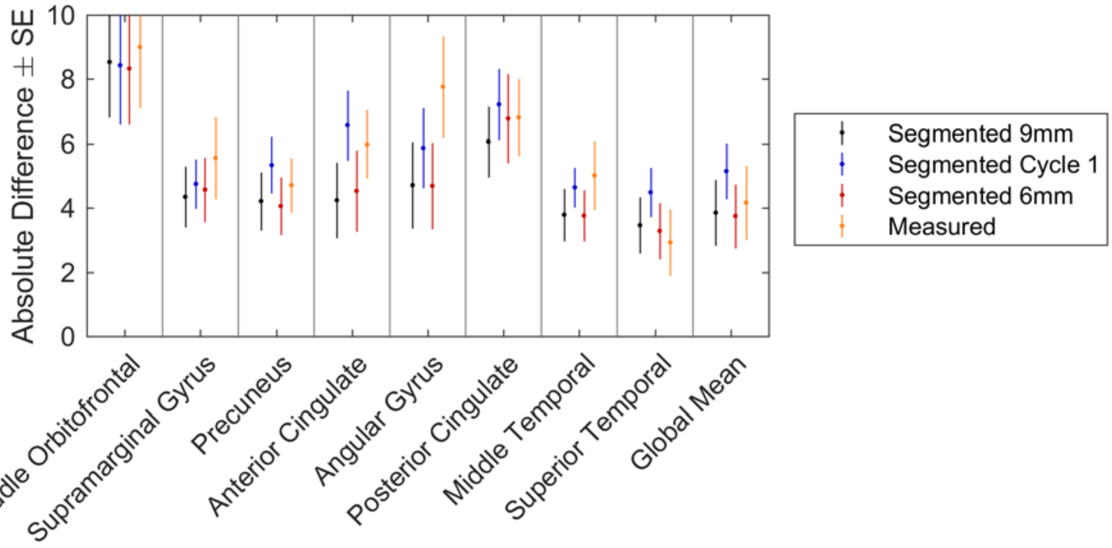

Figure 5.8 [^{11}C]PiB DVR Absolute Difference Between Cycles

Longitudinal rates of [^{11}C]PiB DVR change calculated for individual ROIs were similar for most regions and methods with the exception of the measured AC method where %DVR/yr measures indicated region-specific differences compared to other methods, particularly in the anterior cingulate which was >6 %DVR/yr lower compared to other AC methods (Figure 5.9). Rates of %DVR/yr were most consistent between the segmented 9mm and segmented 6mm AC methods with less than one %DVR/yr difference within individual ROIs. Rates calculated using the coregistered cycle one µ-map method were higher than the segmented 9mm and segmented 6mm methods in the anterior and posterior cingulate and the middle

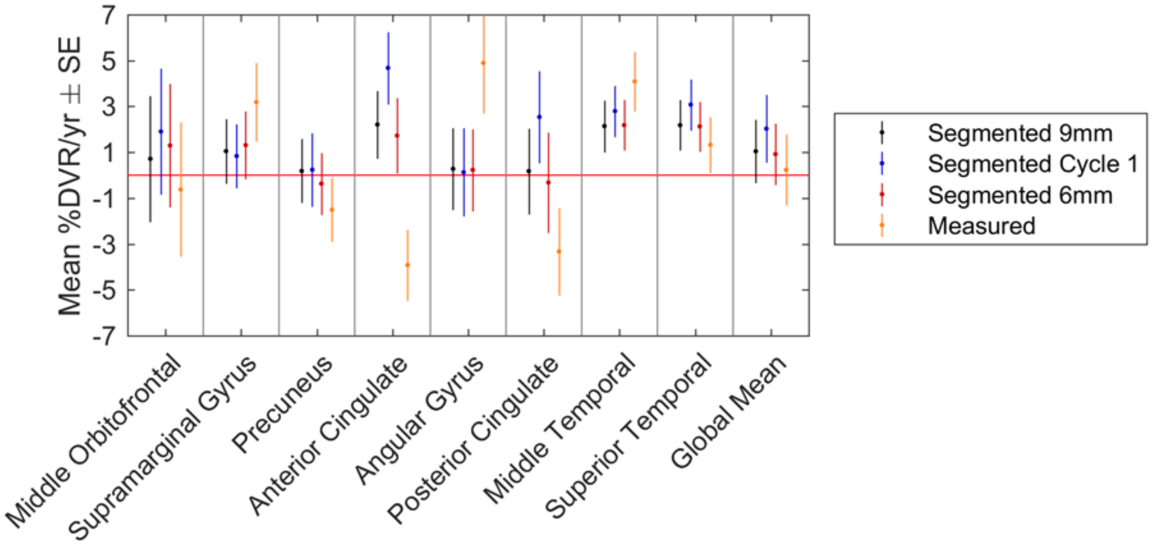

Figure 5.9 [^{11}C]PiB DVR Rate of Change Comparison of Attenuation Correction Methods

orbitofrontal gyrus and slightly higher in the middle and superior temporal cortices. Inter-subject variability in annual DVR rates within individual regions were similar for all AC methods. [^{11}C]PiB DVR rates calculated from the global average of the ROIs were within 2 %DVR/yr for all AC methods. Global measures were most similar between the segmented 9mm and segmented 6mm AC methods.

Mean longitudinal DVR rate parametric images were visually indistinguishable between the segmented 9mm and segmented 6mm AC methods (Figure 5.10). Coregistered segmented cycle one and measured AC methods resulted in %DVR/yr parametric maps that exhibited similar spatial patterns as those observed in the inter-method comparisons. Notably, all AC methods indicated a reduction in DVR from cycle one to cycle two in the lateral ventricles, which ranged from -3 to -8 %DVR/yr and had the highest magnitude using the measured AC method for the cycle two reconstruction.

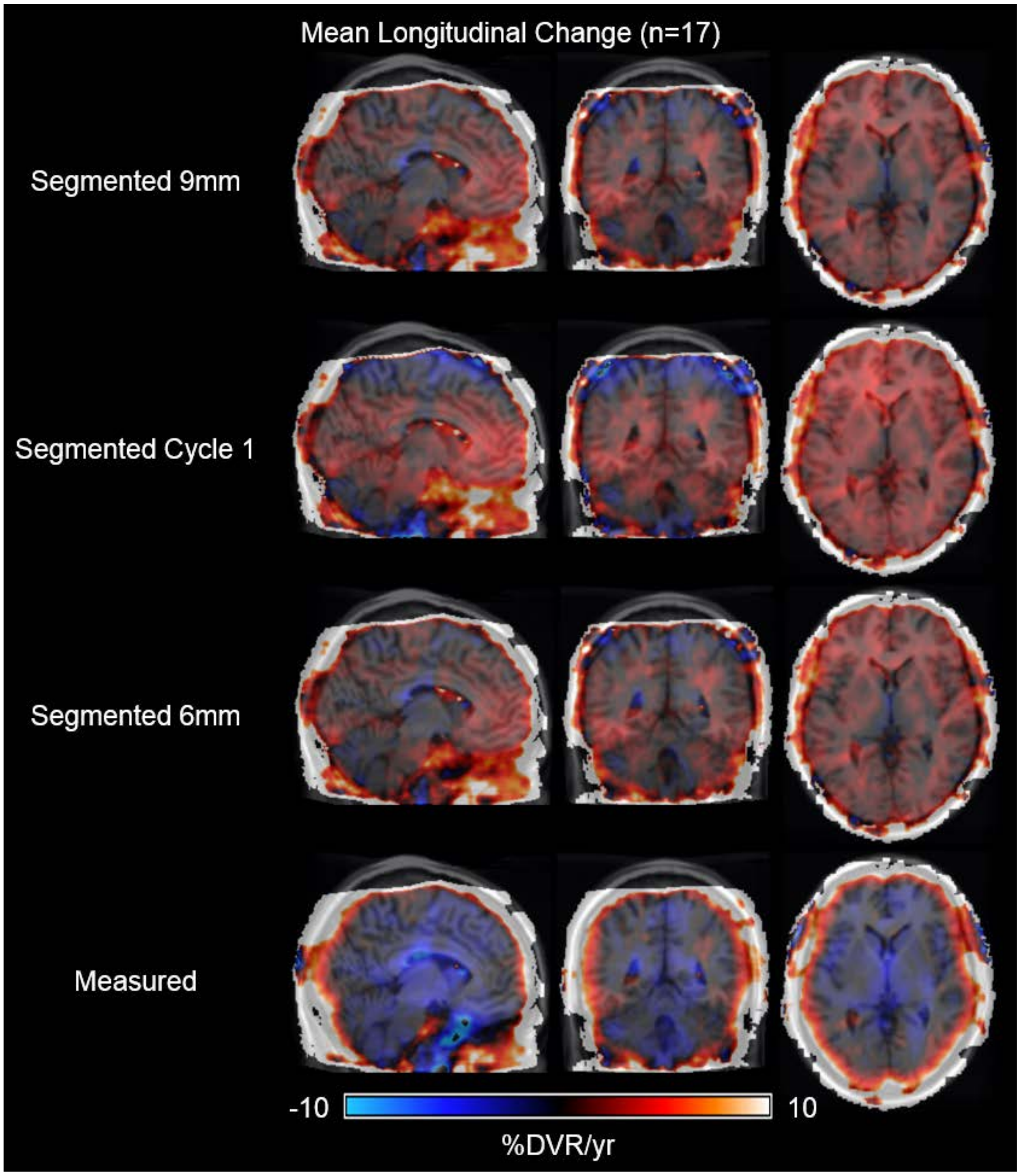

Figure 5.10 [^{11}C]PiB Annual Rates of Change Using Different Attenuation Correction Methods

5.2.4 Discussion

The spatial differences between AC methods can be explained when considering the process of μ-map generation for each method. Although differences in the pre-segmentation smoothing could affect the histogram-based segmentation thresholds, the final segmented image is generated by combining the segmented and measured μ-maps using a weighted approach and is subsequently smoothed using a proprietary (unknown) smoothing kernel(203). This final smoothing step likely blurs local differences, which therefore minimizes differences between reconstructed images that use different pre-segmentation smoothing kernels. Differences between DVR images using segmented and measured AC can be explained by partial volume effects in bone attenuation coefficients and the differences in the path length of bone in the cerebellum and the cerebrum. Attenuation coefficients in boney regions were higher for the measured AC method compared to segmented AC (data not shown), which is likely due to partial volume effects and exacerbated by smoothing of the final composite image for segmented AC. Higher attenuation coefficients result in higher reconstructed image activity concentrations throughout the brain, but more so in the cerebellum where in-plane path lengths through bone are greater. Higher cerebellum TACs therefore reduce the DVR values in the cerebrum compared to DVR images generated from reconstructions using segmented AC. The banded pattern observed using the coregistered segmented cycle one μ-map may have been produced due to missing attenuation information in the superior and inferior edges of the PET field of view, which would also affect scatter correction of these slices and the scatter factors within individual frames. There is also potential for registration bias occurring from the coregistration of the cycle one and two μ-maps.

Reduced variability in repeated PET scans increases the statistical power to detect longitudinal changes. Therefore, it would seem that using a single μ-map for individual subjects, compared to using unique μ-maps from each PET acquisition cycle, would reduce longitudinal variability in DVR estimates. However, this was not the case in this data where using unique μ-maps with similar or the same parameters (6mm or 9mm pre-segmentation smoothing) indicated lower absolute differences between scans, which were comparable to test-retest measures of [^{11}C]PiB LGA DVRs reported for AD and cognitively normal older individuals(64, 209). Global rates of DVR change were lower in this study than PiB binding measures in cognitively normal individuals reported in other studies that included both PiB(-) and PiB(+) individuals (71, 210), and just PiB(-) individuals(211). The similarities between test-retest measures of other studies and low rates of annual DVR change suggest that despite the 2-3 year gap between scans, there were minimal physiological differences in Aβ between cycle one and cycle two PET scans. This supports the use of this sample for comparisons of different AC methods. When considering spatial patterns that likely represent bias between methods, it is advisable to use the same AC method for cycle one and cycle two with individually derived μ-maps. Interestingly, despite differences between AC methods in PET activity concentrations, the use of a reference tissue method largely diminished differences in binding estimates between AC methods supporting the use of simplified methods to reduce variability between scans.

PET/MR systems pose a unique challenge for absolute quantification of PET data, largely due to the inability to measure photon attenuation and adequately correct for this physical process. While several strategies have been proposed in neuroimaging, these mostly rely on non-linear deformations of atlases and/or probability maps to the subject-specific MR images acquired during the PET scan session(198, 199, 201, 212, 213). Evaluation of these methods is further complicated because common PET brain phantoms(214) do not have materials with magnetic moments comparable to those of tissues present throughout the head and are not spatially similar to the 3D anatomy of the entire human head, which would be required for quality spatially registration of PET/MR based AC methods. Therefore, evaluation of PET/MR AC methods often relies on registration of CT images (or other attenuation images) to the space of the PET/MR system. These coregistered images are then used for AC of PET data and the resulting reconstructed images define the standard of comparison for evaluating MR-based methods. The results presented in this section using intramodality coregistered μ-maps suggest that even when using AC information derived from the same individual, the process of registration potentially creates spatially dependent biases in the reconstructed PET data. This suggests that intermodal registration of CT or other data to MRI could affect the quantitative accuracy of the comparison standard in these studies. This could potentially be mitigated by introducing a removable, MR-safe transmission source that could serve as a standard of comparison without concern of registration biases (patient motion notwithstanding). This would be especially adaptable to neuroimaging research applications where spatial constraints would be less limiting compared to whole-body imaging.

This investigation has limitations that warrant further discussion. Foremost, test-retest data or PET scans where two transmission scans were acquired for a single emission scan would have provided a more direct comparison of the variability introduced by methodological differences in the generation of ACFs and the transmission scan itself. In lieu of these data, longitudinal [^{11}C]PiB data in PiB(-) subjects was used with the assumption that these individuals would not have dramatically different DVR outcomes as a result of minimal changes in Aβ deposition or brain morphology occurring between scans (2-3 years). In this regard, parametric image comparisons between longitudinal time points indicated a reduction in PET signal in the ventricle space for all methods, which could be indicative of atrophy occurring between data cycles. This would add additional variability and bias, including partial volume effects, when evaluating difference between methods. However, since the same spatial transformation were applied and the cycle one reconstruction was used for comparison for all methods, differences between AC method variability and potential biases would be a reflection of how individual methods are affected by atrophic processes or accumulation of Aβ. As such, these comparisons may represent a more accurate depiction of the effects of AC methodology on longitudinal DVR measures. An additional limitation is only one AC method was used for the cycle one data. It is therefore unsurprising that the same method (segmented 9mm) produced the optimal results compared to other methods. A better understanding of how each AC method would contribute to longitudinal variability could be ascertained by investigating within-method differences from cycle one and cycle two reconstructions or serially acquired transmission scans for the same emission scan, but these data were not available for this analysis.

5.3 Summary and Conclusions

This chapter highlights the multi-step processes required to analyze PET neuroimaging data and how individual steps can affect PET outcome measures in longitudinal studies. These results also demonstrate the need for routine quality control of processed PET data to minimize potential sources of additional variability that could preclude detection of small changes between longitudinal time points. Further work is needed to integrate quality control measures into the processing and analysis pipeline described in this chapter. Additionally, there is a need to develop semi- or fully-automated QC algorithms in large-scale, multi-center studies where data are acquired rapidly and timely feedback is needed to address potential resolvable issues to maximize the efficient use of acquired research data.

CHAPTER 6

SUMMARY CONCLUSION AND FUTURE DIRECTIONS

Advances in medical science technology and methodology continue to drive discovery of new insights into neurodegenerative disease processes and have tremendous potential for tying together molecular features of disease with macromolecular processes and disease symptomology. This theme is evident in several aspects of this work and in the state of neurodegenerative disease research. The recent discovery of NFT-specific PET radioligands holds tremendous potential for novel discovery of disease mechanisms, defining individual pathophysiological processes and the interactions between them, and informing diagnosis and assessing patient risk during life. This represents a major development more than a century after AD pathological features were first identified. Beyond NFT PET imaging, recent advances in molecular imaging techniques (i.e. cryo-EM) hold unprecedented potential for identifying molecular structures of protein aggregates and have predictive potential for designing aggregate-specific radiopharmaceuticals and therapeutic drugs. This likely will be especially important for developing PET biomarkers for other amyloids (e.g. alpha synuclein, TDP-43, Huntington, etc.) or soluble forms of aggregates, such as Aβ and tau oligomers, that currently have limited or no available *in vivo* biomarkers.

The development of novel radioligands for proteinopathies continues to be stifled by several factors. Discrepancies between *in vitro* binding assays themselves, and between *in vitro* and *in vivo* results highlight the need for in-depth methodological development to understand the limitations of using *in vitro* binding assays to evaluate *in vivo* radiotracer binding patterns. This is evidenced with the THK series of compounds where methodological differences in autoradiographic tissue preparation resulted in completely different binding affinities for MAO-B, and differences between the present work and other studies that have made contradictory conclusions about the binding specificity of THK-5317. Given the availability of more NFT-specific radioligands, *in vivo* binding similarities between [^{18}F]THK-5351 and [^{18}F]THK-5317, and the discord between these ligands and [^{18}F]MK-6240 continued use of THK compounds for detecting NFT pathophysiology is not advisable. Non-human primates may be useful for identifying off-target binding sites *in vivo* as demonstrated with the development of MK-6240. However, the lack of non-human primate models for AD and the lack of phylogenetic similarities between rodents and humans, continue to suppress the development and characterization of effective therapies and radioligands for humans. Development of non-human primate models that express human-like pathophysiology would be particularly advantageous for evaluating ligand specificity and kinetic properties of PET compounds due to the potential for longer, uninterrupted scan durations and the ability to perform self-blocking studies that could identify the *in vivo* affinity and components of the distribution volume prior to expensive human translation efforts.

Neurodegenerative disease research has become a large-scale, multi-site collaborative effort that requires refined automated processes to facilitate investigation and new discoveries. The work presented in this dissertation highlights the need for streamlining individual processes from radiopharmaceutical production to image processing and analysis of PET data to maximize the efficient use of available resources. While this work provides a template for this development process, further work is needed. [^{18}F]MK-6240 indicated high dynamic range, favorable imaging characteristics, and high apparent selectivity to NFTs, but its use in clinical research may be stunted by low radiochemical yields that limit large-scale distribution. Additional investigation is therefore warranted to improve radiochemical yields thereby increasing the accessibility of this radiotracer for clinical investigations. Test-retest studies of [^{18}F]MK-6240 and other NFT PET radioligands are also needed to optimize imaging protocols and processing and quantification methodology to better understand and possibly reduce inter-scan variability. These studies would help contextualize longitudinal findings and have potential to improve statistical efficiency for detecting differences within individual subjects and between clinical groups. In addition, the development and implementation of automated or semi-automated quality control algorithms that incorporate longitudinal data would also be advantageous.

Lastly, continued work characterizing AD biomarkers throughout the entire range of disease is needed to allow for meaningful interpretation of results at the patient level. A better understanding of how AD biomarkers predict late-life cognitive and disease-specific outcomes would provide a scaffold to develop risk profiles similar to those used in other clinical diseases (e.g. blood markers for cardiovascular disease or diabetes). This would have the immediate effect of improving late-life planning for individuals with high risk of developing dementia. In the context of clinical trials, a better understanding of biomarker-based AD risk could facilitate the integration of AD biomarkers as screening criteria and as clinical outcome measures, which would enable faster development of much needed disease modifying therapies. Improved neuroimaging methodology and biomarker models are also needed to take advantage of the topographical patterns of aggregate-specific PET radioligands, which likely will provide meaningful diagnostic information from a single time point. Many of these concepts are already being explored in clinical research, but substantial work is also needed to obtain regulatory approval so biomarkers can be integrated into clinical use. Despite these obstacles and other unknown challenges that may lie ahead, advances in PET imaging allow, for the first time in history, topographical detection and monitoring of the hallmarks of AD pathophysiology during life. This will undoubtedly play a pivotal role in the advancement of scientific and medical knowledge of AD processes and move us towards a solution to a disease that is currently without a means of intervention.

BIBLIOGRAPHY

1. Aging NIo. Alzheimer's Disease Fact Sheet 2018 [cited 2018 March 5]. Available from: www.nia.nih.gov/health/alzheimers-disease-fact-sheet.
2. Association As. Costs of Alzheimer's to Medicare and Medicaid. In: Association As, editor. 2017. p. 1-2.
3. Hyman BT, Sorger P. Failure analysis of clinical trials to test the amyloid hypothesis. Annals of neurology. 2014;76(2):159-61. doi: 10.1002/ana.24227.
4. Declercq LD, Vandenberghe R, Van Laere K, Verbruggen A, Bormans G. Drug Development in Alzheimer's Disease: The Contribution of PET and SPECT. Front Pharmacol. 2016;7:88. doi: 10.3389/fphar.2016.00088. PubMed PMID: 27065872; PMCID: PMC4814730.
5. Hyman BT, Phelps CH, Beach TG, Bigio EH, Cairns NJ, Carrillo MC, Dickson DW, Duyckaerts C, Frosch MP, Masliah E. National Institute on Aging–Alzheimer's Association guidelines for the neuropathologic assessment of Alzheimer's disease. Alzheimer's & Dementia. 2012;8(1):1-13. doi: doi:10.1016/j.jalz.2011.10.007.
6. Montine TJ, Phelps CH, Beach TG, Bigio EH, Cairns NJ, Dickson DW, Duyckaerts C, Frosch MP, Masliah E, Mirra SS. National Institute on Aging–Alzheimer's Association guidelines for the neuropathologic assessment of Alzheimer's disease: a practical approach. Acta neuropathologica. 2012;123(1):1-11. doi: 10.1007/s00401-011-0910-3.
7. Mirra SS, Heyman A, McKeel D, Sumi SM, Crain BJ, Brownlee LM, Vogel FS, Hughes JP, Belle Gv, Berg L. The Consortium to Establish a Registry for Alzheimer's Disease (CERAD): Part II. Standardization of the neuropathologic assessment of Alzheimer's disease. Neurology. 1991;41(4):479-. doi: 10.1212/wnl.41.4.479.
8. McKhann GM, Knopman DS, Chertkow H, Hyman BT, Jack CR, Jr., Kawas CH, Klunk WE, Koroshetz WJ, Manly JJ, Mayeux R, Mohs RC, Morris JC, Rossor MN, Scheltens P, Carrillo MC, Thies B, Weintraub S, Phelps CH. The diagnosis of dementia due to Alzheimer's disease: recommendations from the National Institute on Aging-Alzheimer's Association workgroups on diagnostic guidelines for Alzheimer's disease. Alzheimers Dement. 2011;7(3):263-9. doi: 10.1016/j.jalz.2011.03.005. PubMed PMID: 21514250; PMCID: PMC3312024.
9. Beach TG, Monsell SE, Phillips LE, Kukull W. Accuracy of the clinical diagnosis of Alzheimer disease at National Institute on Aging Alzheimer Disease Centers, 2005-2010. J Neuropathol Exp Neurol. 2012;71(4):266-73. doi: 10.1097/NEN.0b013e31824b211b. PubMed PMID: 22437338; PMCID: PMC3331862.
10. Albert MS, DeKosky ST, Dickson D, Dubois B, Feldman HH, Fox NC, Gamst A, Holtzman DM, Jagust WJ, Petersen RC, Snyder PJ, Carrillo MC, Thies B, Phelps CH. The diagnosis of mild cognitive impairment due to Alzheimer's disease: recommendations from the National Institute on Aging-Alzheimer's Association workgroups on diagnostic guidelines for Alzheimer's disease. Alzheimers Dement. 2011;7(3):270-9. doi: 10.1016/j.jalz.2011.03.008. PubMed PMID: 21514249; PMCID: PMC3312027.
11. Dubois B, Feldman HH, Jacova C, DeKosky ST, Barberger-Gateau P, Cummings J, Delacourte A, Galasko D, Gauthier S, Jicha G, Meguro K, O'Brien J, Pasquier F, Robert P, Rossor M, Salloway S, Stern Y, Visser PJ, Scheltens P. Research criteria for the diagnosis of Alzheimer's disease: revising the NINCDS–ADRDA criteria. The Lancet Neurology. 2007;6(8):734-46. doi: 10.1016/s1474-4422(07)70178-3.
12. Dubois B, Feldman HH, Jacova C, Hampel H, Molinuevo JL, Blennow K, DeKosky ST, Gauthier S, Selkoe D, Bateman R, Cappa S, Crutch S, Engelborghs S, Frisoni GB, Fox NC, Galasko D, Habert M-O, Jicha GA, Nordberg A, Pasquier F, Rabinovici G, Robert P, Rowe C, Salloway S, Sarazin M, Epelbaum S, de Souza LC, Vellas B, Visser PJ, Schneider L, Stern Y, Scheltens P, Cummings JL. Advancing research diagnostic criteria for Alzheimer's disease: the IWG-2 criteria. The Lancet Neurology. 2014;13(6):614-29. doi: 10.1016/s1474-4422(14)70090-0.
13. Jack CR, Jr., Albert MS, Knopman DS, McKhann GM, Sperling RA, Carrillo MC, Thies B, Phelps CH. Introduction to the recommendations from the National Institute on Aging-Alzheimer's Association workgroups on diagnostic guidelines for Alzheimer's disease. Alzheimers Dement. 2011;7(3):257-62. doi: 10.1016/j.jalz.2011.03.004. PubMed PMID: 21514247; PMCID: PMC3096735.
14. Sperling RA, Aisen PS, Beckett LA, Bennett DA, Craft S, Fagan AM, Iwatsubo T, Jack CR, Jr., Kaye J, Montine TJ, Park DC, Reiman EM, Rowe CC, Siemers E, Stern Y, Yaffe K, Carrillo MC, Thies B, Morrison-Bogorad M, Wagster MV, Phelps CH. Toward defining the preclinical stages of Alzheimer's disease: recommendations from the National Institute on Aging-Alzheimer's Association workgroups on

diagnostic guidelines for Alzheimer's disease. Alzheimers Dement. 2011;7(3):280-92. doi: 10.1016/j.jalz.2011.03.003. PubMed PMID: 21514248; PMCID: PMC3220946.

15. Braak H, Braak E. Neuropathological stageing of Alzheimer-related changes. Acta Neuropathol. 1991;82(4):239-59. doi: 10.1007/BF00308809.

16. Thal DR, Rüb U, Orantes M, Braak H. Phases of Aβ-deposition in the human brain and its relevance for the development of AD. Neurology. 2002;58(12):1791-800. doi: 10.1212/WNL.58.12.1791; PMCID: 12084879.

17. Nelson PT, Alafuzoff I, Bigio EH, Bouras C, Braak H, Cairns NJ, Castellani RJ, Crain BJ, Davies P, Del Tredici K, Duyckaerts C, Frosch MP, Haroutunian V, Hof PR, Hulette CM, Hyman BT, Iwatsubo T, Jellinger KA, Jicha GA, Kovari E, Kukull WA, Leverenz JB, Love S, Mackenzie IR, Mann DM, Masliah E, McKee AC, Montine TJ, Morris JC, Schneider JA, Sonnen JA, Thal DR, Trojanowski JQ, Troncoso JC, Wisniewski T, Woltjer RL, Beach TG. Correlation of Alzheimer disease neuropathologic changes with cognitive status: a review of the literature. J Neuropathol Exp Neurol. 2012;71(5):362-81. doi: 10.1097/NEN.0b013e31825018f7. PubMed PMID: 22487856; PMCID: PMC3560290.

18. Nelson PT, Jicha GA, Schmitt FA, Liu H, Davis DG, Mendiondo MS, Abner EL, Markesbery WR. Clinicopathologic correlations in a large Alzheimer disease center autopsy cohort: neuritic plaques and neurofibrillary tangles "do count" when staging disease severity. J Neuropathol Exp Neurol. 2007;66(12):1136-46. doi: 10.1097/nen.0b013e31815c5efb. PubMed PMID: 18090922; PMCID: PMC3034246.

19. Alzheimer A, Stelzmann RA, Schnitzlein HN, Murtagh FR. An English translation of Alzheimer's 1907 paper, "Uber eine eigenartige Erkankung der Hirnrinde". Clin Anat. 1995;8(6):429-31. doi: 10.1002/ca.980080612. PubMed PMID: 8713166.

20. Braak H, Alafuzoff I, Arzberger T, Kretzschmar H, Del Tredici K. Staging of Alzheimer disease-associated neurofibrillary pathology using paraffin sections and immunocytochemistry. Acta Neuropathol. 2006;112(4):389-404. doi: 10.1007/s00401-006-0127-z. PubMed PMID: 16906426; PMCID: PMC3906709.

21. Braak H, Del Tredici K. The preclinical phase of the pathological process underlying sporadic Alzheimer’s disease. Brain. 2015;138(10):2814-33. doi: 10.1093/brain/awv236.

22. Braak H, Thal DR, Ghebremedhin E, Del Tredici K. Stages of the pathologic process in Alzheimer disease: age categories from 1 to 100 years. J Neuropathol Exp Neurol. 2011;70(11):960-9. doi: 10.1097/NEN.0b013e318232a379. PubMed PMID: 22002422.

23. Thal DR, Fandrich M. Protein aggregation in Alzheimer's disease: Abeta and tau and their potential roles in the pathogenesis of AD. Acta Neuropathol. 2015;129(2):163-5. doi: 10.1007/s00401-015-1387-2. PubMed PMID: 25600324.

24. Friedhoff P, von Bergen M, Mandelkow E-M, Mandelkow E. Structure of tau protein and assembly into paired helical filaments. Biochimica et Biophysica Acta (BBA)-Molecular Basis of Disease. 2000;1502(1):122-32. doi: 10.1016/S0925-4439(00)00038-7.

25. Weaver CL, Espinoza M, Kress Y, Davies P. Conformational change as one of the earliest alterations of tau in Alzheimer’s disease. Neurobiology of aging. 2000;21(5):719-27. doi: 10.1016/S0197-4580(00)00157-3.

26. Bancher C, Brunner C, Lassmann H, Budka H, Jellinger K, Wiche G, Seitelberger F, Grundke-Iqbal I, Iqbal K, Wisniewski HM. Accumulation of abnormally phosphorylated τ precedes the formation of neurofibrillary tangles in Alzheimer's disease. Brain Research. 1989;477(1-2):90-9. doi: 10.1016/0006-8993(89)91396-6.

27. Nisbet RM, Polanco JC, Ittner LM, Gotz J. Tau aggregation and its interplay with amyloid-beta. Acta Neuropathol. 2015;129(2):207-20. doi: 10.1007/s00401-014-1371-2. PubMed PMID: 25492702; PMCID: PMC4305093.

28. Honjo K, Black SE, Verhoeff NP. Alzheimer's disease, cerebrovascular disease, and the β-amyloid cascade. The Canadian Journal of Neurological Sciences. 2012;39(06):712-28. doi: 10.1017/S0317167100015547.

29. Hardy JA, Higgins GA. Alzheimer's disease: the amyloid cascade hypothesis. Science. 1992;256(5054):184.

30. Mattson MP. Pathways towards and away from Alzheimer's disease. Nature. 2004;430(7000):631-9. doi: 10.1038/nature02621.

31. Markesbery WR. Oxidative Stress Hypothesis in Alzheimer's Disease. Free Radical Biology and Medicine. 1997;23(1):134-47. doi: 10.1016/s0891-5849(96)00629-6.

32. Braak H, Del Tredici K. The preclinical phase of the pathological process underlying sporadic Alzheimer's disease. Brain. 2015;138(Pt 10):2814-33. doi: 10.1093/brain/awv236. PubMed PMID: 26283673.
33. Selkoe DJ. Toward a Comprehensive Theory for Alzheimer's Disease. Hypothesis: Alzheimer's Disease Is Caused by the Cerebral Accumulation and Cytotoxicity of Amyloid β-Protein. Annals of the New York Academy of Sciences. 2000;924(1):17-25. doi: 10.1111/j.1749-6632.2000.tb05554.x.
34. Hardy J. The genetic causes of neurodegenerative diseases. Journal of Alzheimer's Disease. 2001;3(1):109-16. doi: 10.3233/jad-2001-3115.
35. Glenner GG, Wong CW. Alzheimer's disease and Down's syndrome: Sharing of a unique cerebrovascular amyloid fibril protein. Biochemical and Biophysical Research Communications. 1984;122(3):1131-5. doi: 10.1016/0006-291x(84)91209-9.
36. Wisniewski KE, Wisniewski HM, Wen GY. Occurrence of neuropathological changes and dementia of Alzheimer's disease in Down's syndrome. Ann Neurol. 1985;17(3):278-82. doi: 10.1002/ana.410170310. PubMed PMID: 3158266.
37. Hampel H, Schneider LS, Giacobini E, Kivipelto M, Sindi S, Dubois B, Broich K, Nistico R, Aisen PS, Lista S. Advances in the therapy of Alzheimer's disease: targeting amyloid beta and tau and perspectives for the future. Expert Rev Neurother. 2015;15(1):83-105. doi: 10.1586/14737175.2015.995637. PubMed PMID: 25537424.
38. Cummings JL, Morstorf T, Zhong K. Alzheimer's disease drug-development pipeline: few candidates, frequent failures. Alzheimers Res Ther. 2014;6(4):37. doi: 10.1186/alzrt269. PubMed PMID: 25024750; PMCID: PMC4095696.
39. Doraiswamy PM, Leon J, Cummings JL, Marin D, Neumann PJ. Prevalence and Impact of Medical Comorbidity in Alzheimer's Disease. The Journals of Gerontology Series A: Biological Sciences and Medical Sciences. 2002;57(3):M173-M7. doi: 10.1093/gerona/57.3.M173.
40. Dubois B, Feldman HH, Jacova C, Cummings JL, DeKosky ST, Barberger-Gateau P, Delacourte A, Frisoni G, Fox NC, Galasko D, Gauthier S, Hampel H, Jicha GA, Meguro K, O'Brien J, Pasquier F, Robert P, Rossor M, Salloway S, Sarazin M, de Souza LC, Stern Y, Visser PJ, Scheltens P. Revising the definition of Alzheimer's disease: a new lexicon. The Lancet Neurology. 2010;9(11):1118-27. doi: 10.1016/s1474-4422(10)70223-4.
41. Jack CR, Knopman DS, Jagust WJ, Shaw LM, Aisen PS, Weiner MW, Petersen RC, Trojanowski JQ. Hypothetical model of dynamic biomarkers of the Alzheimer's pathological cascade. The Lancet Neurology. 2010;9(1):119-28. doi: 10.1016/S1474-4422(09)70299-6.
42. Jack CR, Knopman DS, Jagust WJ, Petersen RC, Weiner MW, Aisen PS, Shaw LM, Vemuri P, Wiste HJ, Weigand SD. Tracking pathophysiological processes in Alzheimer's disease: an updated hypothetical model of dynamic biomarkers. Lancet Neurol. 2013;12(2):207-16. doi: 10.1016/S1474-4422(12)70291-0.
43. Grothe MJ, Barthel H, Sepulcre J, Dyrba M, Sabri O, Teipel SJ, Alzheimer's Disease Neuroimaging I. In vivo staging of regional amyloid deposition. Neurology. 2017;89(20):2031-8. doi: 10.1212/WNL.0000000000004643. PubMed PMID: 29046362; PMCID: PMC5711511.
44. Scholl M, Lockhart SN, Schonhaut DR, O'Neil JP, Janabi M, Ossenkoppele R, Baker SL, Vogel JW, Faria J, Schwimmer HD, Rabinovici GD, Jagust WJ. PET Imaging of Tau Deposition in the Aging Human Brain. Neuron. 2016;89(5):971-82. doi: 10.1016/j.neuron.2016.01.028. PubMed PMID: 26938442; PMCID: PMC4779187.
45. Scholl M. Distinct 18F-AV-1451 tau PET retention patterns in early- and late-onset Alzheimer’s disease. Brain. 2017. doi: 10.1093/brain/awx171.
46. Honer M, Gobbi L, Martarello L, Comley RA. Radioligand development for molecular imaging of the central nervous system with positron emission tomography. Drug Discov Today. 2014;19(12):1936-44. doi: 10.1016/j.drudis.2014.08.012. PubMed PMID: 25173703.
47. Laruelle M. Relationships between radiotracer properties and image quality in molecular imaging of the brain with positron emission tomography. Molecular Imaging & Biology. 2003;5(6):363-75. doi: 10.1016/j.mibio.2003.09.009.
48. Pike VW. PET radiotracers: crossing the blood-brain barrier and surviving metabolism. Trends Pharmacol Sci. 2009;30(8):431-40. doi: 10.1016/j.tips.2009.05.005. PubMed PMID: 19616318; PMCID: PMC2805092.
49. Pike VW. Considerations in the Development of Reversibly Binding PET Radioligands for Brain Imaging. Curr Med Chem. 2016;23(18):1818-69. PubMed PMID: 27087244; PMCID: PMC5579844.

50. Mathis CA, Lopresti BJ, Ikonomovic MD, Klunk WE. Small-molecule PET tracers for imaging proteinopathies. Semin Nucl Med. 2017;47(5):553-75. doi: 10.1053/j.semnuclmed.2017.06.003. PubMed PMID: 28826526; PMCID: PMC5657567.

51. Villemagne VL, Fodero-Tavoletti MT, Masters CL, Rowe CC. Tau imaging: early progress and future directions. Lancet Neurol. 2015;14(1):114-24. doi: 10.1016/S1474-4422(14)70252-2. PubMed PMID: 25496902.

52. Makin OS, Serpell LC. Structures for amyloid fibrils. FEBS J. 2005;272(23):5950-61. doi: 10.1111/j.1742-4658.2005.05025.x. PubMed PMID: 16302960.

53. Fitzpatrick AWP, Falcon B, He S, Murzin AG, Murshudov G, Garringer HJ, Crowther RA, Ghetti B, Goedert M, Scheres SHW. Cryo-EM structures of tau filaments from Alzheimer's disease. Nature. 2017;547(7662):185-90. doi: 10.1038/nature23002. PubMed PMID: 28678775; PMCID: PMC5552202.

54. Schmidt M, Rohou A, Lasker K, Yadav JK, Schiene-Fischer C, Fandrich M, Grigorieff N. Peptide dimer structure in an Abeta(1-42) fibril visualized with cryo-EM. Proc Natl Acad Sci U S A. 2015;112(38):11858-63. doi: 10.1073/pnas.1503455112. PubMed PMID: 26351699; PMCID: PMC4586870.

55. Biancalana M, Koide S. Molecular mechanism of Thioflavin-T binding to amyloid fibrils. Biochim Biophys Acta. 2010;1804(7):1405-12. doi: 10.1016/j.bbapap.2010.04.001. PubMed PMID: 20399286; PMCID: PMC2880406.

56. Krebs MR, Bromley EH, Donald AM. The binding of thioflavin-T to amyloid fibrils: localisation and implications. J Struct Biol. 2005;149(1):30-7. doi: 10.1016/j.jsb.2004.08.002. PubMed PMID: 15629655.

57. Harada R, Okamura N, Furumoto S, Furukawa K, Ishiki A, Tomita N, Hiraoka K, Watanuki S, Shidahara M, Miyake M. [18F] THK-5117 PET for assessing neurofibrillary pathology in Alzheimer’s disease. Eur J Nucl Med Mol Imaging. 2015;42(7):1052-61. doi: 10.1007/s00259-015-3035-4.

58. Zhang W, Arteaga J, Cashion DK, Chen G, Gangadharmath U, Gomez LF, Kasi D, Lam C, Liang Q, Liu C, Mocharla VP, Mu F, Sinha A, Szardenings AK, Wang E, Walsh JC, Xia C, Yu C, Zhao T, Kolb HC. A highly selective and specific PET tracer for imaging of tau pathologies. J Alzheimers Dis. 2012;31(3):601-12. doi: 10.3233/JAD-2012-120712. PubMed PMID: 22683529.

59. Klunk WE, Wang Y, Huang G-f, Debnath ML, Holt DP, Shao L, Hamilton RL, Ikonomovic MD, DeKosky ST, Mathis CA. The binding of 2-(4′-methylaminophenyl) benzothiazole to postmortem brain homogenates is dominated by the amyloid component. The Journal of neuroscience. 2003;23(6):2086-92.

60. Marquié M, Normandin MD, Vanderburg CR, Costantino IM, Bien EA, Rycyna LG, Klunk WE, Mathis CA, Ikonomovic MD, Debnath ML. Validating novel tau positron emission tomography tracer [F-18]-AV-1451 (T807) on postmortem brain tissue. Ann Neurol. 2015;78(5):787-800. doi: 10.1002/ana.24517.

61. Heuer E, F. Rosen R, Cintron A, C. Walker L. Nonhuman Primate Models of Alzheimer-Like Cerebral Proteopathy. Current Pharmaceutical Design. 2012;18(8):1159-69. doi: 10.2174/138161212799315885.

62. Cohen RM, Rezai-Zadeh K, Weitz TM, Rentsendorj A, Gate D, Spivak I, Bholat Y, Vasilevko V, Glabe CG, Breunig JJ, Rakic P, Davtyan H, Agadjanyan MG, Kepe V, Barrio JR, Bannykh S, Szekely CA, Pechnick RN, Town T. A transgenic Alzheimer rat with plaques, tau pathology, behavioral impairment, oligomeric abeta, and frank neuronal loss. J Neurosci. 2013;33(15):6245-56. doi: 10.1523/JNEUROSCI.3672-12.2013. PubMed PMID: 23575824; PMCID: PMC3720142.

63. Klunk WE, Engler H, Nordberg A, Wang Y, Blomqvist G, Holt DP, Bergström M, Savitcheva I, Huang GF, Estrada S. Imaging brain amyloid in Alzheimer's disease with Pittsburgh Compound-B. Annals of neurology. 2004;55(3):306-19.

64. Price JC, Klunk WE, Lopresti BJ, Lu X, Hoge JA, Ziolko SK, Holt DP, Meltzer CC, DeKosky ST, Mathis CA. Kinetic modeling of amyloid binding in humans using PET imaging and Pittsburgh Compound-B. Journal of Cerebral Blood Flow & Metabolism. 2005;25(11):1528-47. doi: 10.1038/sj.jcbfm.9600146.

65. Mintun MA, Larossa GN, Sheline YI, Dence CS, Lee SY, Mach RH, Klunk WE, Mathis CA, DeKosky ST, Morris JC. [11C]PIB in a nondemented population: potential antecedent marker of Alzheimer disease. Neurology. 2006;67(3):446-52. doi: 10.1212/01.wnl.0000228230.26044.a4. PubMed PMID: 16894106.

66. Edison P, Archer H, Hinz R, Hammers A, Pavese N, Tai Y, Hotton G, Cutler D, Fox N, Kennedy A. Amyloid, hypometabolism, and cognition in Alzheimer disease An [11C] PIB and [18F] FDG PET study. Neurology. 2007;68(7):501-8.

67. Rowe C, Ng S, Ackermann U, Gong S, Pike K, Savage G, Cowie T, Dickinson K, Maruff P, Darby D. Imaging β-amyloid burden in aging and dementia. Neurology. 2007;68(20):1718-25.

68. Aizenstein HJ, Nebes RD, Saxton JA, Price JC, Mathis CA, Tsopelas ND, Ziolko SK, James JA, Snitz BE, Houck PR. Frequent amyloid deposition without significant cognitive impairment among the elderly. Archives of neurology. 2008;65(11):1509-17. doi: 10.1001/archneur.65.11.1509.

69. Forsberg A, Engler H, Almkvist O, Blomquist G, Hagman G, Wall A, Ringheim A, Långström B, Nordberg A. PET imaging of amyloid deposition in patients with mild cognitive impairment. Neurobiology of aging. 2008;29(10):1456-65.

70. Jack CR, Lowe VJ, Senjem ML, Weigand SD, Kemp BJ, Shiung MM, Knopman DS, Boeve BF, Klunk WE, Mathis CA. 11C PiB and structural MRI provide complementary information in imaging of Alzheimer's disease and amnestic mild cognitive impairment. Brain. 2008;131(3):665-80. doi: 10.1093/brain/awm336.

71. Jack CR, Jr., Lowe VJ, Weigand SD, Wiste HJ, Senjem ML, Knopman DS, Shiung MM, Gunter JL, Boeve BF, Kemp BJ, Weiner M, Petersen RC, Alzheimer's Disease Neuroimaging I. Serial PIB and MRI in normal, mild cognitive impairment and Alzheimer's disease: implications for sequence of pathological events in Alzheimer's disease. Brain. 2009;132(Pt 5):1355-65. doi: 10.1093/brain/awp062. PubMed PMID: 19339253; PMCID: PMC2677798.

72. Reiman EM, Chen K, Liu X, Bandy D, Yu M, Lee W, Ayutyanont N, Keppler J, Reeder SA, Langbaum JB. Fibrillar amyloid-β burden in cognitively normal people at 3 levels of genetic risk for Alzheimer's disease. Proceedings of the National Academy of Sciences. 2009;106(16):6820-5. doi: 10.1073/pnas.0900345106; PMCID: 19346482.

73. Johnson SC, Christian BT, Okonkwo OC, Oh JM, Harding S, Xu G, Hillmer AT, Wooten DW, Murali D, Barnhart TE, Hall LT, Racine AM, Klunk WE, Mathis CA, Bendlin BB, Gallagher CL, Carlsson CM, Rowley HA, Hermann BP, Dowling NM, Asthana S, Sager MA. Amyloid burden and neural function in people at risk for Alzheimer's Disease. Neurobiol Aging. 2014;35(3):576-84. doi: 10.1016/j.neurobiolaging.2013.09.028. PubMed PMID: 24269021; PMCID: PMC4018215.

74. Clark LR, Racine AM, Koscik RL, Okonkwo OC, Engelman CD, Carlsson CM, Asthana S, Bendlin BB, Chappell R, Nicholas CR, Rowley HA, Oh JM, Hermann BP, Sager MA, Christian BT, Johnson SC. Beta-amyloid and cognitive decline in late middle age: Findings from the Wisconsin Registry for Alzheimer's Prevention study. Alzheimers Dement. 2016;12(7):805-14. doi: 10.1016/j.jalz.2015.12.009. PubMed PMID: 26806386; PMCID: PMC4947439.

75. Rukovets O. Third Amyloid Imaging Agent Approved by the FDA. Neurology Today. 2014.

76. Yang LC, Rieves D, Ganley C. Brain Amyloid Imaging - FDA Approval of Florbetapir F18 Injection. New England Journal of Medicine. 2012;367(10):885-7. doi: 10.1056/NEJMp1208061. PubMed PMID: WOS:000308343300002.

77. Chien DT, Bahri S, Szardenings AK, Walsh JC, Mu F, Su MY, Shankle WR, Elizarov A, Kolb HC. Early clinical PET imaging results with the novel PHF-tau radioligand [F-18]-T807. J Alzheimers Dis. 2013;34(2):457-68. doi: 10.3233/JAD-122059. PubMed PMID: 23234879.

78. Maruyama M, Shimada H, Suhara T, Shinotoh H, Ji B, Maeda J, Zhang MR, Trojanowski JQ, Lee VM, Ono M, Masamoto K, Takano H, Sahara N, Iwata N, Okamura N, Furumoto S, Kudo Y, Chang Q, Saido TC, Takashima A, Lewis J, Jang MK, Aoki I, Ito H, Higuchi M. Imaging of tau pathology in a tauopathy mouse model and in Alzheimer patients compared to normal controls. Neuron. 2013;79(6):1094-108. doi: 10.1016/j.neuron.2013.07.037. PubMed PMID: 24050400; PMCID: PMC3809845.

79. Fodero-Tavoletti MT, Okamura N, Furumoto S, Mulligan RS, Connor AR, McLean CA, Cao D, Rigopoulos A, Cartwright GA, O'Keefe G, Gong S, Adlard PA, Barnham KJ, Rowe CC, Masters CL, Kudo Y, Cappai R, Yanai K, Villemagne VL. 18F-THK523: a novel in vivo tau imaging ligand for Alzheimer's disease. Brain. 2011;134(Pt 4):1089-100. doi: 10.1093/brain/awr038. PubMed PMID: 21436112.

80. Okamura N, Furumoto S, Harada R, Tago T, Yoshikawa T, Fodero-Tavoletti M, Mulligan RS, Villemagne VL, Akatsu H, Yamamoto T. Novel 18F-labeled arylquinoline derivatives for noninvasive imaging of tau pathology in Alzheimer disease. J Nucl Med. 2013;54(8):1420-7. doi: 10.2967/jnumed.112.117341.

81. Brier MR, Gordon B, Friedrichsen K, McCarthy J, Stern A, Christensen J, Owen C, Aldea P, Su Y, Hassenstab J, Cairns NJ, Holtzman DM, Fagan AM, Morris JC, Benzinger TL, Ances BM. Tau and Abeta imaging, CSF measures, and cognition in Alzheimer's disease. Sci Transl Med. 2016;8(338):338ra66. doi: 10.1126/scitranslmed.aaf2362. PubMed PMID: 27169802; PMCID: PMC5267531.

82. Johnson KA, Schultz A, Betensky RA, Becker JA, Sepulcre J, Rentz D, Mormino E, Chhatwal J, Amariglio R, Papp K. Tau positron emission tomographic imaging in aging and early Alzheimer disease. Ann Neurol. 2015;79(1):110-9. doi: 10.1002/ana.24546.

83. Lowe VJ, Curran G, Fang P, Liesinger AM, Josephs KA, Parisi JE, Kantarci K, Boeve BF, Pandey MK, Bruinsma T, Knopman DS, Jones DT, Petrucelli L, Cook CN, Graff-Radford NR, Dickson DW, Petersen RC, Jack CR, Jr., Murray ME. An autoradiographic evaluation of AV-1451 Tau PET in dementia. Acta Neuropathol Commun. 2016;4(1):58. doi: 10.1186/s40478-016-0315-6. PubMed PMID: 27296779; PMCID: PMC4906968.

84. Lowe VJ, Wiste HJ, Senjem ML, Weigand SD, Therneau TM, Boeve BF, Josephs KA, Fang P, Pandey MK, Murray ME, Kantarci K, Jones DT, Vemuri P, Graff-Radford J, Schwarz CG, Machulda MM, Mielke MM, Roberts RO, Knopman DS, Petersen RC, Jack CR, Jr. Widespread brain tau and its association with ageing, Braak stage and Alzheimer's dementia. Brain. 2018;141(1):271-87. doi: 10.1093/brain/awx320. PubMed PMID: 29228201.

85. Villemagne VL, Okamura N. Tau imaging in the study of ageing, Alzheimer's disease, and other neurodegenerative conditions. Current opinion in neurobiology. 2016;36:43-51. doi: 10.1016/j.conb.2015.09.002.

86. Chiotis K, Saint-Aubert L, Rodriguez-Vieitez E, Leuzy A, Almkvist O, Savitcheva I, Jonasson M, Lubberink M, Wall A, Antoni G, Nordberg A. Longitudinal changes of tau PET imaging in relation to hypometabolism in prodromal and Alzheimer's disease dementia. Mol Psychiatry. 2017. doi: 10.1038/mp.2017.108. PubMed PMID: 28507319.

87. Chiotis K, Saint-Aubert L, Savitcheva I, Jelic V, Andersen P, Jonasson M, Eriksson J, Lubberink M, Almkvist O, Wall A, Antoni G, Nordberg A. Imaging in-vivo tau pathology in Alzheimer's disease with THK5317 PET in a multimodal paradigm. Eur J Nucl Med Mol Imaging. 2016;43(9):1686-99. doi: 10.1007/s00259-016-3363-z. PubMed PMID: 26996778.

88. Schwarz AJ, Yu P, Miller BB, Shcherbinin S, Dickson J, Navitsky M, Joshi AD, Devous MD, Sr., Mintun MS. Regional profiles of the candidate tau PET ligand 18F-AV-1451 recapitulate key features of Braak histopathological stages. Brain. 2016;139(Pt 5):1539-50. doi: 10.1093/brain/aww023. PubMed PMID: 26936940.

89. Dubois B, Hampel H, Feldman HH, Scheltens P, Aisen P, Andrieu S, Bakardjian H, Benali H, Bertram L, Blennow K, Broich K, Cavedo E, Crutch S, Dartigues JF, Duyckaerts C, Epelbaum S, Frisoni GB, Gauthier S, Genthon R, Gouw AA, Habert MO, Holtzman DM, Kivipelto M, Lista S, Molinuevo JL, O'Bryant SE, Rabinovici GD, Rowe C, Salloway S, Schneider LS, Sperling R, Teichmann M, Carrillo MC, Cummings J, Jack CR, Jr., Proceedings of the Meeting of the International Working G, the American Alzheimer's Association on "The Preclinical State of AD, July, Washington Dc USA. Preclinical Alzheimer's disease: Definition, natural history, and diagnostic criteria. Alzheimers Dement. 2016;12(3):292-323. doi: 10.1016/j.jalz.2016.02.002. PubMed PMID: 27012484.

90. Jack CR, Bennett DA, Blennow K, Carrillo MC, Dunn B, Elliott CL, Haeberlein SB, Holtzman DM, Jagust WJ, Jessen F, Karlawish J, Liu E, Molinuevo JL, Montine TJ, Phelps C, Rankin K, Rowe CC, Ryan LM, Scheltens P, Siemers ER, Silverberg N, Snyder HM, Sperling RA. 2017 Nia-Aa Research Framework to Investigate the Alzheimer's Disease Continuum. Alzheimer's Association International Conference; July 182017. p. P890-P1.

91. Jack CR, Jr., Bennett DA, Blennow K, Carrillo MC, Feldman HH, Frisoni GB, Hampel H, Jagust WJ, Johnson KA, Knopman DS, Petersen RC, Scheltens P, Sperling RA, Dubois B. A/T/N: An unbiased descriptive classification scheme for Alzheimer disease biomarkers. Neurology. 2016;87(5):539-47. doi: 10.1212/WNL.0000000000002923. PubMed PMID: 27371494; PMCID: PMC4970664.

92. Jack CR, Jr., Wiste HJ, Weigand SD, Therneau TM, Lowe VJ, Knopman DS, Gunter JL, Senjem ML, Jones DT, Kantarci K, Machulda MM, Mielke MM, Roberts RO, Vemuri P, Reyes DA, Petersen RC. Defining imaging biomarker cut points for brain aging and Alzheimer's disease. Alzheimers Dement. 2017;13(3):205-16. doi: 10.1016/j.jalz.2016.08.005. PubMed PMID: 27697430; PMCID: PMC5344738.

93. Betthauser TJ, Ellison PA, Murali D, Lao PJ, Barnhart TE, Furumoto S, Okamura N, Johnson SC, Engle JW, Nickles RJ, Christian BT. Characterization of the radiosynthesis and purification of [(18)F]THK-5351, a PET ligand for neurofibrillary tau. Appl Radiat Isot. 2017;130:230-7. doi: 10.1016/j.apradiso.2017.10.002. PubMed PMID: 29031087; PMCID: PMC5673567.

94. Harada R, Okamura N, Furumoto S, Furukawa K, Ishiki A, Tomita N, Tago T, Hiraoka K, Watanuki S, Shidahara M, Miyake M, Ishikawa Y, Matsuda R, Inami A, Yoshikawa T, Funaki Y, Iwata R, Tashiro M, Yanai K, Arai H, Kudo Y. 18F-THK5351: A novel PET radiotracer for imaging neurofibrillary pathology in Alzheimer disease. J Nucl Med. 2016;57(2):208-14. doi: 10.2967/jnumed.115.164848. PubMed PMID: 26541774.

95. Tago T, Furumoto S, Okamura N, Harada R, Adachi H, Ishikawa Y, Yanai K, Iwata R, Kudo Y. Structure-activity relationship of 2-arylquinolines as PET imaging tracers for tau pathology in Alzheimer disease. J Nucl Med. 2016;57(4):608-14. doi: 10.2967/jnumed.115.166652. PubMed PMID: 26697966.
96. Neelamegam R, Yokell DL, Rice PA, Furumoto S, Kudo Y, Okamura N, El Fakhri G. A report of the automated radiosynthesis of the tau positron emission tomography radiopharmaceutical, [18 F]-THK-5351. J Labelled Comp Radiopharm. 2017;60(2):140-6. doi: 10.1002/jlcr.3482. PubMed PMID: 27859483.
97. Lazari M, Quinn KM, Claggett SB, Collins J, Shah GJ, Herman HE, Maraglia B, Phelps ME, Moore MD, van Dam RM. ELIXYS - a fully automated, three-reactor high-pressure radiosynthesizer for development and routine production of diverse PET tracers. EJNMMI Res. 2013;3(1):52. doi: 10.1186/2191-219X-3-52. PubMed PMID: 23849185; PMCID: PMC3717127.
98. Lazari M, Collins J, Shen B, Farhoud M, Yeh D, Maraglia B, Chin FT, Nathanson DA, Moore M, van Dam RM. Fully automated production of diverse 18F-labeled PET tracers on the ELIXYS multireactor radiosynthesizer without hardware modification. J Nucl Med Technol. 2014;42(3):203-10. doi: 10.2967/jnmt.114.140392. PubMed PMID: 25033883; PMCID: PMC4491436.
99. Harada R, Furumoto S, Tago T, Katsutoshi F, Ishiki A, Tomita N, Iwata R, Tashiro M, Arai H, Yanai K. Characterization of the radiolabeled metabolite of tau PET tracer 18F-THK5351. Eur J Nucl Med. 2016:1-8. doi: 10.1007/s00259-016-3453-y.
100. Jacobson MS, Dankwart HR, Mahoney DW. Radiolysis of 2-[18F]fluoro-2-deoxy-D-glucose ([18F]FDG) and the role of ethanol and radioactive concentration. Appl Radiat Isot. 2009;67(6):990-5. doi: 10.1016/j.apradiso.2009.01.005. PubMed PMID: 19231219.
101. Kolb HCW, Joseph; Mocharla, Vani; Mu, Fanrong; Gangadharmath, Umesh, inventor; Siemens Medical Solutions USA, Inc. (Malvern, PA) assignee. Formulation, apparatus and method for stabilizing radiopharmaceuticals. United States2016 February 16, 2012.
102. Hostetler ED, Walji AM, Zeng Z, Miller P, Bennacef I, Salinas C, Connolly B, Gantert L, Haley H, Holahan M, Purcell M, Riffel K, Lohith TG, Coleman P, Soriano A, Ogawa A, Xu S, Zhang X, Joshi E, Della Rocca J, Hesk D, Schenk DJ, Evelhoch JL. Preclinical characterization of 18F-MK-6240, a promising PET tracer for in vivo quantification of human neurofibrillary tangles. J Nucl Med. 2016;57(10):1599-606. doi: 10.2967/jnumed.115.171678. PubMed PMID: 27230925.
103. Collier TL, Yokell DL, Livni E, Rice PA, Celen S, Serdons K, Neelamegam R, Bormans G, Harris D, Walji A, Hostetler ED, Bennacef I, Vasdev N. cGMP production of the radiopharmaceutical [18 F]MK-6240 for PET imaging of human neurofibrillary tangles. J Labelled Comp Radiopharm. 2017. doi: 10.1002/jlcr.3496. PubMed PMID: 28185305.
104. Lang L, Eckelman WC. One-step synthesis of 18F labeled [18F]-N-succinimidyl 4-(fluoromethyl)benzoate for protein labeling. Applied Radiation and Isotopes. 1994;45(12):1155-63. doi: 10.1016/0969-8043(94)90031-0.
105. Jacobson O, Kiesewetter DO, Chen X. Fluorine-18 radiochemistry, labeling strategies and synthetic routes. Bioconjug Chem. 2015;26(1):1-18. doi: 10.1021/bc500475e. PubMed PMID: 25473848; PMCID: PMC4306521.
106. Scott PJ, Hockley BG, Kung HF, Manchanda R, Zhang W, Kilbourn MR. Studies into radiolytic decomposition of fluorine-18 labeled radiopharmaceuticals for positron emission tomography. Appl Radiat Isot. 2009;67(1):88-94. doi: 10.1016/j.apradiso.2008.08.015. PubMed PMID: 18951032.
107. Betthauser T, Lao PJ, Murali D, Barnhart TE, Furumoto S, Okamura N, Stone CK, Johnson SC, Christian BT. In vivo comparison of tau radioligands ^{18}F-THK-5351 and ^{18}F-THK-5317. J Nucl Med. 2016. doi: 10.2967/jnumed.116.182980. PubMed PMID: 27856627.
108. Betthauser T, Cody K, Zammit M, Murali D, Converse AK, Barnhart TE, Stone CK, Rowley HA, Johnson SC, Christian BT. In vivo characterization and quantification of neurofibrillary tau PET radioligand [18F-]MK-6240 in humans from Alzheimer's disease dementia to young controls. J Nucl Med. In Review.
109. Herscovitch P. Regulatory approval and insurance reimbursement: the final steps in clinical translation of amyloid brain imaging. Clinical and Translational Imaging. 2015;3(1):75-7. doi: 10.1007/s40336-015-0101-7.
110. Shoghi-Jadid K, Small GW, Agdeppa ED, Kepe V, Ercoli LM, Siddarth P, Read S, Satyamurthy N, Petric A, Huang S-C, Barrio JR. Localization of neurofibrillary tangles and beta-amyloid plaques in the brains of living patients with Alzheimer disease. Am J Geriatr Psychiatry. 2002;10(1):24-35. doi: 10.1097/00019442-200201000-00004.

111. Xia C-F, Arteaga J, Chen G, Gangadharmath U, Gomez LF, Kasi D, Lam C, Liang Q, Liu C, Mocharla VP. [18 F] T807, a novel tau positron emission tomography imaging agent for Alzheimer's disease. Alzheimers Dement. 2013;9(6):666-76. doi: 10.1016/j.jalz.2012.11.008.

112. Gordon BA, Friedrichsen K, Brier M, Blazey T, Su Y, Christensen J, Aldea P, McConathy J, Holtzman DM, Cairns NJ, Morris JC, Fagan AM, Ances BM, Benzinger TL. The relationship between cerebrospinal fluid markers of Alzheimer pathology and positron emission tomography tau imaging. Brain. 2016;139(Pt 8):2249-60. Epub June 10, 2016. doi: 10.1093/brain/aww139. PubMed PMID: 27286736; PMCID: PMC4958902.

113. Shimada H, Kitamura S, Shinotoh H, Endo H, Niwa F, Hirano S, Kimura Y, Zhang MR, Kuwabara S, Suhara T, Higuchi M. Association between Abeta and tau accumulations and their influence on clinical features in aging and Alzheimer's disease spectrum brains: A [(11)C]PBB3-PET study. Alzheimers Dement (Amst). 2017;6:11-20. doi: 10.1016/j.dadm.2016.12.009. PubMed PMID: 28138509; PMCID: PMC5257028.

114. Hashimoto H, Kawamura K, Igarashi N, Takei M, Fujishiro T, Aihara Y, Shiomi S, Muto M, Ito T, Furutsuka K, Yamasaki T, Yui J, Xie L, Ono M, Hatori A, Nemoto K, Suhara T, Higuchi M, Zhang MR. Radiosynthesis, photoisomerization, biodistribution, and metabolite analysis of 11C-PBB3 as a clinically useful PET probe for imaging of tau pathology. J Nucl Med. 2014;55(9):1532-8. doi: 10.2967/jnumed.114.139550. PubMed PMID: 24963128.

115. Shimada H, Kitamura S, Ono M, Kimura Y, Ichise M, Takahata K, Moriguchi S, Kubota M, Ishii T, Takado Y, Seki C, Hirano S, Shinotoh H, Sahara N, Tempest P, Tamagnan G, Seibyl J, Barret O, Alagille D, Zhang M-R, Kuwabara S, Jang M-K, Marek K, Suhara T, Higuchi M, editors. First-in-Human Pet Study with 18 F-Am-Pbb3 and 18 F-Pm-Pbb3. Alzheimer's Association International Conference; 2017.

116. Harada R, Okamura N, Furumoto S, Furukawa K, Ishiki A, Tomita N, Tago T, Iwata R, Yanai K, Arai H, Kudo Y. Validation of the binding specificity of Tau PET tracer [18F]THK-5351 on postmortem human brain samples. Alzheimers Dement. 2015;11(7):P271. doi: 10.1016/j.jalz.2015.07.354.

117. Walji AM, Hostetler ED, Selnick H, Zeng Z, Miller P, Bennacef I, Salinas C, Connolly B, Gantert L, Holahan M, O'Malley S, Purcell M, Riffel K, Li J, Balsells J, JA OB, Melquist S, Soriano A, Zhang X, Ogawa A, Xu S, Joshi E, Della Rocca J, Hess FJ, Schachter J, Hesk D, Schenk D, Struyk A, Babaoglu K, Lohith TG, Wang Y, Yang K, Fu J, Evelhoch JL, Coleman PJ. Discovery of 6-(Fluoro-(18)F)-3-(1H-pyrrolo[2,3-c]pyridin-1-yl)isoquinolin-5-amine ([(18)F]-MK-6240): A Positron Emission Tomography (PET) Imaging Agent for Quantification of Neurofibrillary Tangles (NFTs). J Med Chem. 2016;59(10):4778-89. doi: 10.1021/acs.jmedchem.6b00166. PubMed PMID: 27088900.

118. Bohorquez SS, Barret O, Tamagnan G, Alagille D, Marik J, Ayalon G, Bengtsson T, de Crespigny A, Jennings D, Seibyl JP, Marek K, Weimer R, Kerchner GA, editors. Evaluation of Tau Burden in a Cross-Sectional Cohort of Alzheimer’s Disease Subjects Using [18f]Gtp1 (Genentech Tau Probe 1). Alzheimer's Association International Conference; 2016.

119. Barret O, Seibyl J, Stephens A, Madonia J, Alagille D, Mueller A, Berndt M, Kroth H, Capotosti F, Muhs A, Pfeifer A, Tamagnan G, Dinkelborg L, Marek K, editors. First-in-Human Pet Studies with the Next Generation Tau Agent 18-F Pi-2620 in Alzheimer’s Disease, Progressive Supranuclear Palsy, and Controls. Alzheimer's Association International Conference; 2017.

120. Declercq L, Rombouts F, Koole M, Fierens K, Marien J, Langlois X, Andres JI, Schmidt M, Macdonald G, Moechars D, Vanduffel W, Tousseyn T, Vandenberghe R, Van Laere K, Verbruggen A, Bormans G. Preclinical Evaluation of (18)F-JNJ64349311, a Novel PET Tracer for Tau Imaging. J Nucl Med. 2017;58(6):975-81. doi: 10.2967/jnumed.116.185199. PubMed PMID: 28232614.

121. Honer M, Gobbi L, Knust H, Kuwabara H, Muri D, Koerner M, Valentine H, Dannals RF, Wong DF, Borroni E. Preclinical Evaluation of (18)F-RO6958948, (11)C-RO6931643 and (11)C-RO6924963 as Novel Radiotracers for Imaging Aggregated Tau in AD with Positron Emission Tomography. J Nucl Med. 2017. doi: 10.2967/jnumed.117.196741. PubMed PMID: 28970331.

122. Mintun MA, Raichle ME, Kilbourn MR, Wooten GF, Welch MJ. A quantitative model for the in vivo assessment of drug binding sites with positron emission tomography. Ann Neurol. 1984;15(3):217-27. doi: 10.1002/ana.410150302. PubMed PMID: 6609679.

123. Innis RB, Cunningham VJ, Delforge J, Fujita M, Gjedde A, Gunn RN, Holden J, Houle S, Huang SC, Ichise M, Iida H, Ito H, Kimura Y, Koeppe RA, Knudsen GM, Knuuti J, Lammertsma AA, Laruelle M, Logan J, Maguire RP, Mintun MA, Morris ED, Parsey R, Price JC, Slifstein M, Sossi V, Suhara T, Votaw JR, Wong DF, Carson RE. Consensus nomenclature for in vivo imaging of reversibly binding radioligands. J Cereb Blood Flow Metab. 2007;27(9):1533-9. doi: 10.1038/sj.jcbfm.9600493. PubMed PMID: 17519979.

124. Logan J, Fowler JS, Volkow ND, Wang G-J, Ding Y-S, Alexoff DL. Distribution volume ratios without blood sampling from graphical analysis of PET data. J Cereb Blood Flow Metab. 1996;16(5):834-40. doi: 10.1097/00004647-199609000-00008.

125. Ichise M, Ballinger JR, Golan H, Vines D, Luong A, Tsai S, Kung HF. Noninvasive quantification of dopamine D2 receptors with iodine-123-IBF SPECT. J Nucl Med. 1996;37(3):513-20.

126. Lammertsma AA, Hume SP. Simplified reference tissue model for PET receptor studies. Neuroimage. 1996;4(3 Pt 1):153-8. doi: 10.1006/nimg.1996.0066. PubMed PMID: 9345505.

127. Gunn RN, Lammertsma AA, Hume SP, Cunningham VJ. Parametric imaging of ligand-receptor binding in PET using a simplified reference region model. Neuroimage. 1997;6(4):279-87. doi: DOI 10.1006/nimg.1997.0303. PubMed PMID: WOS:000071052500006.

128. Koeppe RA, Holden JE, Ip WR. Performance comparison of parameter estimation techniques for the quantitation of local cerebral blood flow by dynamic positron computed tomography. J Cereb Blood Flow Metab. 1985;5(2):224-34. doi: 10.1038/jcbfm.1985.29. PubMed PMID: 3872874.

129. Ichise M, Liow JS, Lu JQ, Takano A, Model K, Toyama H, Suhara T, Suzuki K, Innis RB, Carson RE. Linearized reference tissue parametric imaging methods: application to [11C]DASB positron emission tomography studies of the serotonin transporter in human brain. J Cereb Blood Flow Metab. 2003;23(9):1096-112. doi: 10.1097/01.WCB.0000085441.37552.CA. PubMed PMID: 12973026.

130. Wu Y, Carson RE. Noise reduction in the simplified reference tissue model for neuroreceptor functional imaging. J Cereb Blood Flow Metab. 2002;22(12):1440-52. doi: 10.1097/00004647-200212000-00004. PubMed PMID: 12468889.

131. Carson RE, Channing MA, Blasberg RG, Dunn BB, Cohen RM, Rice KC, Herscovitch P. Comparison of bolus and infusion methods for receptor quantitation—Application to [F-18] cyclofoxy and positron emission tomography. J Cereb Blood Flow Metab. 1993;13(1). doi: 10.1038/jcbfm.1993.6.

132. Lemoine L, Saint-Aubert L, Marutle A, Antoni G, Eriksson JP, Ghetti B, Okamura N, Nennesmo I, Gillberg PG, Nordberg A. Visualization of regional tau deposits using (3)H-THK5117 in Alzheimer brain tissue. Acta Neuropathol Commun. 2015;3(1):40. doi: 10.1186/s40478-015-0220-4. PubMed PMID: 26134112; PMCID: PMC4489196.

133. Harada R, Okamura N, Furumoto S, Tago T, Yanai K, Arai H, Kudo Y. Characteristics of tau and its ligands in PET imaging. Biomolecules. 2016;6(1):7. doi: 10.3390/biom6010007. PubMed PMID: 26751494; PMCID: PMC4808801.

134. Tago T, Furumoto S, Okamura N, Harada R, Adachi H, Ishikawa Y, Yanai K, Iwata R, Kudo Y. Preclinical evaluation of [(18)F]THK-5105 enantiomers: effects of chirality on its effectiveness as a tau imaging radiotracer. Mol Imaging Biol. 2016;18(2):258-66. doi: 10.1007/s11307-015-0879-8. PubMed PMID: 26194011.

135. Jonasson M, Wall A, Chiotis K, Saint-Aubert L, Wilking H, Sprycha M, Borg B, Thibblin A, Eriksson J, Sorensen J, Antoni G, Nordberg A, Lubberink M. Tracer kinetic analysis of (S)-18F-THK5117 as a PET tracer for assessing tau pathology. J Nucl Med. 2016;57(4):574-81. doi: 10.2967/jnumed.115.158519. PubMed PMID: 26795290.

136. Ishiki A, Okamura N, Furukawa K, Furumoto S, Harada R, Tomita N, Hiraoka K, Watanuki S, Ishikawa Y, Tago T, Funaki Y, Iwata R, Tashiro M, Yanai K, Kudo Y, Arai H. Longitudinal assessment of tau pathology in patients with Alzheimer's disease using [18F]THK-5117 positron emission tomography. PLoS One. 2015;10(10):e0140311. doi: 10.1371/journal.pone.0140311. PubMed PMID: 26461913; PMCID: PMC4604169.

137. Lockhart SN, Baker SL, Okamura N, Furukawa K, Ishiki A, Furumoto S, Tashiro M, Yanai K, Arai H, Kudo Y, Harada R, Tomita N, Hiraoka K, Watanuki S, Jagust WJ. Dynamic PET measures of tau accumulation in cognitively normal older adults and Alzheimer's disease patients measured using [18F] THK-5351. PLoS One. 2016;11(6):e0158460. doi: 10.1371/journal.pone.0158460. PubMed PMID: 27355840.

138. Ng KP, Pascoal TA, Mathotaarachchi S, Therriault J, Kang MS, Shin M, Guiot MC, Guo Q, Harada R, Comley RA, Massarweh G, Soucy JP, Okamura N, Gauthier S, Rosa-Neto P. Monoamine oxidase B inhibitor, selegiline, reduces 18F-THK5351 uptake in the human brain. Alzheimers Res Ther. 2017;9(1):25. doi: 10.1186/s13195-017-0253-y. PubMed PMID: 28359327; PMCID: PMC5374697.

139. Lemoine L, Gillberg PG, Svedberg M, Stepanov V, Jia Z, Huang J, Nag S, Tian H, Ghetti B, Okamura N, Higuchi M, Halldin C, Nordberg A. Comparative binding properties of the tau PET tracers THK5117, THK5351, PBB3, and T807 in postmortem Alzheimer brains. Alzheimers Res Ther. 2017;9(1):96. doi: 10.1186/s13195-017-0325-z. PubMed PMID: 29229003; PMCID: PMC5725799.

140. Koscik RL, La Rue A, Jonaitis EM, Okonkwo OC, Johnson SC, Bendlin BB, Hermann BP, Sager MA. Emergence of mild cognitive impairment in late middle-aged adults in the wisconsin registry for Alzheimer's prevention. Dement Geriatr Cogn Disord. 2014;38(1-2):16-30. doi: 10.1159/000355682. PubMed PMID: 24556849; PMCID: PMC4104157.

141. Johnson SC, Koscik RL, Jonaitis EM, Clark LR, Mueller KD, Berman SE, Bendlin BB, Engelman CD, Okonkwo OC, Hogan KJ, Asthana S, Carlsson CM, Hermann BP, Sager MA. The Wisconsin Registry for Alzheimer's Prevention: A review of findings and current directions. Alzheimers Dement (Amst). 2018;10:130-42. doi: 10.1016/j.dadm.2017.11.007. PubMed PMID: 29322089; PMCID: PMC5755749.

142. Solbach C, Uebele M, Reischl G, Machulla HJ. Efficient radiosynthesis of carbon-11 labelled uncharged Thioflavin T derivatives using [11C]methyl triflate for beta-amyloid imaging in Alzheimer's Disease with PET. Appl Radiat Isot. 2005;62(4):591-5. doi: 10.1016/j.apradiso.2004.09.003. PubMed PMID: 15701414.

143. Floberg JM, Mistretta CA, Weichert JP, Hall LT, Holden JE, Christian BT. Improved kinetic analysis of dynamic PET data with optimized HYPR-LR. Med Phys. 2012;39(6):3319-31. doi: 10.1118/1.4718669. PubMed PMID: 22755714; PMCID: PMC3371076.

144. Christian BT, Vandehey NT, Floberg JM, Mistretta CA. Dynamic PET denoising with HYPR processing. J Nucl Med. 2010;51(7):1147-54. doi: 10.2967/jnumed.109.073999.

145. Racine AM, Clark LR, Berman SE, Koscik RL, Mueller KD, Norton D, Nicholas CR, Blennow K, Zetterberg H, Jedynak B, Bilgel M, Carlsson CM, Christian BT, Asthana S, Johnson SC. Associations between performance on an abbreviated CogState battery, other measures of cognitive function, and biomarkers in people at risk for Alzheimer's disease. J Alzheimers Dis. 2016;54(4):1395-408. doi: 10.3233/JAD-160528. PubMed PMID: 27589532; PMCID: PMC5074904.

146. Joachim C, Morris J, Selkoe D. Diffuse senile plaques occur commonly in the cerebellum in Alzheimer's disease. Am J Pathol. 1989;135(2):309.

147. Altman DG, Bland JM. Measurement in medicine - the analysis of method comparison studies. Statistician. 1983;32(3):307-17. doi: 10.2307/2987937. PubMed PMID: WOS:A1983RP04600005.

148. Bland JM, Altman DG. Measuring agreement in method comparison studies. Stat Methods Med Res. 1999;8(2):135-60. PubMed PMID: 10501650.

149. Slifstein M, Laruelle M. Effects of statistical noise on graphic analysis of PET neuroreceptor studies. J Nucl Med. 2000;41(12):2083-8. PubMed PMID: 11138696.

150. Wooten DW, Guehl NJ, Verwer EE, Shoup TM, Yokell DL, Zubcevik N, Vasdev N, Zafonte RD, Johnson KA, El Fakhri G, Normandin MD. Pharmacokinetic evaluation of the tau PET radiotracer (18)F-T807 ((18)F-AV-1451) in human subjects. J Nucl Med. 2017;58(3):484-91. doi: 10.2967/jnumed.115.170910. PubMed PMID: 27660144; PMCID: PMC5334185.

151. Fowler JS, MacGregor RR, Wolf AP, Arnett CD, Dewey SL, Schlyer D, Christman D, Logan J, Smith M, Sachs H, et al. Mapping human brain monoamine oxidase A and B with 11C-labeled suicide inactivators and PET. Science. 1987;235(4787):481-5. doi: 10.1126/science.3099392. PubMed PMID: 3099392.

152. Fowler JS, Volkow ND, Wang GJ, Logan J, Pappas N, Shea C, MacGregor R. Age-related increases in brain monoamine oxidase B in living healthy human subjects. Neurobiol Aging. 1997;18(4):431-5. PubMed PMID: 9330975.

153. Hirvonen J, Kailajarvi M, Haltia T, Koskimies S, Nagren K, Virsu P, Oikonen V, Sipila H, Ruokoniemi P, Virtanen K, Scheinin M, Rinne JO. Assessment of MAO-B occupancy in the brain with PET and [11C]-L-deprenyl-D2: a dose-finding study with a novel MAO-B inhibitor, EVT 301. Clin Pharmacol Ther. 2009;85(5):506-12. doi: 10.1038/clpt.2008.241. PubMed PMID: 19129751.

154. Vemuri P, Lesnick TG, Przybelski SA, Knopman DS, Lowe VJ, Graff-Radford J, Roberts RO, Mielke MM, Machulda MM, Petersen RC, Jack CR, Jr. Age, vascular health, and Alzheimer disease biomarkers in an elderly sample. Ann Neurol. 2017;82(5):706-18. doi: 10.1002/ana.25071. PubMed PMID: 29023983; PMCID: PMC5696029.

155. Harada R, Ishiki A, Kai H, Sato N, Furukawa K, Furumoto S, Tago T, Tomita N, Watanuki S, Hiraoka K, Ishikawa Y, Funaki Y, Nakamura T, Yoshikawa T, Iwata R, Tashiro M, Sasano H, Kitamoto T, Yanai K, Arai H, Kudo Y, Okamura N. Correlations of (18)F-THK5351 PET with post-mortem burden of tau and astrogliosis in Alzheimer's disease. J Nucl Med. 2017. doi: 10.2967/jnumed.117.197426. PubMed PMID: 28864633.

156. Wilson AA, Garcia A, Parkes J, McCormick P, Stephenson KA, Houle S, Vasdev N. Radiosynthesis and initial evaluation of [18F]-FEPPA for PET imaging of peripheral benzodiazepine receptors. Nucl Med Biol. 2008;35(3):305-14. doi: 10.1016/j.nucmedbio.2007.12.009. PubMed PMID: 18355686.

157. Camsonne R, Crouzel C, Comar D, Mazière M, Prenant C, Sastre J, Moulin M, Syrota A. Synthesis of N-(11C) methyl, N-(methyl-1 propyl), (chloro-2 phenyl)-1 isoquinoleine carboxamide-3 (PK 11195): A new ligand for peripheral benzodiazepine receptors. Journal of Labelled Compounds and Radiopharmaceuticals. 1984;21(10):985-91. doi: 10.1002/jlcr.2580211012.
158. Fujita M, Imaizumi M, Zoghbi SS, Fujimura Y, Farris AG, Suhara T, Hong J, Pike VW, Innis RB. Kinetic analysis in healthy humans of a novel positron emission tomography radioligand to image the peripheral benzodiazepine receptor, a potential biomarker for inflammation. Neuroimage. 2008;40(1):43-52. doi: 10.1016/j.neuroimage.2007.11.011. PubMed PMID: 18093844; PMCID: PMC2265774.
159. Boutin H, Chauveau F, Thominiaux C, Gregoire MC, James ML, Trebossen R, Hantraye P, Dolle F, Tavitian B, Kassiou M. 11C-DPA-713: A Novel Peripheral Benzodiazepine Receptor PET Ligand for In Vivo Imaging of Neuroinflammation. Journal of Nuclear Medicine. 2007;48(4):573-81. doi: 10.2967/jnumed.106.036764.
160. Heneka MT, Carson MJ, Khoury JE, Landreth GE, Brosseron F, Feinstein DL, Jacobs AH, Wyss-Coray T, Vitorica J, Ransohoff RM, Herrup K, Frautschy SA, Finsen B, Brown GC, Verkhratsky A, Yamanaka K, Koistinaho J, Latz E, Halle A, Petzold GC, Town T, Morgan D, Shinohara ML, Perry VH, Holmes C, Bazan NG, Brooks DJ, Hunot S, Joseph B, Deigendesch N, Garaschuk O, Boddeke E, Dinarello CA, Breitner JC, Cole GM, Golenbock DT, Kummer MP. Neuroinflammation in Alzheimer's disease. The Lancet Neurology. 2015;14(4):388-405. doi: 10.1016/s1474-4422(15)70016-5.
161. Betthauser TJ, Hillmer AT, Lao PJ, Ehlerding E, Mukherjee J, Stone CK, Christian BT. Human biodistribution and dosimetry of [18 F]nifene, an α4β2* nicotinic acetylcholine receptor PET tracer. Nuclear Medicine and Biology. 2017;55:7-11. doi: 10.1016/j.nucmedbio.2017.08.001.
162. Cristy M, Eckerman K. Specific absorbed fractions of energy at various ages from internal photon sources. ORNL/TM-8381. 1987;3.
163. Stabin M. MIRDOSE: personal computer software for internal dose assessment in nuclear medicine. J Nucl Med. 1996;37(3):538-46.
164. Stabin MG, Sparks RB, Crowe E. OLINDA/EXM: the second-generation personal computer software for internal dose assessment in nuclear medicine. J Nucl Med. 2005;46(6):1023-7. PubMed PMID: 15937315.
165. Siegel JA, S.R. T, J.B. S, M.G. S, M.T. H, K.F. K, J.S. R, R.W. H, D.R. F, D.A. W, A.B. B. MIRD pamphlet no. 16: Techniques for quantitative radiopharmaceutical biodistribution data acquisition and analysis for use in human radiation dose estimates. J Nucl Med. 1999;40(2):37S-61S.
166. Davies P. Selective Loss of Central Cholinergic Neurons in Alzheimer's Disease. The Lancet. 1976;308(8000):1403. doi: 10.1016/s0140-6736(76)91936-x.
167. Bartus R, Dean R, Beer B, Lippa A. The cholinergic hypothesis of geriatric memory dysfunction. Science. 1982;217(4558):408-14. doi: 10.1126/science.7046051.
168. Gotti C, Clementi F. Neuronal nicotinic receptors: from structure to pathology. Prog Neurobiol. 2004;74(6):363-96. doi: 10.1016/j.pneurobio.2004.09.006. PubMed PMID: 15649582.
169. Wu J, Kuo YP, George AA, Xu L, Hu J, Lukas RJ. beta-Amyloid directly inhibits human alpha4beta2-nicotinic acetylcholine receptors heterologously expressed in human SH-EP1 cells. J Biol Chem. 2004;279(36):37842-51. doi: 10.1074/jbc.M400335200. PubMed PMID: 15234980.
170. Graham AJ, Ray MA, Perry EK, Jaros E, Perry RH, Volsen SG, Bose S, Evans N, Lindstrom J, Court JA. Differential nicotinic acetylcholine receptor subunit expression in the human hippocampus. Journal of Chemical Neuroanatomy. 2003;25(2):97-113. doi: 10.1016/s0891-0618(02)00100-x.
171. Paterson D, Nordberg A. Neuronal nicotinic receptors in the human brain. Progress in Neurobiology. 2000;61(1):75-111. doi: 10.1016/s0301-0082(99)00045-3.
172. Mesulam MM, Geula C, Moran MA. Anatomy of cholinesterase inhibition in Alzheimer's disease: effect of physostigmine and tetrahydroaminoacridine on plaques and tangles. Ann Neurol. 1987;22(6):683-91. doi: 10.1002/ana.410220603. PubMed PMID: 3435078.
173. Gallezot JD, Bottlaender M, Gregoire MC, Roumenov D, Deverre JR, Coulon C, Ottaviani M, Dolle F, Syrota A, Valette H. In vivo imaging of human cerebral nicotinic acetylcholine receptors with 2-18F-fluoro-A-85380 and PET. J Nucl Med. 2005;46(2):240-7. PubMed PMID: 15695782.
174. Kuruvilla SA, Hillmer AT, Wooten DW, Patel A, Christian BT, Mukherjee J. Synthesis and evaluation of 2-18F-fluoro-5-iodo-3-[2-(S)-3, 4-dehydropyrrolinylmethoxy] pyridine (18F-Niofene) as a potential imaging agent for nicotinic α4β2 receptors. American journal of nuclear medicine and molecular imaging. 2014;4(4):354.

175. Wong DF, Kuwabara H, Kim J, Brasic JR, Chamroonrat W, Gao Y, Valentine H, Willis W, Mathur A, McCaul ME, Wand G, Gean EG, Dannals RF, Horti AG. PET imaging of high-affinity alpha4beta2 nicotinic acetylcholine receptors in humans with 18F-AZAN, a radioligand with optimal brain kinetics. J Nucl Med. 2013;54(8):1308-14. doi: 10.2967/jnumed.112.108001. PubMed PMID: 23801676.

176. Kuwabara H, Gao Y, Stabin M, Coughlin J, Nimmagadda S, Dannals RF, Pomper MG, Horti AG. Imaging alpha4beta2 Nicotinic Acetylcholine Receptors (nAChRs) in Baboons with [18F]XTRA, a Radioligand with Improved Specific Binding in Extra-Thalamic Regions. Mol Imaging Biol. 2017;19(2):280-8. doi: 10.1007/s11307-016-0999-9. PubMed PMID: 27562686.

177. Sattler B, Kranz M, Starke A, Wilke S, Donat CK, Deuther-Conrad W, Patt M, Schildan A, Patt J, Smits R, Hoepping A, Schoenknecht P, Steinbach J, Brust P, Sabri O. Internal dose assessment of (-)-18F-flubatine, comparing animal model datasets of mice and piglets with first-in-human results. J Nucl Med. 2014;55(11):1885-92. doi: 10.2967/jnumed.114.137059. PubMed PMID: 25286922.

178. Toyohara J, Sakata M, Wu J, Ishikawa M, Oda K, Ishii K, Iyo M, Hashimoto K, Ishiwata K. Preclinical and the first clinical studies on [11C]CHIBA-1001 for mapping alpha7 nicotinic receptors by positron emission tomography. Ann Nucl Med. 2009;23(3):301-9. doi: 10.1007/s12149-009-0240-x. PubMed PMID: 19337782.

179. Wong DF, Kuwabara H, Pomper M, Holt DP, Brasic JR, George N, Frolov B, Willis W, Gao Y, Valentine H, Nandi A, Gapasin L, Dannals RF, Horti AG. Human brain imaging of alpha7 nAChR with [(18)F]ASEM: a new PET radiotracer for neuropsychiatry and determination of drug occupancy. Mol Imaging Biol. 2014;16(5):730-8. doi: 10.1007/s11307-014-0779-3. PubMed PMID: 25145965; PMCID: PMC5344036.

180. Gao Y, Kellar KJ, Yasuda RP, Tran T, Xiao Y, Dannals RF, Horti AG. Derivatives of dibenzothiophene for positron emission tomography imaging of alpha7-nicotinic acetylcholine receptors. J Med Chem. 2013;56(19):7574-89. doi: 10.1021/jm401184f. PubMed PMID: 24050653; PMCID: PMC3866913.

181. Pichika R, Easwaramoorthy B, Collins D, Christian BT, Shi B, Narayanan TK, Potkin SG, Mukherjee J. Nicotinic alpha4beta2 receptor imaging agents: part II. Synthesis and biological evaluation of 2-[18F]fluoro-3-[2-((S)-3-pyrrolinyl)methoxy]pyridine (18F-nifene) in rodents and imaging by PET in nonhuman primate. Nucl Med Biol. 2006;33(3):295-304. doi: 10.1016/j.nucmedbio.2005.12.017. PubMed PMID: 16631077.

182. Fujita M, Ichise M, van Dyck CH, Zoghbi SS, Tamagnan G, Mukhin AG, Bozkurt A, Seneca N, Tipre D, DeNucci CC, Iida H, Vaupel DB, Horti AG, Koren AO, Kimes AS, London ED, Seibyl JP, Baldwin RM, Innis RB. Quantification of nicotinic acetylcholine receptors in human brain using [123I]5-I-A-85380 SPET. Eur J Nucl Med Mol Imaging. 2003;30(12):1620-9. doi: 10.1007/s00259-003-1320-0. PubMed PMID: 14523584.

183. Kendziorra K, Wolf H, Meyer PM, Barthel H, Hesse S, Becker GA, Luthardt J, Schildan A, Patt M, Sorger D, Seese A, Gertz HJ, Sabri O. Decreased cerebral alpha4beta2* nicotinic acetylcholine receptor availability in patients with mild cognitive impairment and Alzheimer's disease assessed with positron emission tomography. Eur J Nucl Med Mol Imaging. 2011;38(3):515-25. doi: 10.1007/s00259-010-1644-5. PubMed PMID: 21069319.

184. Mukherjee J, Lao PJ, Betthauser TJ, Samra GK, Pan ML, Patel IH, Liang C, Metherate R, Christian BT. Human brain imaging of nicotinic acetylcholine alpha4beta2* receptors using [(18) F]Nifene: Selectivity, functional activity, toxicity, aging effects, gender effects, and extrathalamic pathways. J Comp Neurol. 2018;526(1):80-95. doi: 10.1002/cne.24320. PubMed PMID: 28875553; PMCID: PMC5788574.

185. Hillmer AT, Wooten DW, Slesarev MS, Ahlers EO, Barnhart TE, Murali D, Schneider ML, Mukherjee J, Christian BT. PET imaging of alpha4beta2* nicotinic acetylcholine receptors: quantitative analysis of 18F-nifene kinetics in the nonhuman primate. J Nucl Med. 2012;53(9):1471-80. doi: 10.2967/jnumed.112.103846. PubMed PMID: 22851633; PMCID: PMC3580212.

186. Lao PJ, Betthauser TJ, Tudorascu DL, Barnhart TE, Hillmer AT, Stone CK, Mukherjee J, Christian BT. [18 F]Nifene test-retest reproducibility in first-in-human imaging of alpha4beta2* nicotinic acetylcholine receptors. Synapse. 2017;71(8). doi: 10.1002/syn.21981. PubMed PMID: 28420041; PMCID: PMC5541262.

187. Constantinescu CC, Garcia A, Mirbolooki MR, Pan ML, Mukherjee J. Evaluation of [18F]Nifene biodistribution and dosimetry based on whole-body PET imaging of mice. Nucl Med Biol. 2013;40(2):289-94. doi: 10.1016/j.nucmedbio.2012.11.004. PubMed PMID: 23265670; PMCID: PMC3557576.

188. Thomas SR, Stabin MG, Chen CT, Samaratunga RC. MIRD Pamphlet No. 14 revised: A dynamic urinary bladder model for radiation dose calculations. Journal of Nuclear Medicine. 1999;40(4):102s-23s. PubMed PMID: WOS:000079521800033.
189. Bottlaender M, Valette H, Roumenov D, Dolle F, Coulon C, Ottaviani M, Hinnen F, Ricard M. Biodistribution and radiation dosimetry of 18F-fluoro-A-85380 in healthy volunteers. J Nucl Med. 2003;44(4):596-601. PubMed PMID: 12679405.
190. Kranz M, Sattler B, Tiepolt S, Wilke S, Deuther-Conrad W, Donat CK, Fischer S, Patt M, Schildan A, Patt J, Smits R, Hoepping A, Steinbach J, Sabri O, Brust P. Radiation dosimetry of the alpha4beta2 nicotinic receptor ligand (+)-[18F]flubatine, comparing preclinical PET/MRI and PET/CT to first-in-human PET/CT results. EJNMMI Phys. 2016;3(1):25. doi: 10.1186/s40658-016-0160-5. PubMed PMID: 27770429; PMCID: PMC5074934.
191. Hoffman EJ, Huang SC, Phelps ME. Quantitation in positron emission computed tomography: 1. Effect of object size. J Comput Assist Tomogr. 1979;3(3):299-308. PubMed PMID: 438372.
192. Huang SC, Hoffman EJ, Phelps ME, Kuhl DE. Quantitation in positron emission computed tomography: 2. Effects of inaccurate attenuation correction. J Comput Assist Tomogr. 1979;3(6):804-14. PubMed PMID: 315970.
193. Huang SC, Hoffman EJ, Phelps ME, Kuhl DE. Quantitation in positron emission computed tomography: 3 Effect of sampling. J Comput Assist Tomogr. 1980;4(6):819-26. PubMed PMID: 6971301.
194. Hoffman EJ, Huang SC, Phelps ME, Kuhl DE. Quantitation in positron emission computed tomography: 4. Effect of accidental coincidences. J Comput Assist Tomogr. 1981;5(3):391-400. PubMed PMID: 6972394.
195. Mazziotta JC, Phelps ME, Plummer D, Kuhl DE. Quantitation in positron emission computed tomography: 5. Physical--anatomical effects. J Comput Assist Tomogr. 1981;5(5):734-43. PubMed PMID: 6975289.
196. Hoffman EJ, Huang SC, Plummer D, Phelps ME. Quantitation in positron emission computed tomography: 6. effect of nonuniform resolution. J Comput Assist Tomogr. 1982;6(5):987-99. PubMed PMID: 6982909.
197. Casey ME, Hoffman EJ. Quantitation in positron emission computed tomography: 7. A technique to reduce noise in accidental coincidence measurements and coincidence efficiency calibration. J Comput Assist Tomogr. 1986;10(5):845-50. PubMed PMID: 3489018.
198. Zaidi H, Montandon ML, Slosman DO. Magnetic resonance imaging-guided attenuation and scatter corrections in three-dimensional brain positron emission tomography. Med Phys. 2003;30(5):937-48. doi: 10.1118/1.1569270. PubMed PMID: 12773003.
199. Hofmann M, Steinke F, Scheel V, Charpiat G, Farquhar J, Aschoff P, Brady M, Scholkopf B, Pichler BJ. MRI-based attenuation correction for PET/MRI: a novel approach combining pattern recognition and atlas registration. J Nucl Med. 2008;49(11):1875-83. doi: 10.2967/jnumed.107.049353. PubMed PMID: 18927326.
200. Catana C, van der Kouwe A, Benner T, Michel CJ, Hamm M, Fenchel M, Fischl B, Rosen B, Schmand M, Sorensen AG. Toward implementing an MRI-based PET attenuation-correction method for neurologic studies on the MR-PET brain prototype. J Nucl Med. 2010;51(9):1431-8. doi: 10.2967/jnumed.109.069112. PubMed PMID: 20810759; PMCID: PMC3801218.
201. Keereman V, Fierens Y, Broux T, De Deene Y, Lonneux M, Vandenberghe S. MRI-based attenuation correction for PET/MRI using ultrashort echo time sequences. J Nucl Med. 2010;51(5):812-8. doi: 10.2967/jnumed.109.065425. PubMed PMID: 20439508.
202. Burger C, Goerres G, Schoenes S, Buck A, Lonn AH, Von Schulthess GK. PET attenuation coefficients from CT images: experimental evaluation of the transformation of CT into PET 511-keV attenuation coefficients. Eur J Nucl Med Mol Imaging. 2002;29(7):922-7. doi: 10.1007/s00259-002-0796-3. PubMed PMID: 12111133.
203. Xu M, Cutler PD, Luk WK. Adaptive, segmented attenuation correction for whole-body PET imaging. Ieee Transactions on Nuclear Science. 1996;43(1):331-6. doi: Doi 10.1109/23.485974. PubMed PMID: WOS:A1996TX79200012.
204. Phelps ME, Hoffman EJ, Mullani NA, Ter-Pogossian MM. Application of annihilation coincidence detection to transaxial reconstruction tomography. J Nucl Med. 1975;16(3):210-24. PubMed PMID: 1113170.

205. Adam LE, Zaers J, Ostertag H, Trojan H, Bellemann ME, Brix G. Performance evaluation of the whole-body PET scanner ECAT EXACT HR/sup +/ following the IEC standard. IEEE Transactions on Nuclear Science. 1997;44(3):1172-9. doi: 10.1109/23.596983.
206. Xu M, Luk WK, Cutler PD, Digby WM. Local threshold for segmented attenuation correction of PET imaging of the thorax. IEEE Transactions on Nuclear Science. 1994;41(4):1532-7. doi: 10.1109/23.322944.
207. Sprecher KE, Bendlin BB, Racine AM, Okonkwo OC, Christian BT, Koscik RL, Sager MA, Asthana S, Johnson SC, Benca RM. Amyloid burden is associated with self-reported sleep in nondemented late middle-aged adults. Neurobiol Aging. 2015;36(9):2568-76. doi: 10.1016/j.neurobiolaging.2015.05.004. PubMed PMID: 26059712; PMCID: PMC4523445.
208. Joshi A, Koeppe RA, Fessler JA. Reducing between scanner differences in multi-center PET studies. Neuroimage. 2009;46(1):154-9. doi: 10.1016/j.neuroimage.2009.01.057. PubMed PMID: 19457369; PMCID: PMC4308413.
209. Lopresti BJ, Klunk WE, Mathis CA, Hoge JA, Ziolko SK, Lu X, Meltzer CC, Schimmel K, Tsopelas ND, DeKosky ST. Simplified quantification of Pittsburgh Compound B amyloid imaging PET studies: a comparative analysis. J Nucl Med. 2005;46(12):1959-72; PMCID: 16330558.
210. Ossenkoppele R, Tolboom N, Foster-Dingley JC, Adriaanse SF, Boellaard R, Yaqub M, Windhorst AD, Barkhof F, Lammertsma AA, Scheltens P, van der Flier WM, van Berckel BN. Longitudinal imaging of Alzheimer pathology using [11C]PIB, [18F]FDDNP and [18F]FDG PET. Eur J Nucl Med Mol Imaging. 2012;39(6):990-1000. doi: 10.1007/s00259-012-2102-3. PubMed PMID: 22441582.
211. Vlassenko AG, Mintun MA, Xiong C, Sheline YI, Goate AM, Benzinger TL, Morris JC. Amyloid-beta plaque growth in cognitively normal adults: longitudinal [11C]Pittsburgh compound B data. Ann Neurol. 2011;70(5):857-61. doi: 10.1002/ana.22608. PubMed PMID: 22162065; PMCID: PMC3243969.
212. Hofmann M, Bezrukov I, Mantlik F, Aschoff P, Steinke F, Beyer T, Pichler BJ, Scholkopf B. MRI-based attenuation correction for whole-body PET/MRI: quantitative evaluation of segmentation- and atlas-based methods. J Nucl Med. 2011;52(9):1392-9. doi: 10.2967/jnumed.110.078949. PubMed PMID: 21828115.
213. Liu F, Jang H, Kijowski R, Bradshaw T, McMillan AB. Deep Learning MR Imaging-based Attenuation Correction for PET/MR Imaging. Radiology. 2018;286(2):676-84. doi: 10.1148/radiol.2017170700. PubMed PMID: 28925823; PMCID: PMC5790303.
214. Hoffman EJ, Cutler PD, Digby WM, Mazziotta JC. 3-D phantom to simulate cerebral blood flow and metabolic images for PET. IEEE Transactions on Nuclear Science. 1990;37(2):616-20. doi: 10.1109/23.106686.
215. Bland JM, Altman DG. Statistical Methods for Assessing Agreement between Two Methods of Clinical Measurement. Lancet. 1986;1(8476):307-10. doi: 10.1016/S0140-6736(86)90837-8. PubMed PMID: WOS:A1986AYW4000013.

APPENDIX A: SEMI-AUTOMATED PURIFICATION AND FORMULATION MODULE

Radiosynthesizers available for this work, as well as some commercially available radiosynthesizers do not include or have limited systems for monitoring and controlling HPLC purification, post-HPLC purification SPE, and formulation and filtration of PET radiopharmaceuticals. While radioactivity levels are lower for these steps compared to the radiosynthesis, these radiation levels and exposer times are not insignificant. In an effort to reduce radiation exposure and further automate the radioproduction of the PET radioligands, a device (RadioChromaForm) was designed, manufactured, and use-tested.

The configuration of the fluidics path (Figure A.1) used positive pressure additions of pre-filled reservoirs via a serial configuration of solenoid flipper valves (6604, Bürkert Fluid Control Systems) with polyether ether ketone (PEEK) ¼-28 UNF manifolds, and prefabricated and custom designed glassware

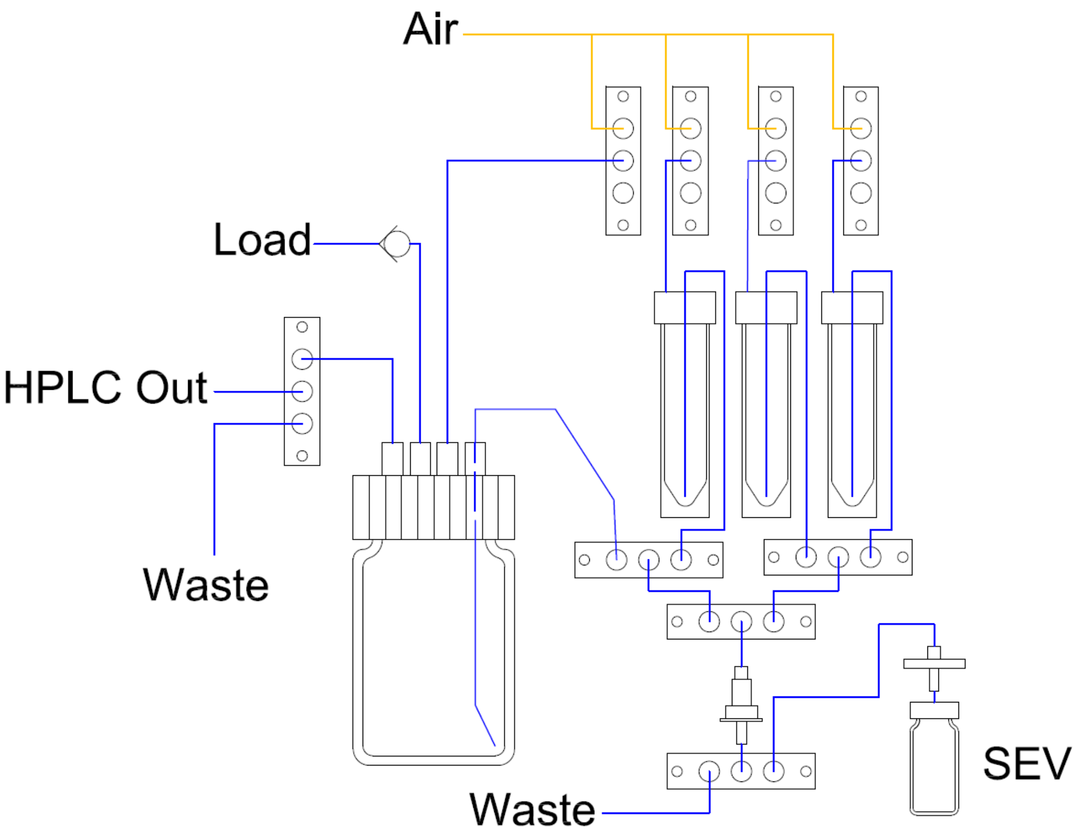

Figure A.1 RadioChromForm Air and Fluidics Flow Diagram

(Figure A.2). To reduce potential for residual contamination from mobile phase solvents, the SPE cartridge inlet path was divided into two segments: a trap and rinse segment, and an elute and formulate segment. Valve control was achieved using transistor-transistor logic (TTL) signals generated by a USB interface (USB-6008, National Instruments) in combination with a custom designed circuit (Figure A.3) that employed Darlington transistor arrays (ULN2003AN, Texas Instruments). The USB-6008 analog inputs were used to monitor voltage outputs from the HPLC UV detector (2489, Waters) and the HPLC radiation detector. The digital counter input on the USB-6008 was also included as a separate option for monitoring the HPLC radiation detector. Initiation of HPLC data acquisition was accomplished using a digital input on the USB-6008. The chassis was designed from a prefabricated instrument enclosure (SC-13100, Bud Industries) that was modified to allow attachment of hardware and a custom-designed reservoir rack (Figure A.4). A complete list of system components is included in Table A.1.

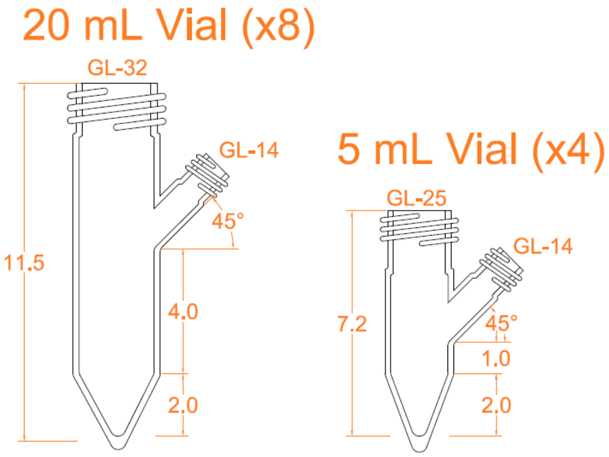

Figure A.2 Reagent Vial Schematics

LabView software (V2017, National Instruments) was written to control hardware components and perform the acquisition and analysis of HPLC chromatogram data. HPLC fraction collection was accomplished by a remote user interface built into the Labview front panel. The SPE and formulation sequences were automated through pre-programmed, timed steps with the exception of the SPE trapping step that requires user input to advance to the rinse step. This was implemented to avoid partial delivery of diluted product during trapping steps due to differences in HPLC collection volumes. All settings can be saved and recalled once the timing steps are established during testing runs, and can be dynamically updated during operation if required.

The unit was validated by use-testing during validation radiochemistry for [^{18}F]THK-5351 and [^{18}F]MK-6240. Presently, this system has been used for over 60 syntheses of [^{18}F]MK-6240.

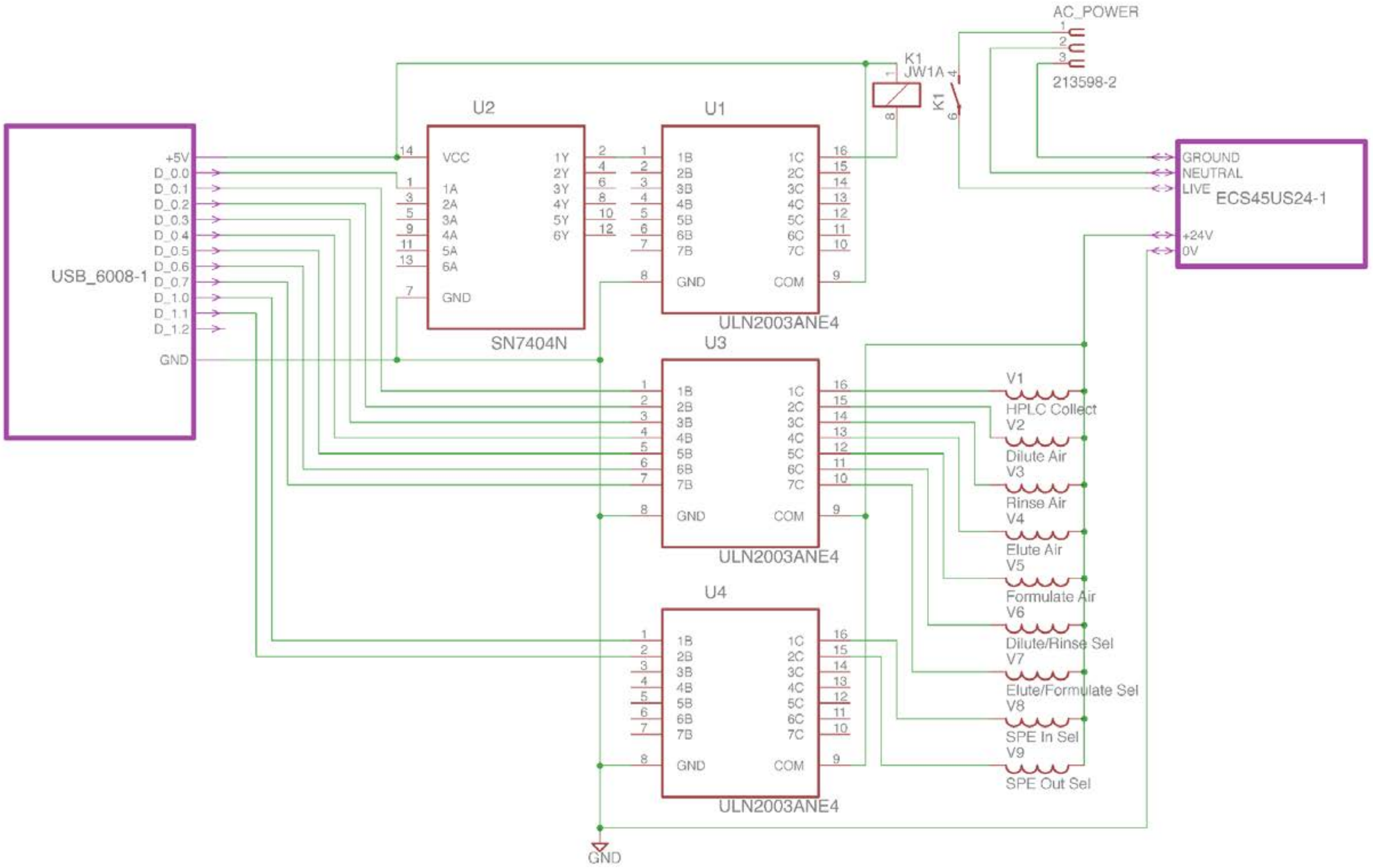

Figure A.3 RadioChromaForm Electronic Schematic for Valve and Power Control

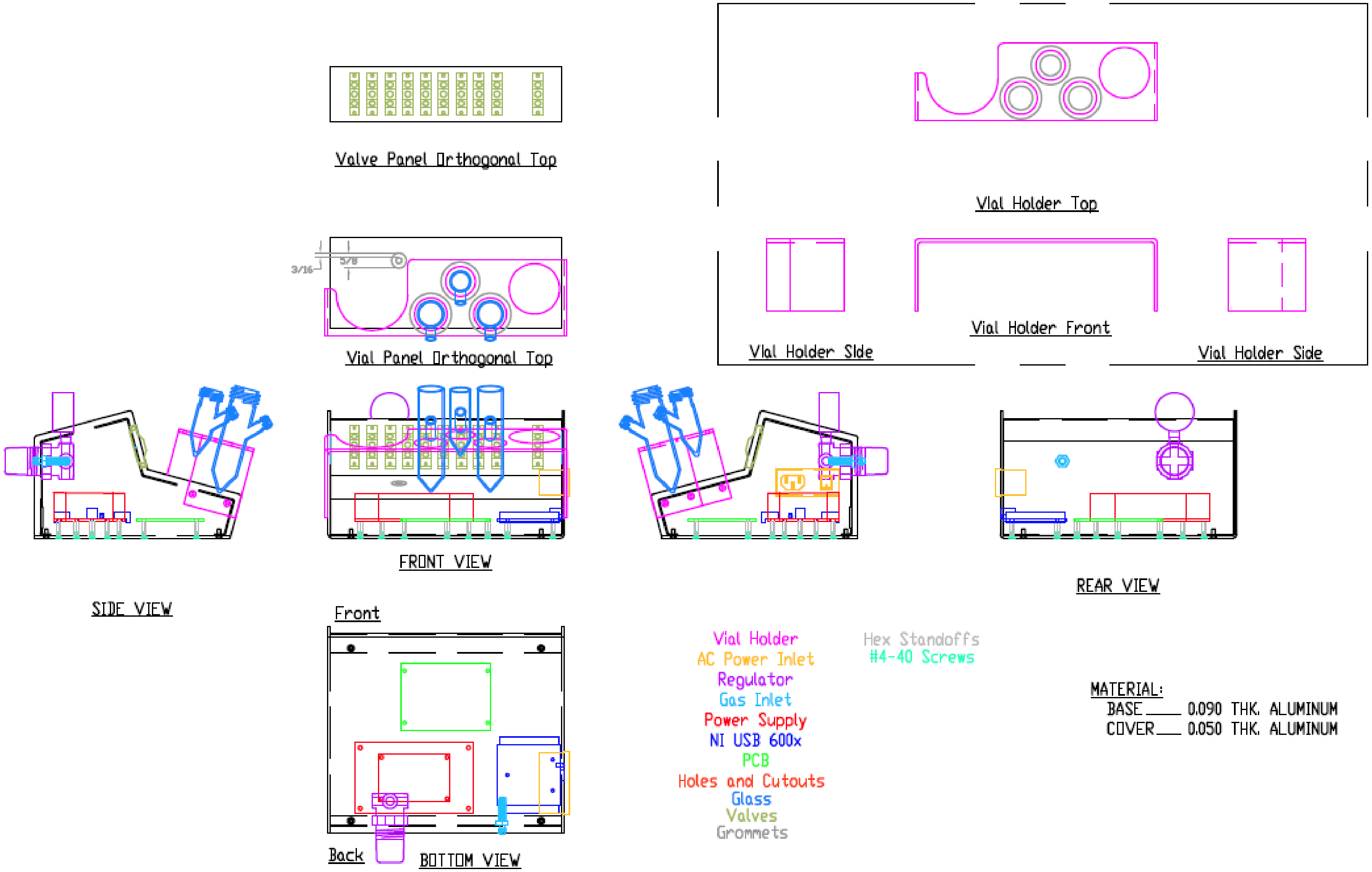

Figure A.4 RadioChromaForm Chasis Design

System	Manufacturer/Supplier	Model	Description
Electronics	National Instruments	USB-6008	TTL Controller for LabView
	RadioShack	276-168	Printed Prototype Board
	XP Power	ECS45US24	Power Supply 24V 45W
	Molex	09-50-1031	AC Power Plug
	Molex	09-50-1041	DC Power Plug
	Molex	08-70-1031	Molex Pins
	Panasonic	JS1-5V-F	Main Power Relay
	Texas Instruments	SN7404N	Hex Inverter
	Qualtek	761-18/003	Fused and Switched IEC Plug
	Texas Instruments	ULN2003AN	Darlington Transistor IC TTL
	TE Connectivity	87X6758	Dip socket 14 pin
	TE Connectivity	87X6759	Dip socket 16 pin
	Twin Industries	8300SB1	Prototyping board
	Phantom YoYo	NA	10 pack jumpers for Burkert valves
Valves	Burkert	6604	3/2-way Solenoid Valve
	Burkert	SET4	PEEK 1/4-28 Manifold
Air Handling	Speedaire	4ZM07	Regulator
	Grainger	4FLP9	Pressure Gauge
	Grainger	1LRH9	(x10)1/8" Push in Tee
	Swagelok	SS-200-1-2	1/8" Swagelok to male NPT
	Swagelok	SS-200-61	1/8" Swagelok Bulkhead
Glass, Caps and Bottles	Corning	1395-100	100 mL GL45 storage bottle (10 pk)
	Vaplock	S45X-4D	Ported GL-45 cap (4 port, 1/4-28)
	Chemglass	CG-194-04	GL-32 Glass
	Chemglass	CG-194-03	GL-25 Glass
	Chemglass	CG-194-01	GL-14 Glass
	Vaplock	S32X-2D	Ported GL-32 cap (2 ports, 1/4-28)
	Vaplock	S25X-2D	Ported GL-25 cap (2 ports, 1/4-28)
	Chemglass	CG-195-01	Holed GL-14 cap
	MDS	14823203	GL-14 Septa (1000 pk)
	Vaplock	S45X-4D	Ported GL-45 cap (2 port, 1/4-28)
Fittings and Tubing	IDEX	P-201	1/4-28, 1/16" nut
	IDEX	P-200X	ferrule, 1/16" (x10)
	IDEX	P-628	Female Luer to 1/4-28 Female
	IDEX	P-675	Male Luer to 1/4-28 Female
	Cole Parmer	NC0340531	Luer check valve (x10)
	Cole-Parmer	EW-06407-41	USP 1/16", 1/32"ID PTFE tubing 25'
	Cole-Parmer	EW-01355-12	1/2-28 Check Valve PEEK/EPDM
Chassis and Hardware	Grainger	CRL031044GR	4-40 x 5/8 in, Al Hex Standoff (x10)
	Grainger	U51122.011.0037	4-40 x 3/8 in, SS Pan Head Screws
	Grainger	U51122.011.0018	4-40 x 3/16 in, SS Pan Head Screws
	Grainger	U51300.011.0025	4-40 x 1/4 in, SS Flat Head Screws
	Speedaire	4ZK13	Regulator nut
	Grainger	6EEE7	Adhesive Cable Tie Mounting (x100)
	Grainger	3MRH2	1/4" Grommet (x50)
	Grainger	3MRN9	7/8" Grommet (x25)
	Grainger	3MRP3	1" Grommet (x10)
	Grainger	3DRZ7	12x24x1/8" Al Plate (H14)
	Grainger	38EH34	1/4" x 10' Neoprene Edging

Table A.1 RadioChromaForm Materials List

APPENDIX B: ALTERNATE [^{18}F]MK-6240 PURIFICATION METHODS

During methods development, several approaches were attempted to radiosynthesize and purify [^{18}F]MK-6240, but no formal side-by-side comparison was made between the HPLC purification methods once pre-HPLC processes were finalized. The comparisons included in this appendix have several methodological differences in the radiochemical synthesis and pre-HPLC SPE that could alter the semi-preparative HPLC purification including differences in precursor mass, hydrolysis conditions and reagent volumes used during the radiosynthesis, pre-HPLC SPE, and the volume and composition of the crude product injected onto semi-preparative HPLC. Because of these differences, this data was excluded from the main text. However, results from these experiments produced interesting findings regarding the radiochemical stability of [^{18}F]MK-6240 in various mobile phases and alternate separations that may reduce the retention time of [^{18}F]MK-6240 from published methods(102, 103), which would further improve EOS radiochemical yields.

Methods

[^{18}F]MK-6240 was synthesized using the ELIXYS with the same sequence of steps described in chapter 2 section 2.3.2, but with different reagent concentrations, volumes and masses. Pre-HPLC SPE ethanol elution volumes, and dilution volumes and reagents used for HPLC injection also differed between

Process	*Run 1*	*Run 2*		*Run 3*
Precursor (manual addition)	0.5 mg in 250 µL DMSO	1.0 mg in 500 µL DMSO		1.0 mg in 500 µL DMSO
Hydrolysis	300 µL 3N HCl (manual add)	750 µL 3N HCl (automated add)		750 µL 3N HCl (manual add)
Neutralization	2.85 mL 0.5M NaOH	2.85 mL 1M NaOH		2.85 mL 1M NaOH
SPE EtOH and Dilution	700 µL EtOH 700 µL DI H_2O (manual)	1 mL EtOH 1mL 10mM NaH_2PO_4 (manual)		1 mL EtOH 1 mL 10 mM NaOAc (automated)
HPLC Column	Luna C18	Luna C18		Gemini C6-phenyl
Mobile Phase	25/75 (v/v) MeCN/10mM NaH_2PO_4	35/65 (v/v) MeCN/10mM Na_2HPO_4	40/60 (v/v) MeCN/10mM Na_2HPO_4	45/55 (v/v) EtOH/10mM NaOAc
Mobile Phase pH	5.5	8	8	7.5
Flow Rate *Column Pressure*	5 mL / min 900 psi	5-10 mL / min 2060 psi	5 mL / min 1090 psi	3 mL / min 3000 psi
Formulated Middle Fraction	Yes	Yes	No	No

Table B.1 [^{18}F]MK-6240 Testing and Purification Conditions tests. In addition to the C6-phenyl column, the Luna C18 column with a guard column was investigated for purification of [^{18}F]MK-6240 using the same UV detector and HPLC pump described in chapter 2. Methodological differences are summarized in Table B.1. Early, middle, and late fraction of the [^{18}F]MK-6240 product peak were collected separately in 50 mL Falcon tubes and characterized on analytical HPLC (see chapter 2 section 3 for analytical system conditions). For two of the preparative HPLC conditions, the middle fraction underwent SPE and was formulated in 10% (v/v) USP ethanol in bacteriostatic saline.

Results

Radiochromatograms for the four semi-preparative HPLC methods are shown in Figure B.1. Retention times were faster for acetonitrile based separations compared to the separation using ethanol, but HPLC recovery (summed fractions 1 and 2) was higher for the ethanol-based method (79%) compared to the acetonitrile based separations (62%, 65%, 66%, for 25% MeCN, 35% MeCN, and 40% MeCN, respectively). Chemical impurities present in the middle fraction of all purification methods were within the limit established in chapter 2. All fractions that were formulated in %10 (v/v) ethanol in bacteriostatic saline remained stable when tested out to four hours post-formulation.

The low HPLC recovery observed when testing the acetonitrile based separations during the second test

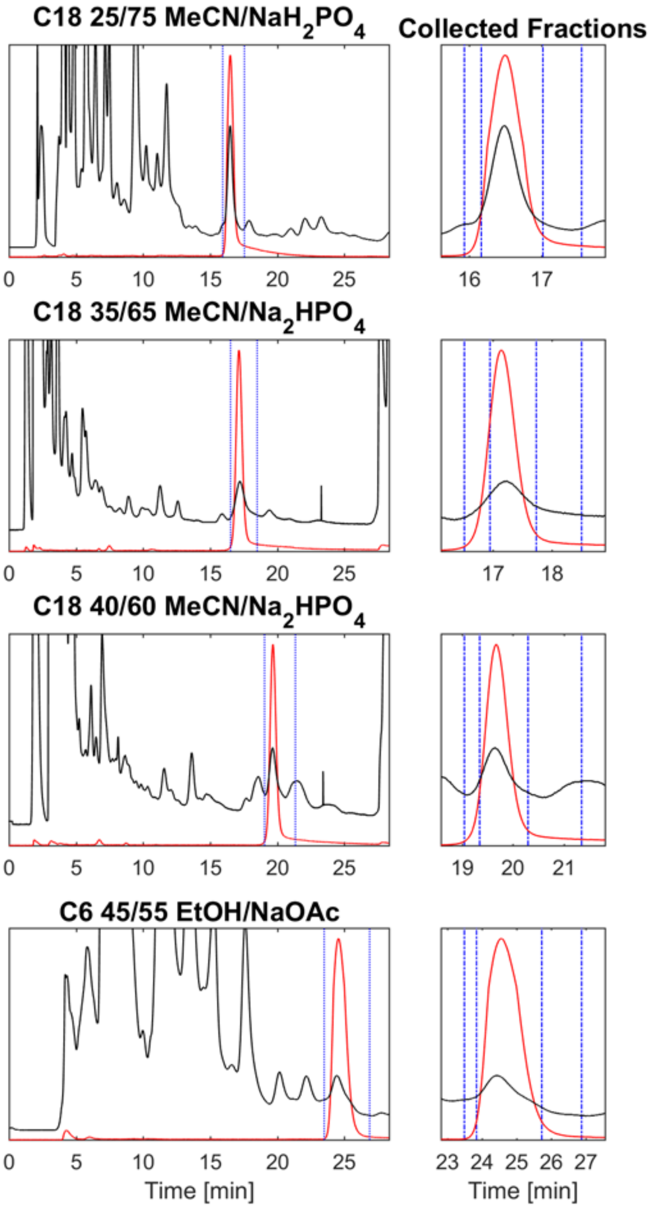

Figure B.1 [^{18}F]MK-6240 Semi-Preparative HPLC Chromatograms and Collected Fractions

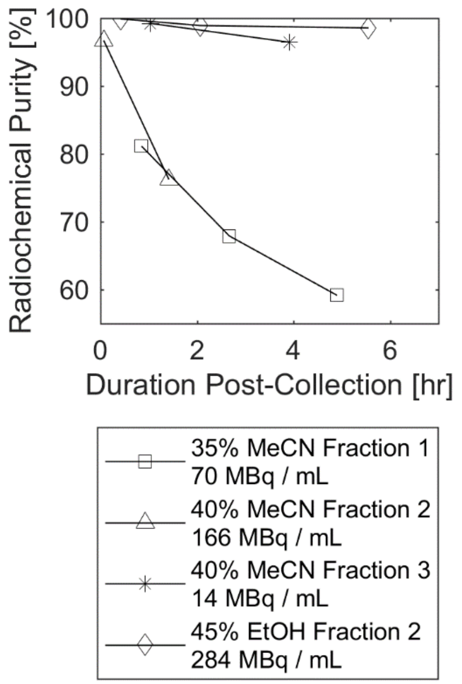

Figure B.2 Radiochemical Stability of [^{18}F]MK-6240 in Mobile Phase. Radioactivity strength is given at the time of collection.

chemistry prompted further investigation. Fractions that hadn't already been formulated in EtOH and saline were retested on analytical HPLC up to six hours after fraction collection. This included fraction one from the 35% acetonitrile separation, fractions two and three from the 40% acetonitrile separation, and fraction two from the ethanol separation. These results indicated radiochemical breakdown in the acetonitrile based mobile phases for activity concentrations of 70 MBq/mL or higher, whereas the middle product fraction for the ethanol based separation was stable at six hours post-collection with a higher activity concentration (284 MBq/mL). In addition, examination of the radioactivity traces for all four semi-preparative separations showed a higher background before the [^{18}F]MK-6240 product peak when compared to after [^{18}F]MK-6240 eluted from the column for the acetonitrile based separations when compared to the ethanol based separation. These results combined with the stability of [^{18}F]MK-6240 in injectable formulation at higher activity strengths up to 334 MBq/mL observed in chapter 2, suggest that ethanol plays a key protective role in preventing radiolytic decomposition of [^{18}F]MK-6240.

APPENDIX C: DETERMINATION OF LGA AND MRTM t*

Accurate estimation of the DVR for LGA and MRTM2 methods is dependent upon selecting the appropriate linearization time (t*) and reference region efflux (k_2') parameters. Both MRTM and SRTM methods allow for direct estimation of the k_2' parameter, which can be used for LGA in the absence of a k_2' derived from arterial analysis. Evaluation of t* typically involves assessment of linearity/parameter stability derived from stepwise t* values. For LGA, this could include comparison of regression residuals, visual assessment of the linear regression of the integral transformed data, or plotting the slope and/or intercept estimates as a function of t*. However, this assessment is more difficult to visualize for MRTM due to the implementation of a multilinear regression. Concurrently, binding estimates for reversibly bound ligands take longer to stabilize in receptor rich regions, which could result in a receptor density dependent negative

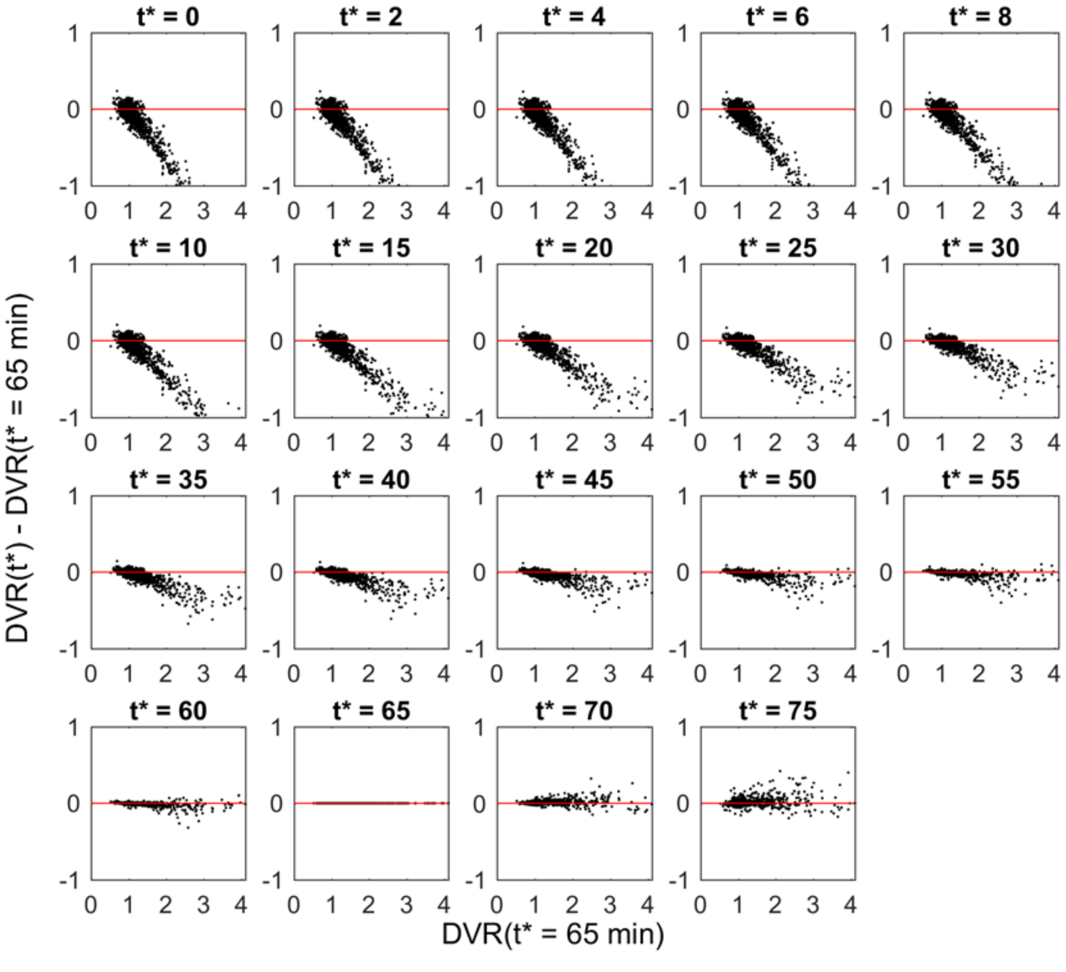

Figure C.1 Bland-Altman Plots for t Determination: LGA [^{18}F]MK-6240 (no k_2' term) using t* = 65 minutes for the standard of comparison.*

bias for DVR determined before estimates are stable in these regions. Thus, an ideal comparison of stepwise t* values would capture not only the stability of regression parameters (i.e. DVR), but would also show any potential bias due to the level of radioligand specific binding. This was accomplished in the present work by plotting the differences between DVR estimates derived from stepwise t* values in two ways. Bland-Altman(215) plots were used to identify potential bias related to the level of binding. Then, to identify global DVR bias the average difference between DVR estimates was plotted as a function of t*. These sets of plots are then generated using late time points for

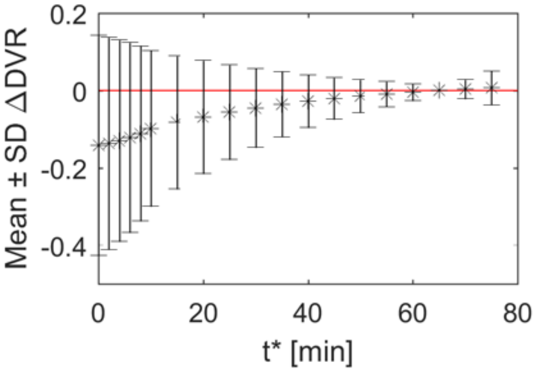

Figure C.2 Global DVR Differences for [^{18}F]MK-6240 LGA DVR Using Stepwise t with t* = 65 minutes for the standard of comparison (no k_2' term)*

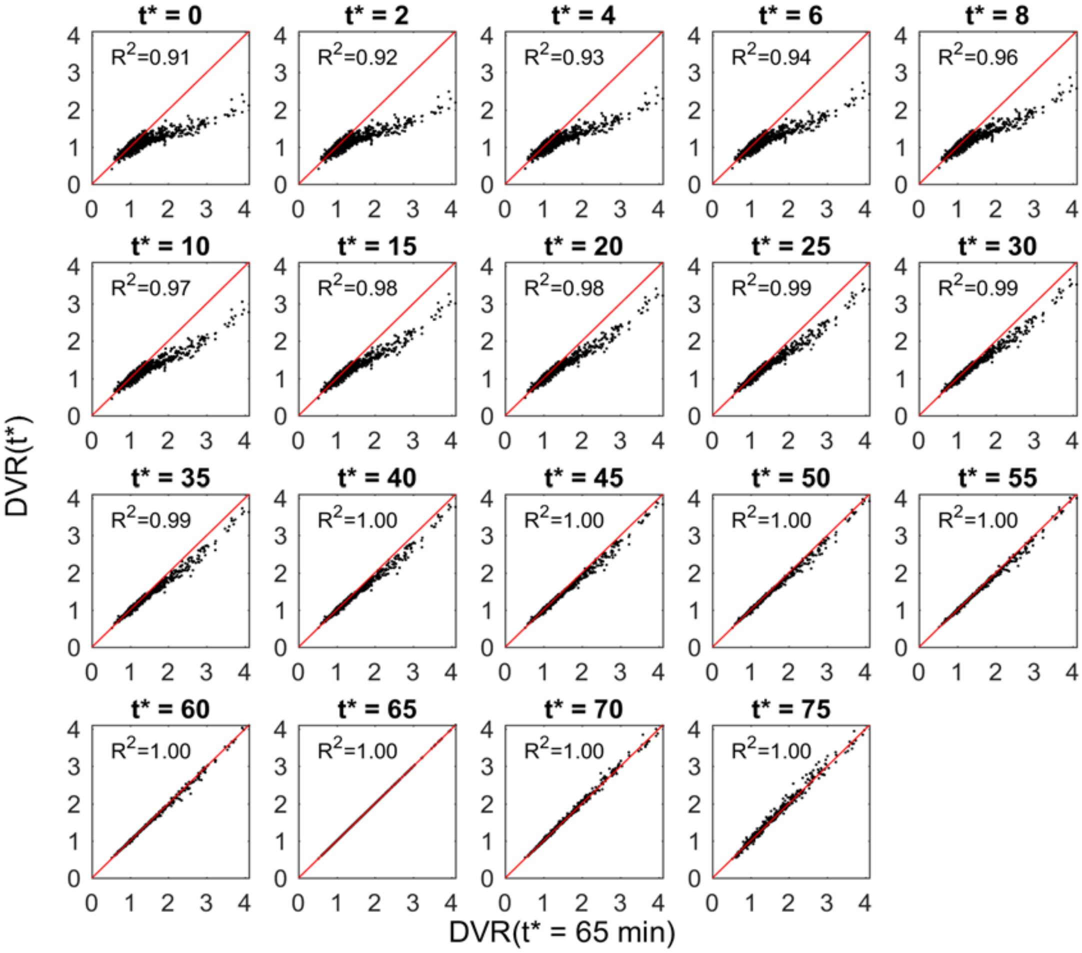

Figure C.3 Stepwise [^{18}F]MK-6240 LGA t DVR Comparison by Regression using t* = 65 minutes as the standard for comparison*

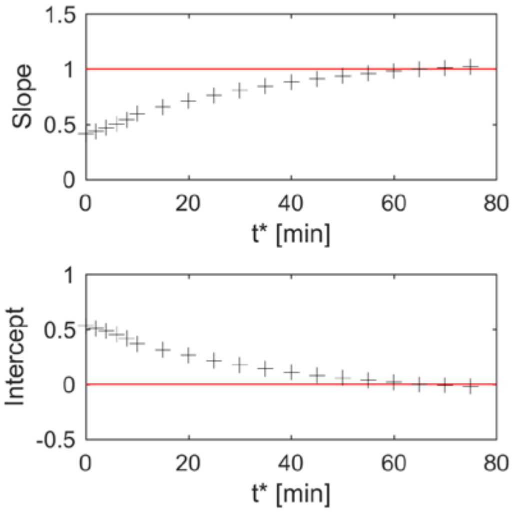

Figure C.4 Slope and Intercept Parameters for Regressions from Figure C.3 as a function of t. The standard of comparison is t* = 65 minutes*

t* values as the standard of comparison, and then shifting this value progressively earlier and generating a new set of plots. The value of t* is then selected whereby binding dependence and global differences are minimal for t* > t.

An example of the final set of plots used to define t* for the LGA method with [^{18}F]MK-6240 is shown in Figure C.1 and Figure C.2. For comparison, the same data from Figure C.1 is plotted in Figure C.3 as scatter plots with Pearson moment correlation coefficients given for linear regression. Additionally, the regression parameters from Figure C.2 are plotted as a function of t* in Figure C.4.

When compared to scatter plots, the Bland-Altman approach more easily identifies binding dependent differences, particularly for t* values near the value used as the standard of comparison (i.e. 55 or 60 minutes in this dataset). Previous works in PET neuroimaging literature for [^{11}C]PiB have made comparisons between radiotracers using regression correlation coefficients(64). However, this dataset demonstrates that while global and binding dependent differences exists for various t* values comparisons, but the correlation coefficient does not provide a meaningful metric to identify these differences.

Another advantage to using Bland-Altman plots for binding comparisons is that this technique also provides a visual representation of the variaiblity across different levels of binding. Another approach that reaches a similar conclusion to the Bland-Altman/global difference approach is plotting the slopes of the regression line for the stepwise t* comparisons as a function of t* (Figure C.4). In this comparison, the value t* can be selected such that the change in slope and intercept parameters is minimized and comparisons with t>t* yield slope and intercept terms near unity.

APPENDIX D: REGION OF INTEREST COMPARISON

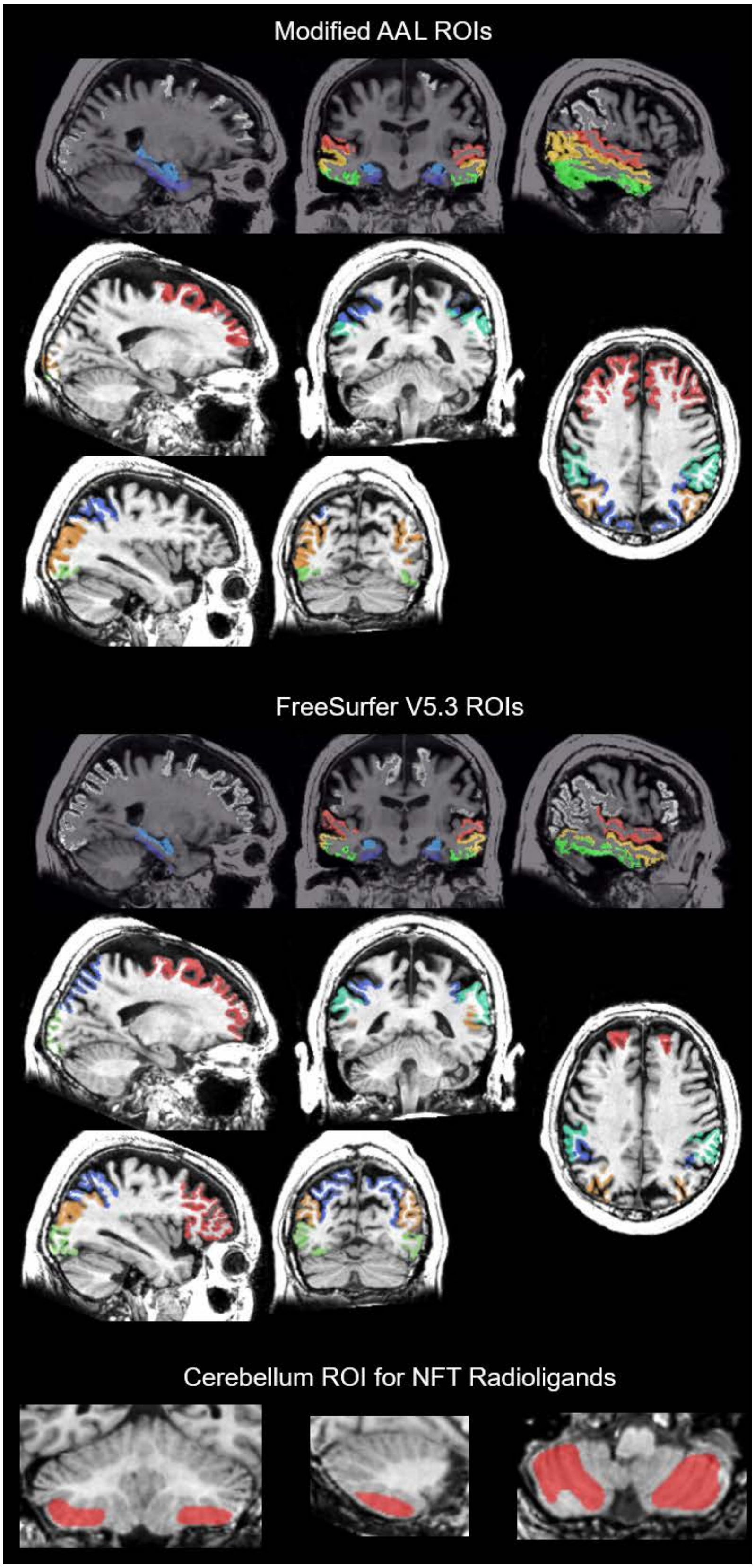

Figure D.1 Comparison of MRI Space ROIs

Data in Chapter 3 were calculated at the ROI level using different atlases for the different sections. The THK tracer analysis and comparison used FreeSurfer V5.3, whereas the MK-6240 section and the comparisons of all three radiotracers used the AAL atlas for ROI delineation. In addition, FreeSurfer ROIs were combined to form a composite frontal cortex ROI. A comparison of the ROIs is presented here in a representative subject. The AAL atlas was inverse warped to MRI space and restricted to voxels with $P_{GM}>0.3$. Importantly for the comparison between all three tracers, the same atlas (Modified AAL) and reference region was used for all three tracers. Figure D.1 shows representative ROIs for some of the regions used in the analyses. The gray MRI background panels show the entorhinal cortex (purple), hippocampus (blue), inferior (green), middle (orange), and superior (red) temporal cortex ROIs. Panels with the white MRI background show the frontal cortex (red), supramarginal (teal) and inferior (lavender) parietal cortex, and the inferior (green) and middle (orange) occipital cortex ROIs.

APPENDIX E: [^{18}F]MK-6240 INTERFRAME REALIGNMENT

The lack of non-specific binding of [^{18}F]MK-6240 presented a challenge during post-reconstruction processing of dynamic PET data. Early attempts to perform interframe realignment of the dynamic PET time series in subjects that had minimal specific tracer binding often failed when using SPM12's realign function. This function attempts to reorient individual frames by applying an affine transformation with six degrees of freedom (translation and rotation) and evaluates differences between individual frames and a mean image of the PET time series using a least sum of squares objective function. Therefore, the SPM12 realign function is expecting spatial similarity between frames, which was not the case for [^{18}F]MK-6240 where the signal was high and dominated by brain uptake during bolus passage, but not during later frames when the brain signal was similar to background signal throughout the head. Furthermore, later time points had high focal signal in regions outside the brain that were not present at early time points. Therefore, a method was developed to minimize the spatial differences between early and late PET frames to improve the interframe realignment. This was accomplished using a two-step approach that removed voxels outside the head on a frame-by-frame basis, and then transformed the PET data prior to interframe realignment.

Defining Image Background

Prior to background determination, dynamic PET data were summed for the entire PET time series and smoothed by an isotropic 6mm Gaussian kernel. The top pane of Figure E.1 shows the resulting histogram of the activity concentration of the summed PET data across the entire 3D volume for a typical 90-minute [^{18}F]MK-6240 scan in an individual that did not show signs of elevated uptake in regions associated with NFTs. Notably, the majority of the voxels in the PET image represent signal outside of the head (i.e. background).

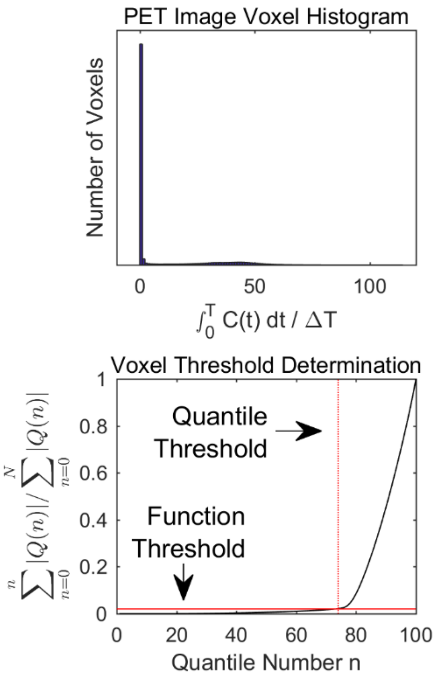

Figure E.1 PET Background Threshold Determination

One-hundred quantiles (Q) were determined for the summed PET voxels. Quantiles were normalized such that the sum of the absolute value of the quantiles were equal to one. A threshold was then empirically selected where the cumulative normalized quantiles would discriminate between the background voxels and voxels within the head. This threshold is visualized in the bottom pane of Figure E.1 where the solid red line is the cumulative normalized quantile threshold, and the dotted line represents the corresponding quantile number. The purpose of normalizing quantiles is that a single threshold can be used across multiple subjects that is not contingent on the activity concentration, which varies between individuals. The absolute value is taken since PET activity concentrations less than zero are a product of the reconstruction process and do not reflect the true activity concentration, which cannot physically be negative.

Frame-by-Frame Background Masking

Individual PET frames were then masked to remove voxels outside of the head. This was accomplished by extracting 100 quantiles for each individual PET frame, and setting PET voxels below the quantile number determined from the summed PET image to either zero of not-a-number (NaN). For example, using the data in shown in Figure E.1, the normalized cumulative quantile threshold of 0.2 corresponds to the 74th quantile, and therefore voxels below the 74th quantile of each individual PET frame would be masked out. Masking each PET frame individually, rather than applying a single global mask to all frames, lessens the potential for registration bias due to the masking process itself and should allow for a more accurate depiction of the motion between frames, but this was not formally evaluated.

Realignment Using Transformed PET Data

Once the background is masked out of each individual frame, the data were transformed by applying the natural log to each individual PET frame (shown in Figure E.2). This minimized the spatial differences occurring throughout the PET time series, thereby limiting their impact on objective function residuals during realignment. Importantly, the masking step resulted in masking out voxels less than one, so the natural log transform did not result in large negative values. The natural log of the masked values was

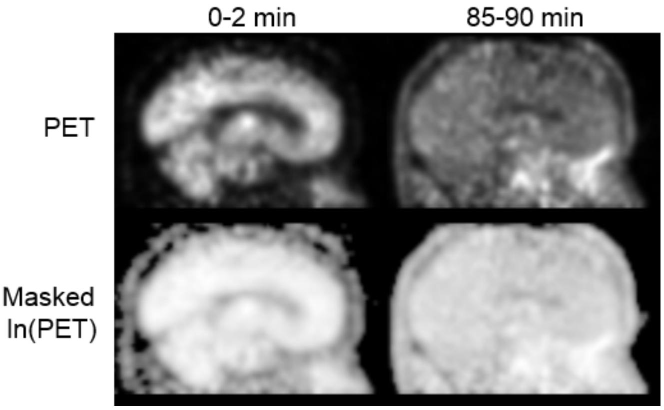

Figure E.2 Comparison of [^{18}F]MK-6240 with Transformed PET Data for Realignment either set to negative infinity or NaN, both of which are ignored by SPM's realignment algorithm. The masked and transformed PET data are then realigned in a two passes by first realigning individual PET frames to the mean of all transformed PET frames, and then generating a new mean image from the first pass realignment and realigning the individual frames to the new mean image. This combined process defines the six parameter affine spatial transformation matrix for each frame that is then applied to the original, unmodified PET time series.

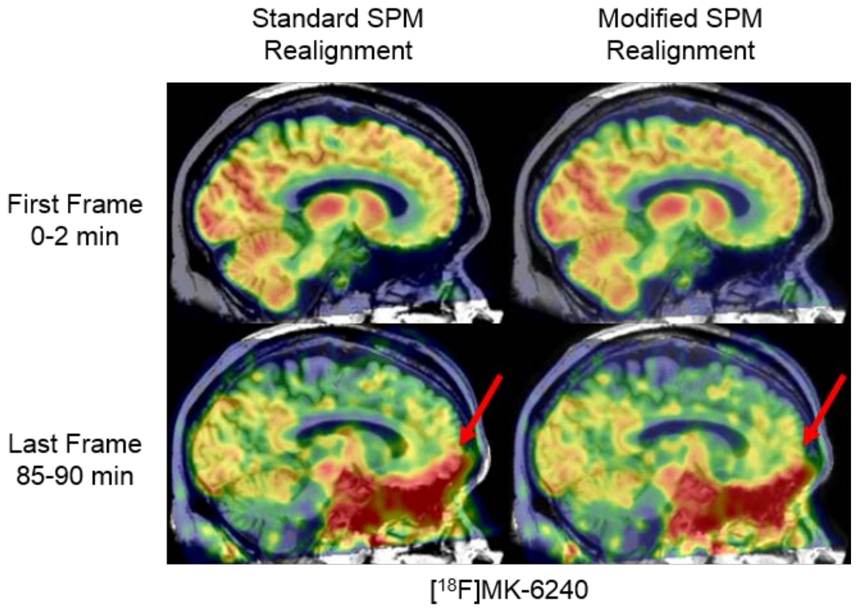

Figure E.3 Comparison of [^{18}F]MK-6240 Realignment Methods

An example comparing the unmodified SPM realignment with the modified realignment method is shown in Figure E.3. The column on the left was processed using a two-pass SPM realignment with unmodified PET data and the column on the right was realigned using the modified realignment method described in this appendix. Both methods are spatially aligned with the brain for the first PET frame (top row), but the standard SPM realignment method caused misalignment of later frames resulting in the signal in the ethmoid sinus being rotated into the orbitofrontal cortex (red arrow). The modified realignment method gave visually improved spatial agreement between the early and late PET data, which can be observed at the intersection of the orbitofrontal cortex and the ethmoid sinus, and in the profile of the nose.